Thermo-compositional structure of the South American Platform lithosphere: Evidence of stability, modification and erosion

Altoe Isabella Lorrainy[1], Goes Saskia[1], and Assumpcao Marcelo S[2]

[1]Imperial College London
[2]University of Sao Paulo

November 16, 2022

Abstract

Constraints on the structure of cratonic lithosphere are essential to improve our understanding of craton formation, evolution and long-term stability. Here, we perform a joint inversion for the thermal and compositional structure of the mantle lithosphere below the South America Platform, using Rayleigh wave group velocities, elevation, and geoid height. Thick thermal lithosphere (200-300 km) is found below the southern Amazonian and São Francisco Cratons and adjoining Parecis Basin and northern Paraná Basin. The southern Rio de la Plata Craton also retains a 200-250 km thick keel. Compositionally, Amazonian, São Francisco and Rio de la Plata lithosphere has a metasomatic and possibly eclogite signature similar to that of North American Proterozoic collision belts. Parecis and northern Paraná lithosphere has likely been altered by Mesozoic plume activity throughout most of its depth, while the rest of the Paraná Basin and the Chaco and Patanal basins appear to have lost the lithospheric root below ~100 km depth that was there during intracratonic basin formation. The low elevation and high geoid of the western Paraná Basin requires a dense (eclogite) layer within the crust/shallow lithosphere, possibly associated with the NeoProterozoic western Paraná Suture Zone and/or Mesozoic plume activity, while topography and geoid of the basins further west and of the western Rio de la Plata craton seem affected by dynamic (subduction-related) topography. Thus, the variable geophysical structure of the platform lithosphere reflects a history that involves besides some stable keels, significant modification and thinning.

Thermo-compositional structure of the South American Platform lithosphere: Evidence of stability, modification and erosion

Isabella Altoe[1], Saskia Goes[1],Marcelo Assumpção[2]

[1]Department of Earth Science and Engineering, Imperial College London, UK
[2]Department of Geophysics, IAG, University of São Paulo, São Paulo, Brazil

Key Points:

- We find thick roots under the Archean/Proterozoic cores and neighboring regions, where roots are altered by plume activity/rifting.
- Significant metasomatism is found at shallow depths in all roots, while eclogite layers in some indicate varying styles of collision.
- Lithospheric root was lost/eroded under the southwest of the platform, likely due to plume/subduction interaction during the Phanerozoic.

Corresponding author: Isabella Altoe, `i.altoe17@imperial.ac.uk`

Abstract

Constraints on the structure of cratonic lithosphere are essential to improve our understanding of craton formation, evolution and long-term stability. Here, we perform a joint inversion for the thermal and compositional structure of the mantle lithosphere below the South America Platform, using Rayleigh wave group velocities, elevation, and geoid height. Thick thermal lithosphere (200-300 km) is found below the southern Amazonian and São Francisco Cratons and adjoining Parecis Basin and northern Paraná Basin. The southern Rio de la Plata Craton also retains a 200-250 km thick keel. Compositionally, Amazonian, São Francisco and Rio de la Plata lithosphere has a metasomatic and possibly eclogite signature similar to that of North American Proterozoic collision belts. Parecis and northern Paraná lithosphere has likely been altered by Mesozoic plume activity throughout most of its depth, while the rest of the Paraná Basin and the Chaco and Patanal basins appear to have lost the lithospheric root below ∼100 km depth that was there during intracratonic basin formation. The low elevation and high geoid of the western Paraná Basin requires a dense (eclogite) layer within the crust/shallow lithosphere, possibly associated with the NeoProterozoic western Paraná Suture Zone and/or Mesozoic plume activity, while topography and geoid of the basins further west and of the western Rio de la Plata craton seem affected by dynamic (subduction-related) topography. Thus, the variable geophysical structure of the platform lithosphere reflects a history that involves besides some stable keels, significant modification and thinning.

Plain Language Summary

Cratons are the ancient cores of continents, preserved at least in part because of their underlying thick cold plate roots, which are assumed to be dry and stiff. Yet, it remains poorly understood how these roots formed, stabilised, and occasionally are lost. Here we investigate the thermal and compositional structure of the plate roots below the old eastern half of South America, using imaged seismic velocities, elevation, and geoid height in the region. Our results show that part of South America has about 250-km thick roots: under the oldest cores of the continent in the northeast and southeast and in the north, and under areas adjacent to these cores, which appear to have survived or regrown after modification by hot upwelling mantle plumes. We find that the western part of the old South American platform has lost a significant part of the root that used to exist, which we attribute to erosion by hot plumes and Andean subduction over the past ∼70 million years. All regions require a more widespread presence of hydrated minerals than usually expected below cratons. Thus, the structure of South America's craton roots sheds light on how they formed, were modified and partially lost.

1 Introduction

1.1 Motivation

Cratons are the stable continental cores formed during the Precambrian. Their formation, evolution and long-term stability is still debated (e.g., van Hunen & Moyen, 2012; C.-T. A. Lee et al., 2011; Sleep, 2005). Mapping lithospheric temperatures and compositional heterogeneity may shed light on their formation, evolution and long-term stability. Cratonic mantle lithosphere is often described as relatively homogeneous, characterized by thick and high-velocity roots (Schaeffer & Lebedev, 2015), low surface heat flow (Cooper et al., 2004), and being approximately neutrally buoyant due to iron depletion as a result of melt extraction (Jordan, 1978; Griffin et al., 2009). However, recent studies have found heterogeneities within and between cratonic keels. Studies using S-to-P receiver functions have detected negative and/or positive velocity gradients in the lithospheric mantle in some cratonic regions (e.g., Miller & Eaton, 2010; Abt et al., 2010; Krueger et al., 2021). Additionally, seismic tomographic studies have found more variation in seismic velocities than can be explained by varying the amount of depletion (e.g., Bruneton et al., 2004; Hieronymus & Goes, 2010; Eeken et al., 2018; Legendre et al., 2012; Liddell et al., 2018).

In a previous study, we modelled Rayleigh-wave dispersion curves for the northeastern North American Craton and resolved five types of compositional structures. Most regions required significant metasomatic alteration over some depths and the structures appeared to reflect different stages of formation and modification of the lithosphere below the region (Altoe et al., 2020; Eeken et al., 2020). Using an update of this approach, here we present results for the South American Platform, comprising the Central Brazilian and Atlantic shields. We perform a joint inversion for thermal and compositional structures of the mantle lithosphere using Rayleigh-wave group-velocity dispersion curves, surface topography, and geoid height. The results reveal variations in thermal lithosphere thickness and compositional structure that also appear to reflect the tectonic history of the region.

1.2 Tectonic History

The South American Platform is defined as the stable interior of South America plate, which has not been deformed by the Andean orogeny during the Phanerozoic (Almeida et al., 2000; U. G. Cordani et al., 2016). The South American Platform was formed by the amalgamation of several Archean and Proterozoic continental blocks which individually assembled during Paleo-Mesoproterozoic tectonic events. The Neoproterozoic Brasiliano cycle brought together the separate blocks, resulting in formation of the Gondwana Supercontinent, and determined the general tectonic framework of the platform basement (Figure 1).

The platform consists of the Archean to Proterozoic Amazonian and São Francisco cratons, other microcontinents (São Luis, Rio de la Plata, Luíz Alves and Rio Apa), and the Paranapanema and Parnaíba blocks covered by the Paraná and Parnaíba Paleozoic basins. The Amazonian Craton is formed by a large Archean core surrounded by Paleoproterozoic and Mesoproterozoic mobile belts with an indication of crustal growth progressing from NNE to SSW (U. G. Cordani & Teixeira, 2007). The westernmost portion of the Amazonian Craton presents important affinities with the Grenville Belts in North America, linking the tectonic evolution of the block to the Laurentian continent (e.g., Brito Neves & Fuck, 2014; U. Cordani et al., 2009; D'Agrella-Filho et al., 2012). Paleomagnetic data also favors that the Amazonian Craton was joined to the Columbia supercontinent (D'Agrella-Filho et al., 2016). In contrast, the basement of the São Francisco Craton is an extension of the Congo craton of western-central Africa (Trompette, 1994), and is made up of Archean blocks that were extensively affected by Paleoproterozoic orogenic episodes during their almagamation (e.g., Pankhurst et al., 2008). Although it is generally agreed that the Amazonian Craton was an integral part of Rodinia, linked to Laurentian blocks, it is debated whether the other South American cratonic blocks (São Francisco-Congo, Rio de la Plata and São Luis cratons) were part of this continent, and if so, if they were adjacent to the Amazon craton at that time (Brito Neves & Fuck, 2014; Oriolo et al., 2017).

The Brasiliano Cycle (e.g., U. G. Cordani et al., 1973; Da Silva et al., 2005; Neves et al., 2014) started during the process of fragmentation of the Rodínia supercontinent. During the extensional phase (1000-750 Ma, Oriolo et al., 2017; U. G. Cordani et al., 2003), the Amazonian block was separated from Laurentia and further oceans opened between other continental blocks where those were still joined. Associated with the extension, passive margins formed and intraplate magmatism occurred. During the subsequent compressional phase (930-530 Ma, De Brito Neves et al., 1999; Neves et al., 2014), subduction-to-collision brought together South American and African continental blocks to form West Gondwana. During this process, the orogenic belts of the Brasiliano Orogenic Systems (900-460 Ma) were formed around the cratonic cores, resulting in the Borborema (between São Francisco and Parnaiba), Tocantins (between São Francisco and Paranapanema) and Mantiqueira (between Rio de la Plata and Paranapanema) Structural Provinces. Other expressions of the assembly of western Gondwana include the Transbrasiliano Lineament (TBL) (Almeida et al., 2000; U. Cordani et al., 2000), a continental NE-SW shear zone with a clear surface expression, and the Western Paraná Suture Zone (WPSZ), a geophysically identified east-ward dipping suture zone between the Paranapanema Block and cratonic blocks to the west and south (Dragone et al., 2017, 2021). The end of the Brasiliano Cycle was characterized by exhumation, extrusive volcanism and gravitational collapse of the orogens under an extensional tectonic regime (630-440 Ma, Fuck et al., 2008; Heilbron & Machado, 2003).

After the platform was tectonically stabilized at the end of the Brasiliano phase, several Paleozoic intracontinental basins developed: the Amazonas, Solimões, Parnaíba, Parecis, Paraná, and Alto Tapajós (e.g., Almeida et al., 2000; Milani & Zalán, 1999). The Paleozoic basins went through two main phases. During the first phase (420 - 250 Ma), the synclines were formed and sedimentary successions were produced by transcontinental marine transgressions and regressions. During the second phase (250 - 230 Ma), there was a general uplift of the platform, associated with thin eolian deposits (e.g., P. C. Soares et al., 1978; Góes et al., 1990; Da Cruz Cunha et al., 2007).

The Intracratonic Stability phase was followed by Mesozoic re-activation, associated with the fragmentation of the Pangea Supercontinent and the opening of the Atlantic Ocean. During this extensional regime, magmatism occurred in most of the sedimentary basins of South America. Magmatism in the Parecis, the Solimões and Amazonas basins belongs to the Central Atlantic Magmatic Province (CAMP, 206-196 Ma), and is related to the opening of the Central Atlantic Ocean (de Min et al., 2003; Marzoli et al., 1999). Another major extrusion event created the Paraná-Etendeka Large Igneous Province (LIP) covering part of eastern South America and western Africa and is related to the opening of the South Atlantic Ocean. The main peak of this LIP magmatic activity occurred between 135–120 Ma (e.g., Gibson et al., 2006; Renne et al., 1992, 1996; Mizusaki et al., 1992). In South America, it formed the large continental flood basalts of the Serra Geral Formation, which covers most of the Paraná Basin (Milani & Ramos, 1998; Milani, 2004).

After the opening of the Atlantic Ocean in the Late Cretaceous, the South American Plate rotated to the west. The movement of the plate increased its convergence rate with the subducting Farallon Plate, and initiated a new compressional phase in South America (e.g., Ramos, 1999; Pilger, 1984; Ramos, 2009; Folguera et al., 2011; Almeida et al., 2000). With uplift and exhumation of the Andean Cordillera, several foreland basins developed parallel to the Andean thrust front, such as the Chaco and Pantanal basins, and deposits were formed over Paleozoic basins on the platform (e.g., Menegazzo et al., 2016; Horton, 2018; Cedraz et al., 2020; Ussami et al., 1999).

1.3 Previous Studies of Lithospheric Structure

Constraints on crustal and lithospheric mantle structure beneath the South American Platform have been obtained using a range of geophysical methods. Continental scale studies in the region include gravity-derived Moho depths (van der Meijde et al., 2013; Uieda & Barbosa, 2017), and seismic tomographic models based on waveform modelling or surface wave dispersion (van der Lee et al., 2001; Feng et al., 2004, 2007; Heintz et al., 2005; Rosa et al., 2016; Celli et al., 2020; Ciardelli et al., 2022). Regional scale studies include deep seismic refraction studies in the Tocantins Province (Berrocal et al., 2004; J. E. Soares et al., 2006), Borborema Province (J. E. P. Soares et al., 2011), and Parnaíba Basin (Daly et al., 2014; Abbott, 1991), and several P-wave receiver function analyses (e.g., Albuquerque et al., 2017). Other studies provide crustal thickness maps based on

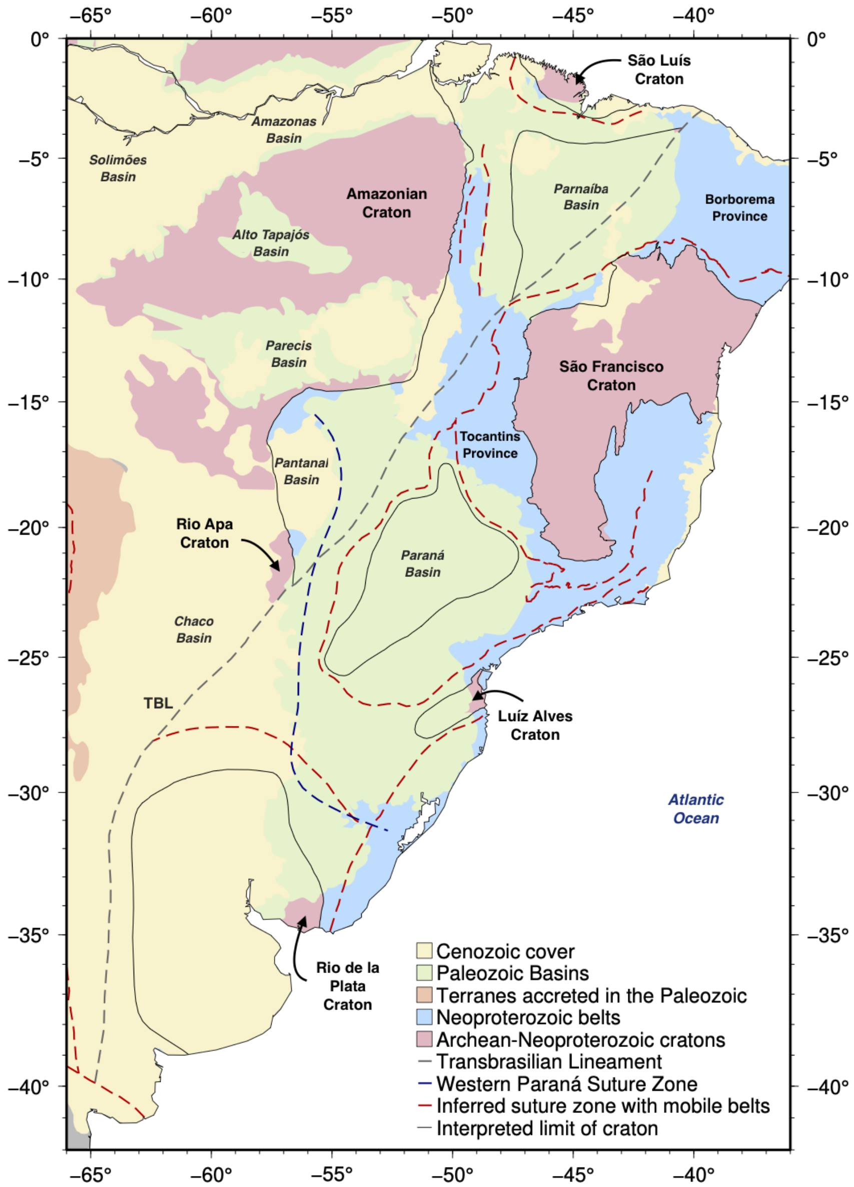

Figure 1. Simplified tectonic map of the South American Platform adapted from U. G. Cordani et al. (2016). The thin black lines are the interpreted boundaries of the cratons. The dashed red lines are the main inferred suture zones. The grey dashed line is the Transbrasiliano Lineament. The blue dashed line is the Western Paraná Suture Zone (adapted from Dragone et al., 2021). Paleozoic sedimentary basins are adapted from IBGE (2010).

the joint inversion of the different geophysical constraints (Lloyd et al., 2010; Assumpção et al., 2013; Rivadeneyra-Vera et al., 2019).

The extent of the cratonic basement below the thick sedimentary cover on much of the platform is not agreed on. Geophysical studies indicate that the Parnaíba Basin is underlain by a Proterozoic basement, the Parnaíba Block (Daly et al., 2014). Below the Paraná Basin, the Paranapanema Block has been identified, for which the crust appears to be a mosaic of cratonic blocks surrounded by mobile belts (Milani, 2004; Julià et al., 2008), while it looks like a single cratonic block at lithospheric scale (U. G. Cordani et al., 2008; Affonso et al., 2021; Mantovani et al., 2005). Others proposed that cratonic blocks include the Rio Tebicuary (Favetto et al., 2015; Dragone et al., 2017) and part of the Rio de la Plata craton overlain by the Chaco Basin (Oyhantçabal et al., 2010; Rapela et al., 2007, 2011; Bologna et al., 2019; Dragone et al., 2017). These cratonic blocks would also have been part of the West Gondwana amalgamation during the Neoproterozoic (Dragone et al., 2021).

The most recent crustal thickness model for South America (Rivadeneyra-Vera et al., 2019) indicates that the crustal thickness in the platform varies between 30 to 45 km. The Amazonian and São Francisco cratons, and the Parnaíba Basin are on average 40 km thick, while the crust of the Borborema and Tocantins provinces are thinner than average, under 37 km thick. The Pantanal Basin has a thin crust in the east (30-35 km) and an average crust in the west (38-43 km), similar to the Rio Apa Block. The Paraná Basin crust is somewhat thicker (40-45 km), especially in the north, which is interpreted as due to magmatic underplating related to the emplacement of the flood basalts.

The seismic structure of the uppermost mantle of the South American Platform is also significantly controlled by the tectonic evolution. All continental tomographic models show a high velocity lid associated with the Amazonian and São Francisco cratons extending down to about 200 km depth, which some suggested might be thinner than North American cratonic cores (van der Lee et al., 2001; Feng et al., 2004; Heintz et al., 2005; Feng et al., 2007; Rosa et al., 2016; Celli et al., 2020). Heintz et al. (2005) and Ciardelli et al. (2022) imaged a lower velocity anomaly in the uppermost 100 km along the Amazon and Solimões rift basins that divides the high velocity anomaly associated with the Amazonian craton. They suggest that the Lower Cretaceous rifting episode within the Amazon Basin has involved a significant part of the lithosphere. However, other studies (Feng et al., 2007; Celli et al., 2020) found that the Amazon Basin lithosphere is underlain by high velocities similar to the surrounding shields, indicating continuity between them. The same studies also find that the lithosphere of the eastern Amazonian Craton is thicker and higher velocity than the northwestern part. Feng et al. (2007) inferred that the high-velocity root below the southeastern Amazonian Craton is more pronounced and thus thicker than below São Francisco. By contrast, a joint interpretation in terms of temperature and Mg# of the lithospheric mantle by Finger et al. (2021), using the shear velocity model of Celli et al. (2020), gravity data from Förste et al. (2014), and crustal data from Rivadeneyra-Vera et al. (2019), found similarly thick thermal lithosphere and iron-depletion below the São Francisco and the eastern Amazonian cratons.

High velocities down to $\sim$150 km depth have also been imaged below the Parnaíba, Parecis and northern Paraná basins (Heintz et al., 2005; Feng et al., 2007; Rosa et al., 2016; Celli et al., 2020; Ciardelli et al., 2022). The high velocities below northern Paraná have been suggested to show that the plume interaction with the Paraná Basin lithosphere, which resulted in the flood basalts, did not significantly modify the overall seismic properties of the Paraná cratonic lithosphere (Heintz et al., 2005; Feng et al., 2007). This is consistent with the thermo-chemical interpretation by Finger et al. (2021) who found a thermal structure and Fe-depletion below northern Paraná similar to the São Francisco lithosphere. While a similar structure is also found below the Parecis Basin, they found no indication for Fe-depletion in the lithosphere below the Parnaíba Basin.

Some studies have identified a localised low-velocity anomaly at depths > 200 km below the southern part of the Paraná Basin, which they suggest could be a fossil expression of the Tristan da Cunha plume (Heintz et al., 2005; Van Decar et al., 1995). Further strong low velocity anomalies down to 150 km depth have been imaged beneath the Chaco, Pantanal, and western Paraná basins (Feng et al., 2004, 2007; Heintz et al., 2005; Rosa et al., 2016; Celli et al., 2020; Ciardelli et al., 2022). These low velocities have been interpreted as thinner lithosphere, and relatively high mantle temperatures (Feng et al., 2007; Rosa et al., 2016; Finger et al., 2021).

Most studies have not found evidence of a thick thermal keel below the Rio de la Plata Craton, in spite of its suggested large lateral extent below the sedimentary cover (Feng et al., 2007; Heintz et al., 2005; Celli et al., 2020). However, a recent group-velocity analysis (Rosa et al., 2016), which used an expanded dataset around the Paraná and Chaco basins, improved the resolution in northern Argentina and southern Brazil. Differently from the previous studies, they identify high velocities under the southeastern part of the Rio de la Plata Craton. Finger et al. (2021) also inferred that the lithosphere below this southern craton, although relatively thin, is partly Fe-depleted.

Several studies, (Feng et al., 2004, 2007; Celli et al., 2020; Ciardelli et al., 2022) found a belt of lower velocities at 100-200 km depth, stretching from the eastern Parnaíba Basin and Tocantins Province in the north to just east of the Pantanal Basin in the south. This was interpreted as a lithospheric expression of the Transbrasiliano Lineament.

2 Data and Methods

Our analysis consists of the joint fitting of thermo-compositional structures to Rayleigh wave group-velocity dispersion data, topography, and geoid, with constraints on the crustal structure (Figure 2). These three data types provide strongly complementary constraints (sensitivity tests are discussed below and in work by Afonso et al. (2008)). The set of thermo-compositional structures tested includes a wide range of steady-state continental geotherms plus a minimum amount of compositional complexity as required to match seismic velocities and density-sensitive data.

2.1 Data

The dispersion data used in this study consist of a set of Rayleigh-wave dispersion curves extracted from group-velocity maps by Rosa et al. (2016) (Figure 2a). The group-velocity maps were derived with surface-wave tomography using a combination of earthquakes covering the South American continent and inter-station cross-correlation of ambient noise for stations in and around the Paraná and Chaco-Paraná basins. The Rosa et al. (2016) study includes, for the earthquake data, fundamental-mode group velocities for Rayleigh waves from 10 to 150 seconds, and Love waves from 10 to 90 seconds. For the ambient noise correlation, they used periods from 10 to 40 seconds for both Rayleigh and Love waves. In this study, we model the Rayleigh waves in terms of thermo-chemical structures using a simple radial anisotropy model for all regions. For the Love waves, we calculate the synthetics and evaluate the misfits in the discussion. From the original study, we removed the period 10 seconds from both Rayleigh and Love waves, as it is most sensitive to the crust, and we analyse only the area within the South American Platform where resolution tests show amplitude recovery to be good.

The short periods of the Rayleigh waves are also sensitive to the crustal structure. Because crustal structure is mainly controlled by compositional variations with little sensitivity to temperature, we use independent constraints for the velocity and density structure of the crust (Altoe et al., 2020; Eeken et al., 2020). Given the limited depth sensitivity of the data we model, we use a simplified crustal model with only an upper and lower crust. The crustal constraints necessary to do our modelling are Moho depth, V_P,

V_S, and density for upper and lower crust. Crustal thickness estimates are taken from Rivadeneyra-Vera et al. (2019) (Figure 2b), and the other information is retrieved from the global crustal model CRUST1.0 (Laske et al., 2013). To account for the uncertainties in the crustal structure, we allow Moho depth to vary by $\pm$ 2 km and lower crustal V_S to vary by $\pm$ 500 m/s (Supplementary Table S3).

For the density-sensitive data, elevation data was taken from the ETOPO1 Global Relief Model (Amante & Eakins, 2009) (Figure 2c). Geoid height data was obtained from the global Earth model EGM2008 (Pavlis et al., 2012) (Figure 2d). The total geoid signal was filtered to remove long wavelengths which mainly reflect deeper density anomalies and dynamic effects (degrees 2–9 were removed) (Afonso et al., 2008, 2019).

2.2 Regionalization

In the analysis, it is important to bear in mind the limits on lateral resolution of the data we use. For the dispersion data, structures can be mapped on scales of 100-200 km due to both intrinsic data sensitivity and the regularisation applied in the group velocity inversion. CRUST1.0 (Laske et al., 2013) provides an estimate of crustal structure on a 1° by 1° grid. To account for this scale of lateral resolution, we regionalise our data. We base the regionalisation on the group velocity data using a cluster analysis. The preferred six dispersion-based clusters were further subdivided into a final 14 groups where this was necessary to accommodate significant variations in topography, geoid or crustal structure within a cluster.

Similar to previous seismic studies (e.g., Eeken et al., 2020; Altoe et al., 2020; Garber et al., 2018; Lekic et al., 2012), we use the k-means algorithm to identify regions with similar group velocity structure. We use the MATLAB implementation of the k-means clustering algorithm (Hartigan & Wong, 1979; Hartigan, 1975). We found the optimal number of Rayleigh wave dispersion clusters to be 6 (Figure 3a). For this number of clusters each region's dispersion curve is distinct (Figure 3b). Furthermore, the clusters are compatible with the tectonics (also see Supplementary Table S1 and Figure S1). When the dispersion curves are divided into two clusters, they split into a set for the the Amazonian, São Francisco, and Rio de La Plata cratons, as distinct from the rest of the region. For three clusters, the coastal margin of the São Francisco Craton is grouped with the Rio de La Plata Craton. A further subdivision into four clusters includes a new group with the Paraná and Parecis basins. The solution for five clusters groups the southernmost part of the Rio de la Plata Craton back with the Amazonian and São Francisco cratons, and a new cluster includes part of the mobile belts of the east coast, the Pantanal Basin region and the northwestern part of the Rio de la Plata Craton. Six clusters adds a further subdivision for the Chaco Basin and the Luiz Alves Craton. The solution for seven clusters does not add a further distinct region, but generates a transition zone between the São Francisco Craton and its coastal margin. Furthermore, for sets of more than 6 clusters, the differences between clusters become similar in magnitude to the differences between profiles within a single cluster. The quality of the final clustering was also assessed by silhouettes (Rousseeuw, 1987; Kaufman & Rousseeuw, 1990). All the points with negative silhouette values and points that were geographically isolated from their clusters were removed from further analysis (Supplementary Figure S1).

The clusters were further subdivided into 14 groups, based on the elevation, geoid and crustal thickness of the regions (Figure 1a). Figure 3b shows the final regionalisation with their respective average dispersion curves. Period-dependent uncertainty bounds were calculated based on the standard deviation of the dispersion data and increased by 50% for periods longer than 60 seconds, to accommodate the, physically unrealistic, high variability of velocity with period in the data (which could occur because the dispersion map inversion included no smoothing with period). The same uncertainties were assigned

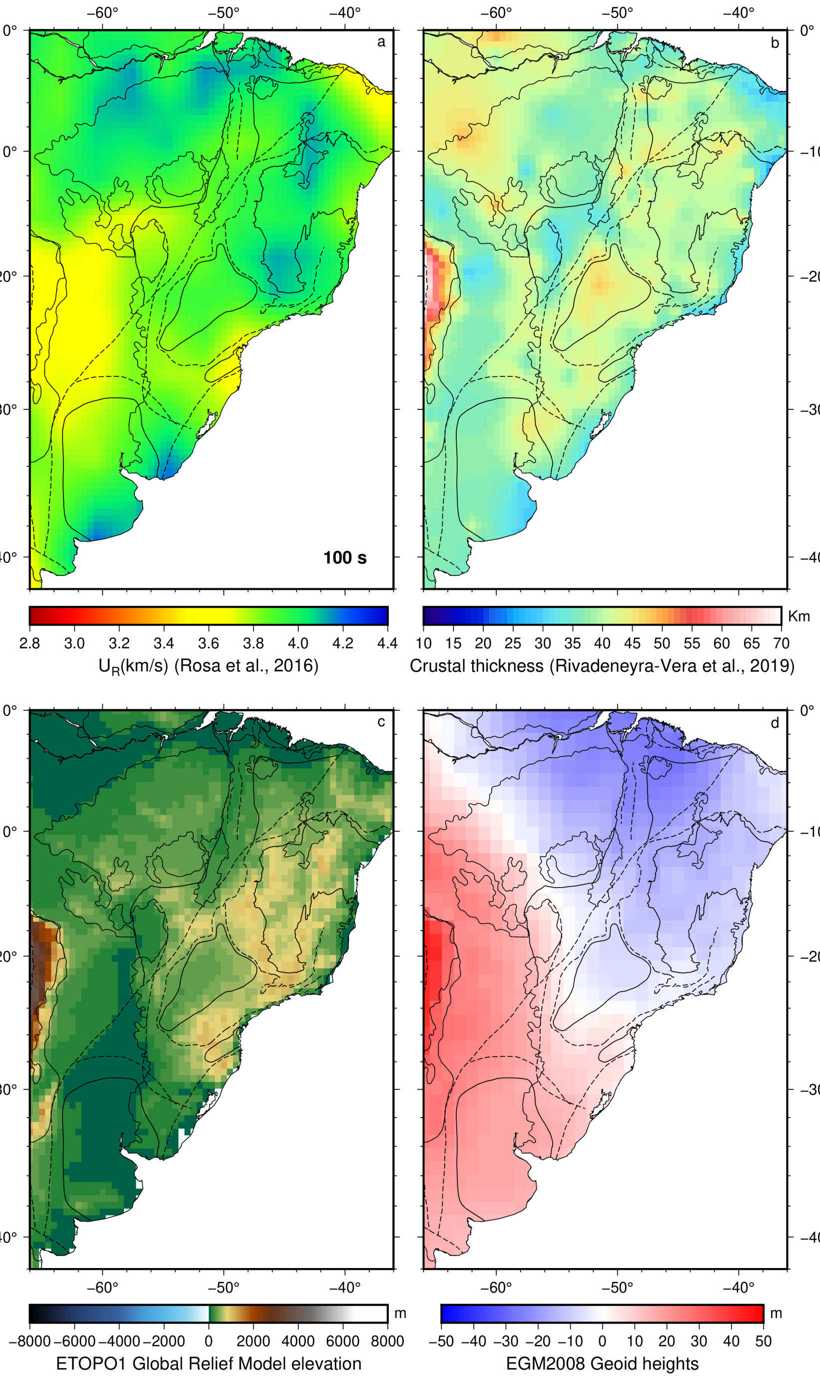

Figure 2. Overview of the data used in our analysis: (a) Rayleigh-wave group-velocities at 100 seconds from Rosa et al. (2016). (b) Crustal thickness from Rivadeneyra-Vera et al. (2019). (c) Topography from Amante and Eakins (2009). (d) Geoid height from Pavlis et al. (2012).

to all groups. The elevation and geoid anomaly for each group equal the average value, with the standard deviation of the region as uncertainty (Figure 3c and d).

2.3 Grid-search for Thermo-chemical Models

The thermo-chemical structure of the regions is estimated by performing a grid-search for a set of forward models that fit the dispersion curves, topography, and geoid anomalies within their uncertainties. The general approach used in this study follows the methods of Altoe et al. (2020) and Eeken et al. (2018, 2020), with an extension to fit density-sensitive data. The approach can be divided into 4 basic steps (Figure 4).

1. We define a solution space of thermal and compositional mantle lithosphere/asthenosphere structures to search, while fixing crustal structure to within a narrow range based on published studies. We chose a set of plausible shield geotherms spanning a range of thermal lithospheric thicknesses by varying Moho heat flow (as we do not use thermal structure of the crust to match any data). For the chosen lithospheric/asthenospheric mantle composition, we compute phase diagrams as a function of pressure and temperature using the Gibbs Free-energy minimization code PerPleX (Connolly, 2005) with the data base HP02 (Holland & Powell, 1998).
2. Each thermo-chemical structure is converted into seismic velocities and density using the thermodynamic database from Abers and Hacker (2016), with an added temperature-, pressure- and frequency-dependent anelasticity correction (anelasticity model QF from Faul & Jackson, 2005). We also impose a depth gradient in radial anisotropy (similar to PREM), from 4% at 40 km depth to 0% at 220 km. The synthetic mantle profiles are then combined with the crustal model and, below 400 km depth, the global seismic reference model AK135 (Montagner & Kennett, 1996).
3. For the thus calculated synthetic seismic and density profiles, the code MINEOS (Masters et al., 2011) is used to obtain group velocity dispersion curves for the Rayleigh-wave fundamental mode. Elevation and geoid anomaly are calculated assuming local isostasy and using a 1-D isostatic geoid formulation, as described below.
4. Finally, we use a grid search to find all models that fit the average dispersion curves, elevation, and geoid anomalies for the different regions.

2.3.1 Thermal Structure

The thermal solution space consists of 1-D steady-state geotherms that span a range of plausible steady-state thermal structures for shield mantle lithosphere. As discussed in more detail in Eeken et al. (2018), there are several trade-offs between the different thermal parameters that define the geotherms, which guided us in deciding which parameters are kept fixed or varied. In this study, we vary Moho heat flow and potential temperature of the asthenospheric adiabat to span a wide range of thermal structures and, in particular, lithospheric thicknesses (Supplementary Table S2). The thermal lithosphere thickness is here defined as the depth where the conductive geotherm and mantle adiabat intersect, and we allow it to vary from 90 to 360 km depth. We test for a range of potential temperatures, from usual MORB-source mantle temperatures of 1300°C, to cooler potential temperatures of 1100°C (Herzberg et al., 2007). The chosen range of Moho heat flow values (10-35 mWm^{-2}) combined with the integrated crustal heat production can generate the observed range of surface heat flow on cratonic regions. Because our method does not constrain the crustal part of the geotherms, we prefer to analyse the Moho heat flow of our solutions rather than the surface heat flow.

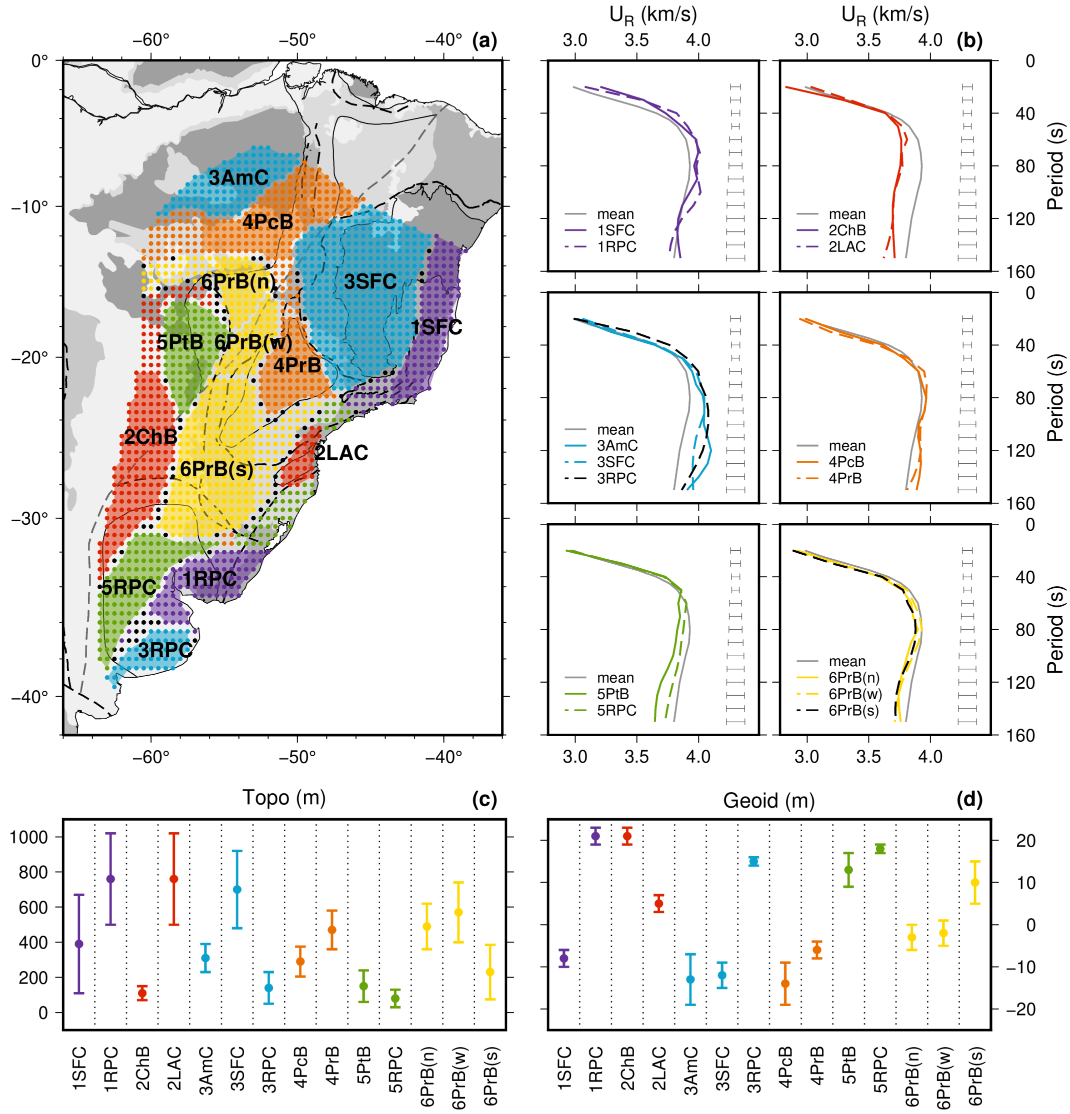

Figure 3. (a) Map showing the grid nodes of the group-velocity map (from Rosa et al., 2016) with the final regionalisation based on the cluster analysis (represented by the different colours and numbers), and further subdivision into groups (solid shading) based on variations in crustal thickness, topography and geoid height. Abbreviations used: AmC - Amazonian Craton, SFC - São Francisco Craton, RPC - Rio de la Plata Craton, LAC - Luíz Alves Craton, PrB - Paraná Basin, PcB - Parecis Basin, PtB - Pantanal Basin, ChB - Chaco Basin. Points with a negative silhouette value (in black), and points not assigned to any group (without coloured shading) were not included in our subsequent modelling. (b) Average dispersion curve for each group, compared with the average dispersion curve for all groups (grey curve). Error bars to the right of the dispersion curves are the period-dependent uncertainties that were used in the subsequent thermo-chemical modelling. (c) Average topography and (d) geoid height for each group with their respective standard deviations.

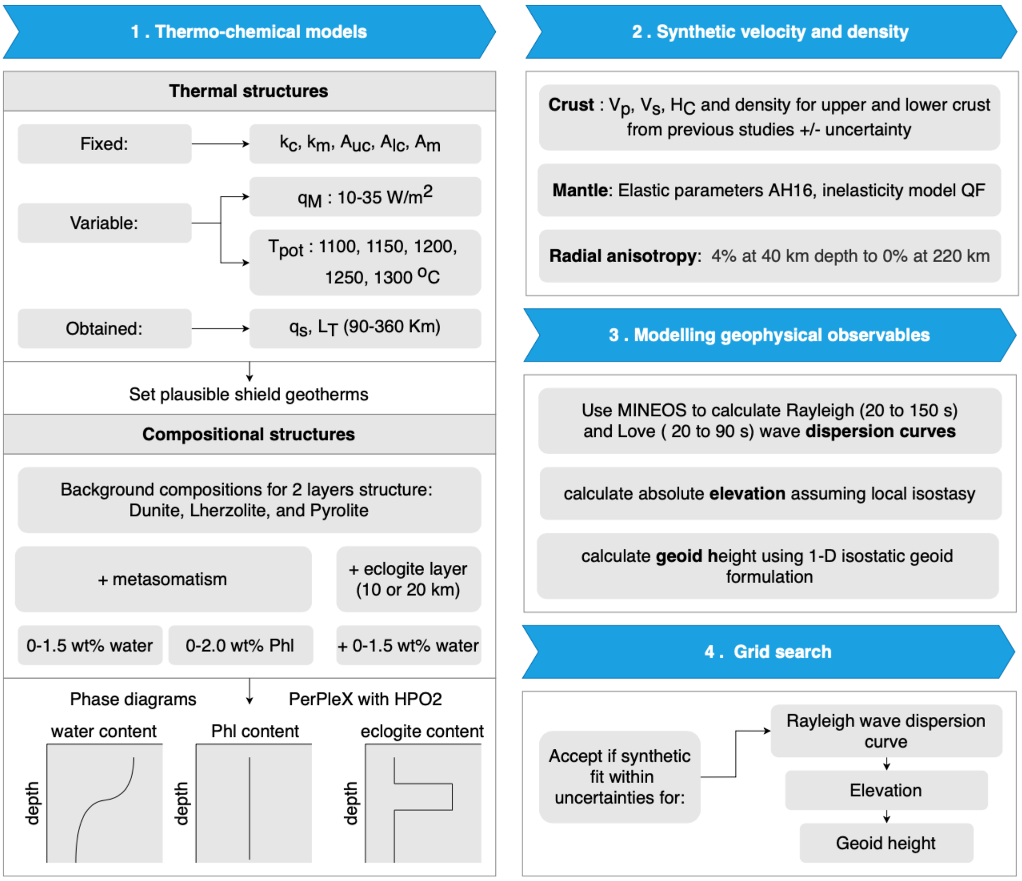

Figure 4. Flow diagram summarizing how the grid search for thermal and compositional structures that match group velocities, topography and geoid anomalies is conducted.

2.3.2 Compositional Structure

Density-sensitive topography and geoid in cratonic areas require that the lithosphere comprises a background composition that is lighter than the underlying peridotitic mantle (e.g., Jordan, 1978; Griffin et al., 2009). We test three background compositions with distinct densities: a relatively low-density refractory dunite (ARC9 in Griffin et al., 2009), an intermediate-density somewhat refractory lherzolite (ARC4 in Griffin et al., 2009), and a fertile peridotite (pyrolite in Xu et al., 2008) as expected in the asthenospheric mantle. We tested models composed of two lithospheric layers, with an interface at various depths, for all combinations of background compositions for top and bottom layers. The depth of the background layers varies according to the lithospheric thickness and the interface is usually located at 50, 60, or 70 km for a thin lithosphere and at 80, 120, 160, 200, or 240 km depth for a thick lithosphere. Our data do not have the resolution for finer scale background structure than this. The differences in group velocities for these end-member background compositions are subtle and therefore can not account for the wide range of velocities in the region. Therefore, we add to our models eclogite and metasomatic compositions, which are the most common seismically fast and slow mineralogies found in xenoliths (e.g., Pearson et al., 2013) (Supplementary Tables S4 and S5).

Eclogite could represent oceanic crust trapped in the lithosphere during its assembly, or solidified mantle melt added later. Eclogite layers of a thickness compatible with that of oceanic crust (between 6 and 20 km depending on whether produced at present-day or at Archean/Proterozoic mantle temperatures (Weller et al., 2019)) are consistent with high-velocity layers imaged in several cratons, including the Slave (Bostock, 1998), Wyoming (Hopper & Fischer, 2015) and Superior cratons (Eeken et al., 2020; Altoe et al., 2020), and mid-lithospheric discontinuities with a positive velocity-depth contrast (e.g., Miller & Eaton, 2010; Abt et al., 2010). We test structures with an added layer of basaltic composition, which is substantially faster than the background compositions once the eclogite stability field has been entered (below about 70 km depth depending on the geotherm). The layer of eclogite is either 10 or 20 km thick and positioned at various depths. We use the MORB bulk composition from Hacker (2008). Other compositions may have somewhat different velocity and density structures (Garber et al., 2018), but our data have no resolution to distinguish between them.

Metasomatic compositions are the most plausible seismically slow compositions expected under cratons (Bruneton et al., 2004; Selway et al., 2015; Eeken et al., 2018). We test for two common types of metasomatism, that lead to different velocity-depth distributions. Adding only water as a metasomatic agent to our background compositions, amphibole, antigorite, chlorite, chloritoid and talc stabilise at depths above 100-150 km. For depths greater than that, we assume the free water escapes and does not influence the calculated seismic velocities or attenuation. When some potassium is added in addition to water, phlogopite mica is formed and stays stable throughout the lithosphere. In most cases, we imposed a linear gradient from a maximum of phlogopite below the Moho to none at the base of the thermal lithosphere. In previous studies, we found that such a decrease in the degree of alteration with increasing depth was generally required to match the seismic observations. However, here we also tested cases where the two layers of background compositions had a constant phlogopite content, which differed between the layers. As metasomatic compositions, we tested for cases with 0.1, 0.25, 0.5, 0.75, 1.0, and 1.5 wt% water added to the top background layer. And we tested for 1, 2.5, 5, 7.5 and 10% phlogopite, as the amount within the background layers, which was allowed to differ between the two layers. We also tested for all combinations of background composition above and below the eclogite layer, with or without the addition of water in the top layer.

2.4 Elevation

We compute the elevation assuming the principle of local isostasy (Turcotte & Schubert, 2002), which implies that the surface elevation at a point depends only on the average density of the column below that point. It also implies that the total mass in vertical columns from the surface to a certain depth, referred as common compensation level, should be equal. If we assume that the effects of the sublithospheric density variations are negligible, then the common compensation level can be placed at the base of our model (∼360 km), which covers the whole range of estimated lithospheric thicknesses for the study region.

The condition of isostasy can be written in function of density distribution as in Equation 1, where h is the common compensation level, and $\Delta\rho$ is the anomalous density with respect to a reference column at depth y. We use as reference column, a model of a mid-oceanic ridge (MOR), composed of an 3 km water column ($\rho = 1020\ kg/m^3$), a 7 km oceanic crust ($\rho = 3000\ kg/m^3$) overlying a pyrolitic mantle along an adiabatic geotherm with a potential temperature of 1330°C appropriate below a mid-ocean ridge (F. D. Richards et al., 2018; F. Richards et al., 2020).

$$\int_0^h \Delta\rho\,(y)\,dy \ = 0 \tag{1}$$

2.5 Geoid Height

The geoid is the Earth's gravity equipotential surface, which coincides with sea level in the ocean (Turcotte & Schubert, 2002). The deviation from this surface and the International Reference Ellipsoid is called geoid anomaly or geoid height. The geoid height can be calculated using the 1-D isostatic geoid formulation given by Turcotte and Schubert (2002) in Equation 2, where $\Delta\,N$ is the geoid heigh, G is the gravitational constant, and g is the normal gravity acceleration. While topography depends only on integrated density in a column, the geoid height is also influenced by the depth of the density anomaly and thus provides additional constraints on the distribution of density with depth. The calculation requires a reference column, for which we chose an oceanic region near the South American eastern margin where geoid height equals zero. To model the reference column, CRUST1.0 (Laske et al., 2013) was used for the crustal structure and we searched for a thermal lithospheric thickness that fits the elevation data for the region (using harzburgite as lithospheric composition and a mantle potential temperature of 1300°C, the same as what we use as highest potential temperature below the study region).

$$\Delta\,N = -\frac{2\pi\,G}{g}\int_0^h y\,\Delta\rho\,(y)\,dy \tag{2}$$

2.6 Sensitivity Analysis

Rayleigh-wave group velocities, elevation, and geoid anomalies have different sensitivities to thermal and compositional structure, and thus they work as a complement to each other (Figure 5, see also Supplementary Figure S2). Rayleigh-wave group velocities are especially useful to estimate the thermal lithosphere thickness. Differences in group velocities for geotherms with q_m of 12 mWm^{-2} and 30 mWm^{-2} are as high as 0.23 km/s (at larger periods ∼120 s, Figure 5d). The group velocities are also somewhat sensitive to the different types of metasomatism. The minerals that form due to the addition of only water can slow group velocities as much as 0.19 km/s at short periods (∼50s, Figure 5p) compared to a dry composition, while the addition of phloglopite has a similar effect extending to mid to long periods. The addition of a layer of eclogite has only a small effect on the group velocity (an increase of a maximum 0.025 km/s). Thus, in

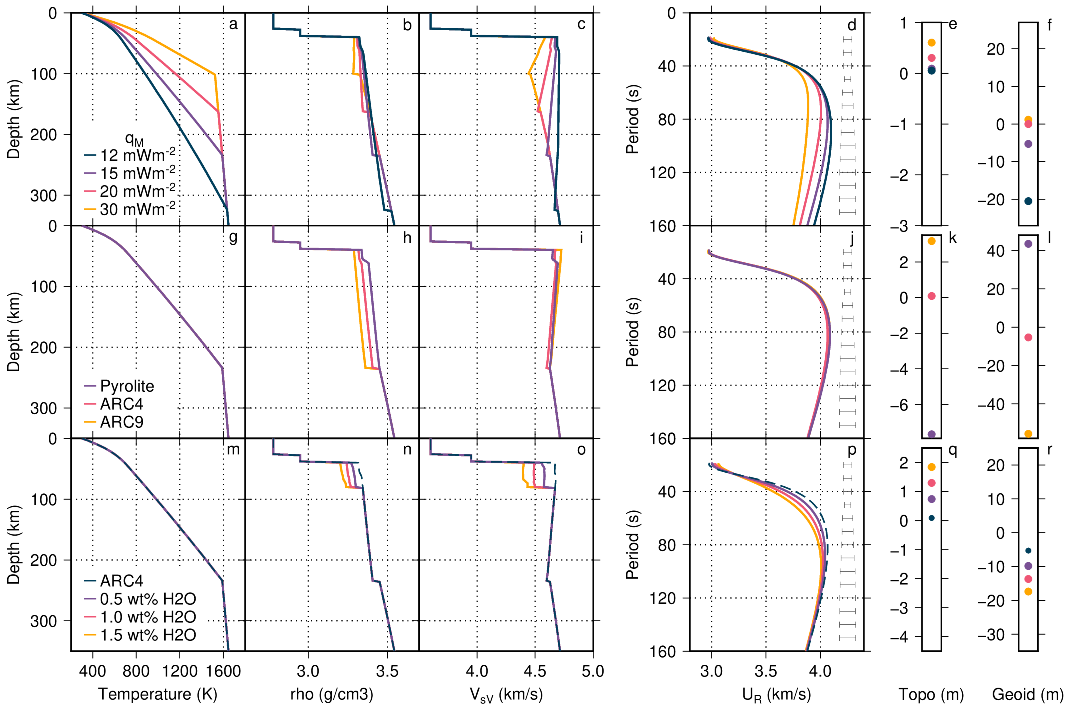

Figure 5. Sensitivity analysis of Rayleigh-wave group-velocity dispersion curves, topography, and geoid height to different Moho heat flow (top row), background composition (middle row), and water content (bottom row). For each set of tests, the three left hand columns show the geotherms (a, g, and m), the density (b, h, and n) and the velocity profiles (c, i, and o). The three right hand columns show the effect of the different thermal and compositional structures on the Rayleigh-wave group velocities (d, i, and p), topography (e, k, and q) and geoid (f, l, and r).

contrast to Rayleigh wave phase velocities (Altoe et al., 2020; Eeken et al., 2020), group velocities are not very sensitive to the high-velocity layers tested. Also, although dispersion data has more depth sensitivity than teleseismic travel time tomography, the dispersion data's integrated sensitivity to depth puts limits on the resolution to the depth distribution of compositional layers (Eeken et al., 2020).

Once the lithosphere thickness range is constrained by matching the dispersion curves, the fits to elevation and geoid height are mostly accomplished by varying compositional structure. Relatively low-density compositions, like ARC9 and metasomatic minerals, have a positive effect on elevation and a negative effect on geoid height. In contrast, high-density compositions, including pyrolite and eclogite, have a negative effect on elevation and a positive effect on geoid height. A modelled thick continental lithosphere composed solely of a fertile or refractory composition yields unrealistic elevation and geoid height values Figure 5k and l. Therefore, we test for layered models and/or an intermediate composition (ARC4). The geoid height offers some constraint on the depth distribution of density, where the deeper the layer, the higher the effect on the geoid height.

2.7 Example Set of Solutions

As an example of the results from the grid search process, we present a set of solutions for Group 3 (São Francisco Craton) for a sublithospheric potential temperature of 1200°C and without the addition of an eclogite layer (Figure 6; for the solutions for other regions see Supplementary Figures S3 to S16). Out of the 51597 models searched, 1253 fit the Rayleigh-wave group-velocities (solutions in gray). Of those solutions, 111 fit the topography (solutions in blue), and 38 also fit the geoid height (solutions in red), within their respective uncertainties (Figure 6d, h, and i).

For the accepted solutions, the base of the thermal lithosphere (i.e., depth at which the geotherm intersects the mantle adiabat) ranges from 220 to 270 km depth (Figure 6a). The density profiles (Figure 6b) illustrate the difference in density between the background compositions and the depth of the interface between the two layers (at 80, 120, and 160 km depth). The addition of water leads to relatively low densities (Figure 6b) and velocities (Figure 6c) directly below the Moho. Lower velocities due to alteration are required to match the Rayleigh-wave dispersion curve as no solutions are found for any of the dry compositions (Figure 6d and j). Although we do not try to fit the Love-waves in our grid-search, we include the forward models to illustrate to what extent our solutions match these data (Figure 6f and g). In this case, many of the solutions do match the Love-wave dispersion as well, although the data may prefer somewhat stronger radial anisotropy than we imposed (yielding higher V_{SH}).

The water content versus background composition graph (Figure 6j) illustrates the compositional solution space and the trade-offs between these two compositional parameters. ARC9 is seismically slightly faster than ARC4 or pyrolite, and thus requires a higher water content to achieve the same low velocities on the top of the lithosphere as the other two compositions. Meanwhile, pyrolite, which is a high-density composition, requires a higher water content to achieve the same densities as ARC4 or ARC9.

The characteristics of the accepted thermal structures are illustrated by the range of lithospheric thicknesses and Moho heatflow values. Considering the wide range of Moho heat flow values and thermal lithosphere thickness that are tested, we only find solutions for a relatively small range of those parameters (Figure 6k and l) with relatively large thermal thicknesses and low Moho heat flow.

3 Results

The majority of the regions have solutions that fit all geophysical observables. However, regions 2LAC, 2ChB, and 5PtB have no solutions that fit both the elevation and geoid height. Regions 1SFC and 1RPC were not analysed because even with the increased error bars, their dispersion curves have large jumps in group velocity with period that can not be matched with any physical model, probably because these regions are at the edge of the path-covered area of the seismic tomography model, where resolution is lower (Rosa et al., 2016).

3.1 Overview

The results reveal a large variation of lithospheric thickness across the platform, as well as four distinct classes of compositional structures. Lithospheric thickness solutions vary between 100 and 300 km depth, and the mantle potential temperature ranges from 1150°C to 1300°C across the study area. While some regions require a specific potential temperature to fit the observations, other regions have solutions for several of the sublithospheric temperatures tested (Figure 7). It would be difficult to maintain different temperatures between close areas within the convecting asthenosphere. Therefore, we chose as the preferred set of solutions those where the sublithospheric temperature was similar to/the same as that of neighbouring areas. The final preferred set of solutions has asthenospheric temperatures of 1200°C to 1250°C below the northern, central, and southern areas (regions 3AmC, 3SFC, 4PcB, 4PrB, 6PrB(n), 6PrB(w), 6PrB(s), 5RPC, and 3RPC), and warmer temperatures of 1250°C to 1300°C below the eastern coast and the western limit of the study region (regions 2LAC, 5PtB, and 2ChB).

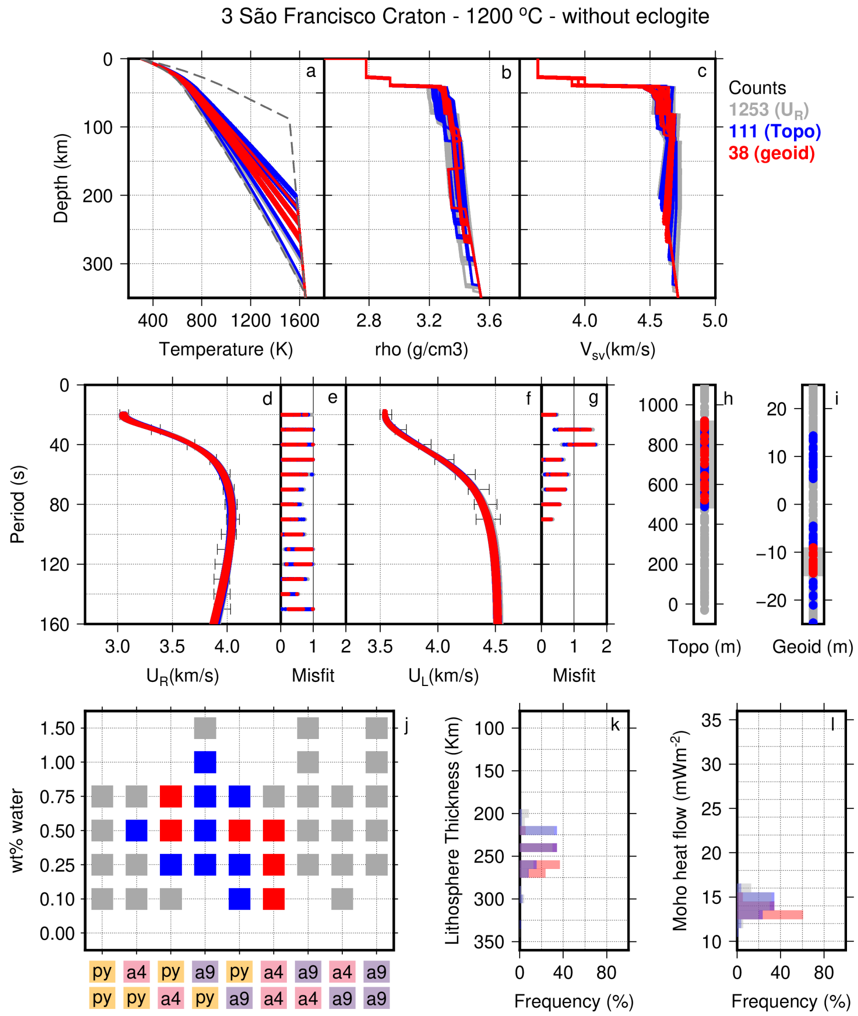

Figure 6. Example of solutions from the grid-search process: a set of solutions for group 3SFC for a sublithospheric potential temperature of 1200°C without an eclogitic layer. All solutions that fit the dispersion curves are in grey; those that fit both the dispersion curves and the elevation are in blue; those that fit dispersion curves, elevation, and geoid are in red. Top row: (a) Geotherms, with the coldest and hottest geotherms tested indicated by grey dashed lines, (b) density profiles, and (c) V_{SV} profiles. Middle row: (d) Rayleigh-wave group velocities vs period and (e) respective misfits, (f) Love-wave group velocities vs period and (g) respective misfits, (h) and (i) show elevation and geoid, respectively, with a dark grey box for the observed range. Bottom row: (j) water content vs background composition (top layer/bottom layer), (k) and (l) show histograms of the solutions for thermal lithosphere thickness, and Moho heat flow.

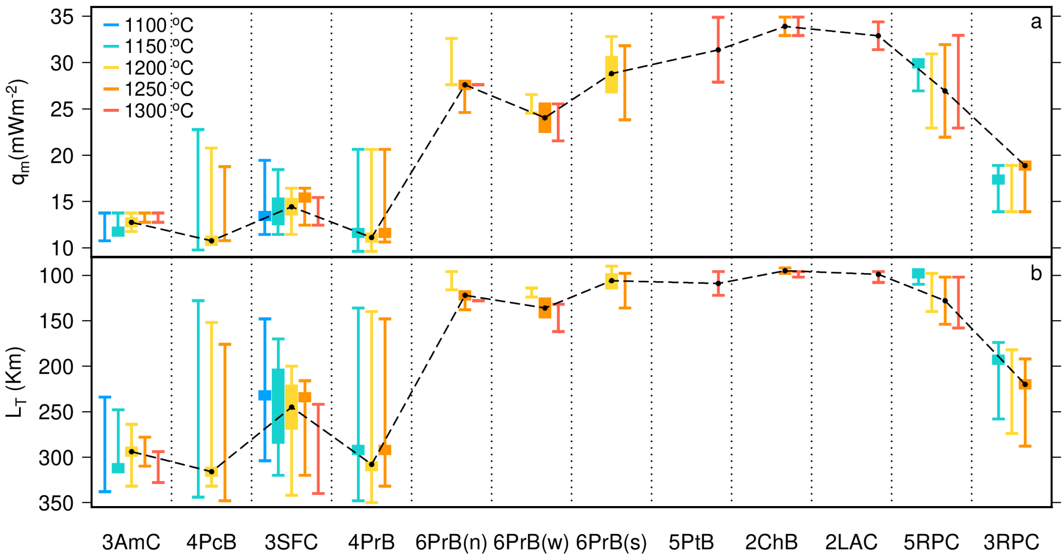

Figure 7. Summary of the range of solutions for Moho heat flow (a) and thermal lithosphere thickness (b) for all of the tested sublithospheric potential temperatures (different colors). The range of solutions that fit the the dispersion curves alone are shown as a line, and the range of solutions that also fit topography and geoid are show as a bar. While some regions require a specific potential temperature to fit the observations, other regions have solutions for multiple sublithospheric temperatures tested. The final preferred set of solutions are indicated by the black dashed line and respective black dots that correspond to the best fit solution of those sets.

Based on the thermal and compositional models that we find for each region for the chosen mantle potential temperature, it is possible to divide the area of study into 4 major types of lithospheric structure: (1) thick lithosphere with minor shallow alteration and sometimes an eclogitic layer, (2) thick lithosphere with alteration over a larger depth range, (3) thin lithosphere with an eclogitic layer, and (4) thin lithosphere affected by dynamic topography. The solutions for the regions are discussed according to these classes below.

3.2 Thick lithosphere with some shallow alteration and sometimes an eclogitic Layer

This type of structure is found below the three cratonic regions in the study area (Figure 8). The lithosphere below the Amazon (3AmC) and São Francisco (3SFC) cratons is found to be thick (between 220 and 294 km thick), and cold (Moho heat flow between 13 and 15 mWm^{-2}). The easternmost part of the Rio de la Plata Craton (3RPC) is almost as thick as the two northern cratons (220 km thick), and has a slightly higher Moho heat flow (19 mWm^{-2}).

The dispersion curves for groups 3AmC and 3SFC can only be fit with some amount of water at shallower depths. For solutions that fit both elevation and geoid height, the water content is 0.5 wt% for the Amazon Craton and from 0.1 to 0.75 wt% for the São Francisco Craton. Both regions require a somewhat fertile composition on the top lithospheric layer (ARC4 or pyrolite) over a more depleted and lower density composition in the bottom layer (ARC4 or ARC9), with an interface at 80, 120 or 160 km depth. Although the southern Amazonian and the São Francisco cratons do not require an eclogitic layer to fit the observables, we do also find acceptable solutions with the presence of an

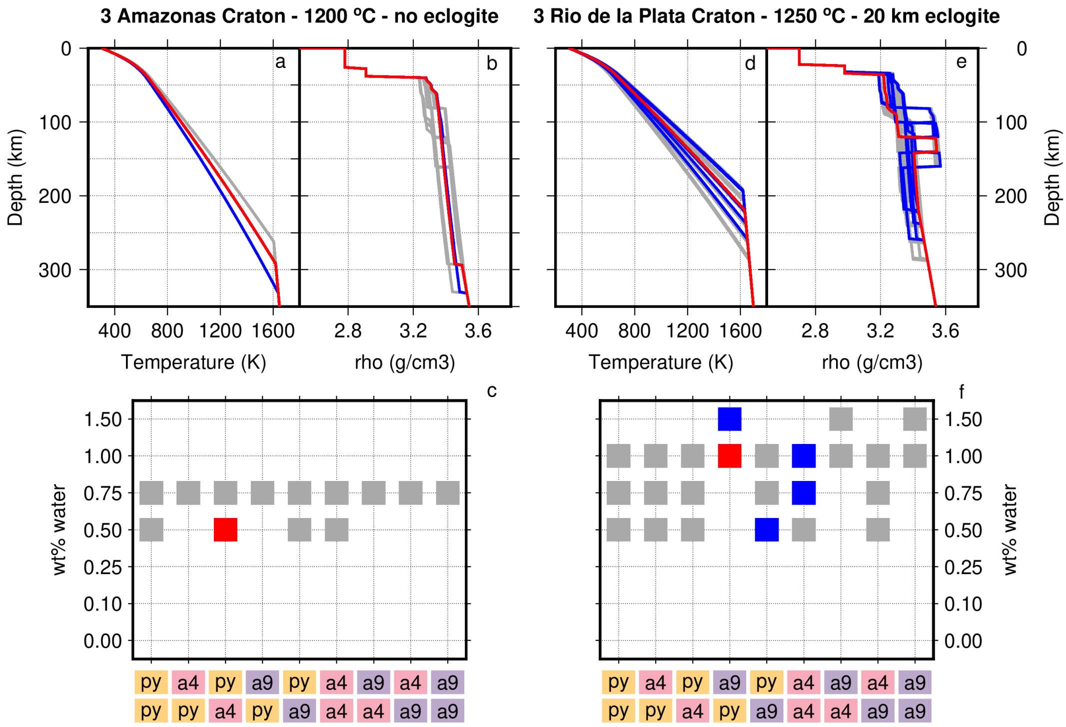

Figure 8. Summary of the results for cratonic groups 3AmC on the left, and 3RPC on the right. The panels are: (a and d) Geotherms, (b and e) density profiles, and (c and f) water content vs background composition (top layer/bottom layer). All solutions that fit the dispersion curves are in grey, those that fit both the dispersion curves and the elevation in blue, and those that fit dispersion curves, elevation, and geoid in red.

eclogitic layer (Figs. S4 and S6). In those cases, the solutions that fit the geoid require a more depleted composition (ACR4) in the top layer to compensate for the high-density eclogite layer.

Region 3RPC requires high amounts of metasomatism below the Moho, with more than 1.0 wt% water. Differently from the other cratons, it requires a thick layer of high-density eclogite at mid-lithospheric depths (20 km thick layer at 120 km depth) to fit the geoid height. In terms of background composition, this is the only region to have a preference for a more depleted composition in the top layer (ARC9).

3.3 Thick Lithosphere with more Pervasive Alteration

The Parecis Basin (4PcB) and the eastern Paraná Basin (4PrC) regions, which border the two northern cratons, are seismically slower than the cratons but have a similarly low geoid height. The slower velocities can be achieved by higher Moho heat flow and thinner lithosphere, but this would raise the geoid height. By instead keeping Moho heat flow low and adding metasomatism deeper in the lithosphere, both the velocities and geoid are kept low. The resulting thermal structures for those regions comprise a thick lithosphere (between 270 and 316 km thick) with low Moho heat flow (between 11 and 15 mWm^{-2}). For these two regions, we expanded our grid search to include variations in lithospheric mantle heat production between none or 0.01 μWm^3 in order to achieve more variation in thermal lithosphere thickness at greater depths.

Therefore, although similar in thermal structure to the cratonic regions, these regions require metasomatism to extend to larger depths (Figure 9). In our models, we divide the lithosphere into two layers and allow the amount of phlogopite in each layer to vary independently (at 80, 120, 160, 200, and 240 km depth). Our results show that region 4PrB requires significant amounts of alteration throughout the lithosphere (between 1.0 to 5.0 wt% Phl with an interface at 240 km depth), while region 4PcB requires higher amounts within the top layer (7.5 wt% Phl with interface at 200 km depth) and no alteration at the bottom. In terms of background composition, both regions require pyrolite on top of a less dense composition (ARC4 or ARC9).

3.4 Thin Lithosphere with an Eclogitic Layer

The regions covered by the western Paraná basin (groups 6PrB) have a peculiar structure. The regions seem to have a somewhat thinner (between 98 and 146 km thick) and warmer lithosphere (q_M between 23 and 33 mWm^{-2}). The northern regions require significant amounts of metasomatism to match the slow velocities at short periods: group 6PrB(n) requires amounts higher than 2.0 wt% water and 6PrB(w), higher than 0.5 wt%. In contrast, the southern region 6PrB(s) has solutions for all water amounts tested, which means that we are not able to resolve the amount of metasomatism needed for this region. Although these regions need a warm lithosphere to fit the surface wave dispersion data, they also require a dense lithosphere to fit the high geoid and low elevation. A fertile peridotitic composition is not dense enough, so we added an basaltic composition layer at the top of the mantle lithosphere (a 10 or 20 km tick layer starting at 50, 60, or 70 km depth). In summary, the structures that fit the data of these regions are: a thin lithosphere with some metasomatism below the Moho, and an high-density layer somewhere between 50 and 90 km depth underlain by a fertile composition (Figure 9).

3.5 Thin Lithosphere Being Affected by Dynamic Topography

For regions 2LAC, 5PtB, and 2ChB, 5RPC, and 2LAC there are no solutions that fit both elevation and geoid height. These regions require an overall high-density material by either colder temperatures or some composition denser than pyrolite. However, the dispersion curves require high mantle potential temperature and thinner lithosphere (between 92 and 122 km thick, and 28 and 35 mWm^{-2}), and even the addition of an eclogite layer is not enough to fit the geophysical observation. Therefore, we propose that those regions are being affected by sublithospheric mantle flow, e.g. associated with Andean subduction for the western 5PtB and 2ChB regions.

4 Discussion

4.1 Love-waves

The results show that for the majority of the regions our solutions have a similar shape to the Love-wave group-velocity-period curves, although they may not fit completely within the estimated uncertainties (Supplementary Figures S3 to S16). Our solutions for regions 2ChB, 4PrB and 5PtB are too slow at short periods (30 to 60 seconds). To fit the data, they would probably require stronger radial anisotropy on the top of the lithosphere, which could trade off with less metasomatic alteration of the shallow lithosphere to maintain the fit of the Rayleigh-wave dispersion curves. Models with strong radial anisotropy (5% below the Moho) require up to 0.5 wt% less water, for cases with added water only, and up to 50% less phlogopite, for cases with added water and K_2O, compared to cases with zero radial anisotropy (Eeken et al., 2018). Regions in the south (5RPC and 3RPC) have Love-wave group velocities that almost decrease constantly with depth at longer periods (60 to 90 seconds), which can not be fit with any physical model. The comparison between the Love-wave synthetics and the data indicates that the South American

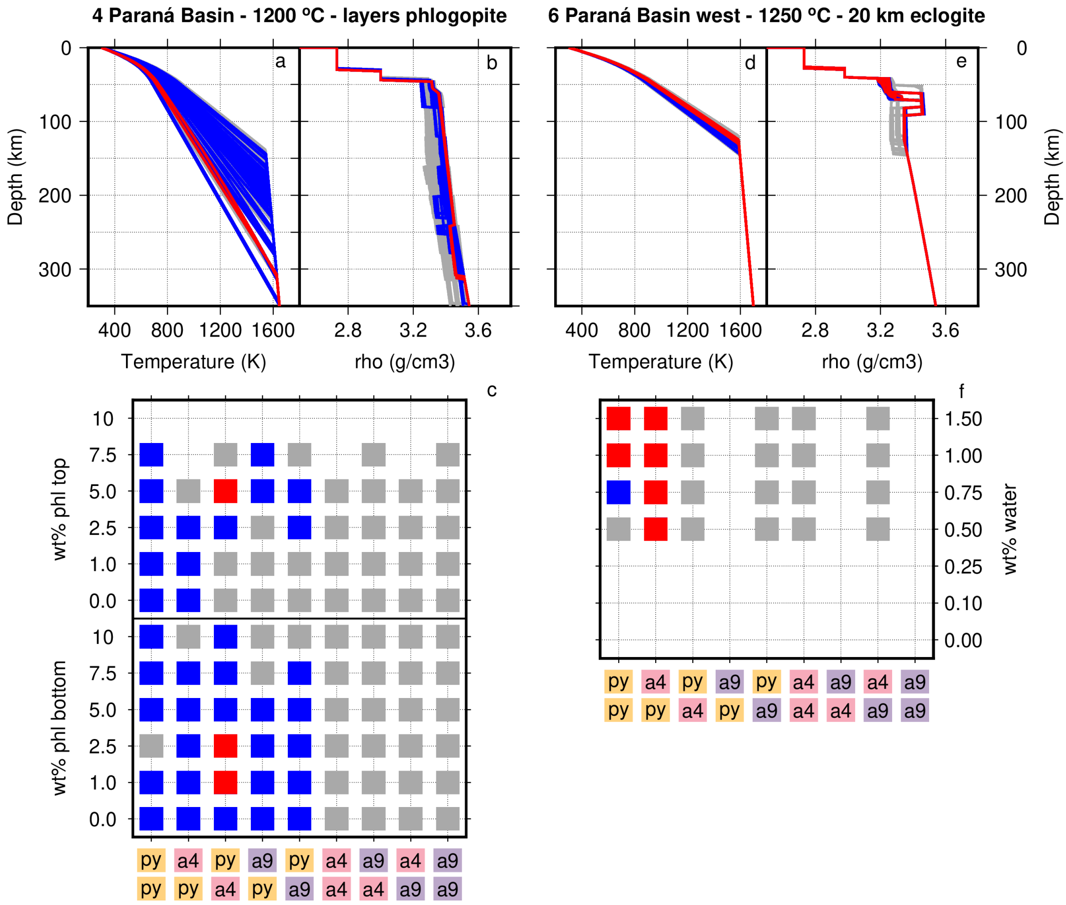

Figure 9. Summary of the results for groups 4PrB on the left, and 6PrBw on the right. The panels are: (a and d) Geotherms, (b and e) density profiles, and (c and f) water content vs background composition (top layer/bottom layer). All solutions that fit the dispersion curves are in grey, those that fit both the dispersion curves and the elevation in blue, and those that fit dispersion curves, elevation, and geoid in red.

Platform probably requires some variation in radial anisotropy. However, even with such variations, the fits to the Love waves are close enough that some shallow lithosphere metasomatism remains required for most regions. A joint Rayleigh-Love phase (rather than group) velocity study could probably better resolve such variations in radial anisotropy.

4.2 Uncertainties and Trade-offs

The method involves a range of uncertainties. Besides the choice of radial anisotropy model, the main uncertainties are related to the thermodynamic methods and data and the chosen attenuation model, and the extracted dispersion curves. The uncertainties of the thermodynamic conversion have been previously discussed in our previous studies employing the same method (Altoe et al., 2020; Eeken et al., 2020). The uncertainty in mapping an absolute velocity to temperature results in an about 100°C uncertainty in temperature. This is a systematic uncertainty, and the uncertainties in temperature differences are estimated to be < 50°C. Similarly, the systematics between velocities for different compositions are robust, but, in particular for compositions outside of the dunite-pyrolite array, the mapping of an exact water content or eclogite composition from seismic and density data is uncertain. The anelasticity model affects predicted velocity-depth gradients, i.e. there is some trade-off between the temperature-dependence of anelasticity and the amount of shallow lithosphere alteration required, but we found alteration is usually required in spite of these uncertainties.

The main difference between this study and the one conducted in North America is the size of the error bars for the dispersion curves. In addition to the already larger standard deviation calculated for each period of the dispersion data, we had to increase the error bars for periods longer than 60 seconds due to large jumps in velocity between neighbouring periods. To alleviate the less strong constraints due to the larger uncertainties in the dispersion data, we included in the analysis data of elevation and geoid height. The added data helped to better constrain variations in composition and its depth distribution. However, for regions significantly affected by dynamic topography, the elevation and geoid calculations are not applicable and aside from a thickness, the lithospheric structure remains poorly constrained.

We require partially melt- and hence iron-depleted background lithosphere below most of the region consistent with xenoliths and xenocrysts (O'Reilly & Griffin, 2010; Griffin et al., 2009) and previous studies that modelled cratonic elevation, gravity and/or geoid (e.g., Jordan, 1978; Afonso et al., 2008; Finger et al., 2021). However, contrary to what has been assumed in many previous studies, below most regions, including AmC and SFC, 4PcB, 4PrB, we need deep lithosphere to be more depleted than the shallow parts. Only RPC solutions are more depleted on top. Regions 6 require the thin lithosphere to be fertile throughout. Xenolith data actually allow a range of different types of layering, with the top of the lithosphere either more or less depleted than deeper lithosphere (e.g., O'Reilly & Griffin, 2010). The layering of depletion we find below most of the South American platform may be more consistent with lithospheric stacking to form cratonic roots than formation above a plume, or with underplating of buoyant refractory lithosphere during hotter subduction conditions in the early Earth (Perchuk et al., 2020).

In our solutions, the net effect of alteration and melt-depletion on density is that the top of lithosphere is lower in density than the base, as previous studies of density sensitive data (gravity, geoid) have usually required (e.g., Afonso et al., 2008). Previous studies have invoked more melt-depletion of the shallow lithosphere to make it low density. However, this melt-depletion leads to higher shallow lithosphere velocities increasing the misfit to the dispersion data. Another way to lower shallow lithosphere velocities would be increased radial anisotropy, but there are few locations where this appears required by the Love waves (see above). By contrast, metasomatism lowers density and ensures the top of mantle lithosphere is not too fast. This larger variation in lithospheric composition does then also lead to solutions with different vertical gradients of depletion of the background composition.

4.3 Structure and tectonics

Emerging from this work and a few previous studies (Altoe et al., 2020; Eeken et al., 2020; Liddell et al., 2018; Boyce et al., 2019; Eakin, 2021; Gilligan et al., 2016) is the conclusion that the lithospheric mantle below the continental platform holds more of a record of its previous tectonic history than often assumed. The seismic data we use have more lateral resolution than the most recent thermo-compositional analyses by Finger et al. (2021) and with the combination of dispersion curves and geoid we are able to better evaluate the variation in composition with depth. In addition, we consider and require a larger range of compositions then only variable iron-depletion of a peridotitic mantle lithosphere. In most of the South American Platform, the lithosphere needs to be refractory to fit elevation and geoid, as previous studies have found. However, we also need low-velocity material in parts of the lithospere, with alteration as the most likely cause, and additional high-density material.

Combining the results of thermal and compositional variation in the region, we can distinguish different classes of lithospheric structure (Figure 10): cratonic cores that have preserved their Proterozoic roots, regions of intracontinental Paleozoic basins where plume interaction has altered the lithosphere, regions of intracontinental Paleozoic basins that were possibly protected by a thick root until lithosphere thinning in the Phanerozoic and are underlain by high density material, and regions being affected by dynamic topography.

4.3.1 Cratons with Archean cores

Groups 3AmC and 3RPC comprise mostly of regions of accreted Archean/ Paleoproterozoic terrains, while 3SFC also includes the Neoproterozoic orogenic belts on its margins. The structure below the three cratons is seismically the most distinct within the platform. Thick thermal roots were found before below the Amazonian and São Francisco Cratons (van der Lee et al., 2001; Heintz et al., 2005; Finger et al., 2021; Feng et al., 2004). Our study only covers the southeastern part of the Amazon Craton and we find that its lithospheric structure is similar to that below the São Francisco Craton even of their tectonic/geologic histories have been proposed to differ (Brito Neves & Fuck, 2014). With the improved resolution in the southern platform (Rosa et al., 2016), we find a thick cratonic root below the southeastern part of the Rio de la Plata Craton which was not identified before.

The structures found below 3AmC and 3SFC most resemble those we previously found under eastern North America in regions of Proterozoic collision, where we attributed the metasomatic modification of the shallow mantle lithosphere to arc accretion along the eastern margin of Laurentia (Altoe et al., 2020; Eeken et al., 2020). A thick lithosphere with a high-velocity mid-lithospheric layer plus shallow lithosphere metasomatism as we find under region 3RPC, was found in parts of the Superior Craton characterised by Archean/Paleoproterozoic collision (Altoe et al., 2020; Eeken et al., 2020). Thus, the South American cratons resemble the North American regions both in thickness and compositional structure, although at least within our study region, we do not find any evidence of a cold, thick unaltered core as we found below the northern and western Superior Province.

The interpretation that the dominant signature in the lithosphere of these cratonic blocks is that of the Proterozoic collision phase is consistent with their tectonic history. The southern Amazonian Craton is composed mainly of two east-west continental mag-

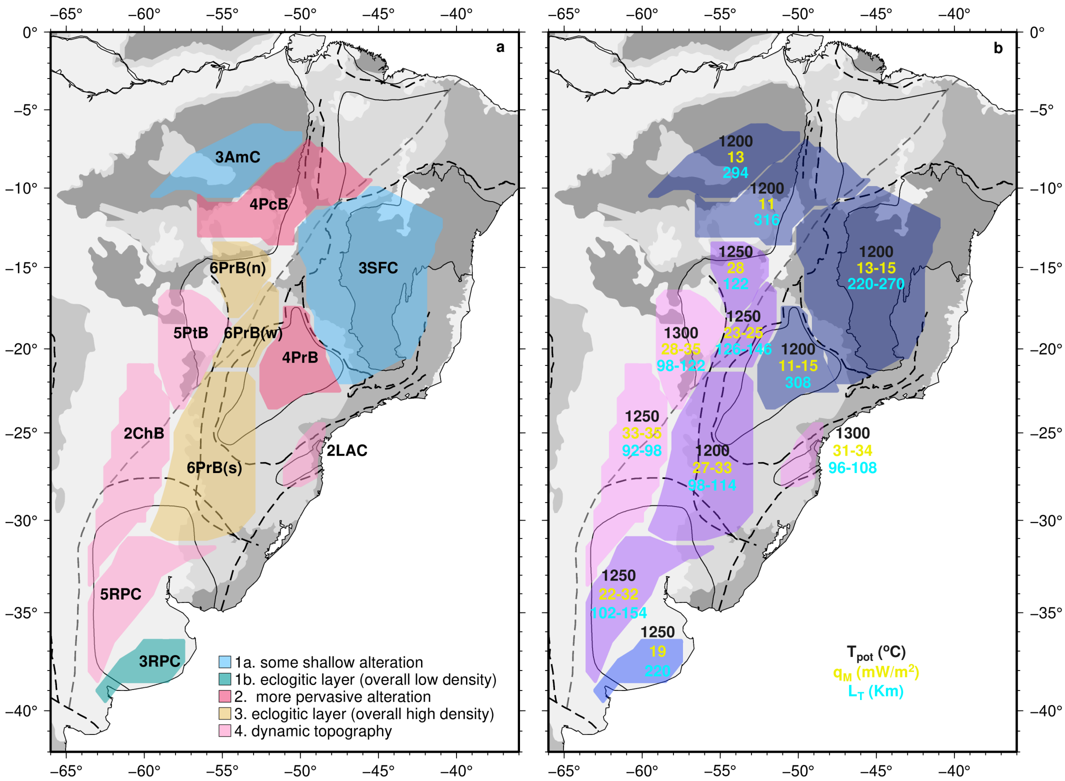

Figure 10. Summary map of the compositional (a) and thermal (b) variation across the study region inferred from our results. Combining these results, we can distinguish four different classes of lithospheric structure. (1) Groups in the Amazonian (3AmC), São Francisco (3SFC), and Rio de la Plata cratons (3RPC) can be matched with a thick lithosphere, some shallow alteration, and sometimes a layer of eclogite. These regions are cratonic cores that seem to have preserved their Proterozoic roots. (2) Groups in the Parecis (4PcB) and eastern Paraná (4PrB) basins are characterised by a thick lithosphere and require more pervasive metasomatism, most likely due to Mesozoic plume interaction. (3) Groups in the Paraná basin below the Western Paraná Suture Zone require a thin lithosphere and a shallow layer of eclogite. These regions were possibly protected by a thick root until lithosphere thinning in the Phanerozoic. (4) regions above the Pantanal (5PtB), and Chaco (2ChB, 5RPC) basins, and below the Luíz Alves Craton in the east coast require thin lithosphere and seem to be affected by dynamic topography.

matic arcs that evolved between 2.0 and 1.87 Ga at the margin of an Archean-Paleoproterozoic continent. During the convergence period there was a possible flat subduction stage, which may explain the metallogenetic zoning observed in the southern Amazonian craton (e.g., Fernandes et al., 2011; Bettencourt et al., 2016), and could have left a remnant eclogite layer in the lithosphere. No overprint of younger recent events are described in this region, suggesting that during the Neoproterozoic this region was already cratonized and has been stable since then.

The basement of the São Francisco Craton is comprised of Archean blocks that were extensively affected by Paleoproterozoic orogenic episodes (2.3 - 1.9 Ga) (e.g., Teixeira & Figueiredo, 1991). During the Neoproterozoic, the region went through a convergent phase, which culminated with the development of the Brasiliano orogenic belts on the margins of the São Francisco-Congo Craton (Almeida et al., 2000). In the Upper Cretaceous, during the Gondwana break-up, magmatism occurred but was restricted to the border with the Paraná Basin (e.g. Hackspacher et al., 2007; da Silva et al., 2008; Carvalho et al., 2022). Hence, we propose that the metasomatism observed in the shallow São Francisco lithosphere could be due to its Paleoproterozoic assembly with a possible further contribution from Neoproterozoic orogenic belts on the craton margins.

Most of the Rio de la Plata Craton is covered by Phanerozoic sediments of the Chaco-Paraná basin, but data from exposed belts in the east and boreholes in the west reveal a similar basement, formed during the Palaeoproterozoic in an island-arc environment (Rapela et al., 2007; Oyhantçabal et al., 2010). While the western portion of the craton lies below an intracratonic basin and appears to have lost much of its root, the eastern portion seems to have preserved its original Paleoproterozoic lithosphere. The presence of an eclogitic layer below the eastern-southern part of the Rio de la Plata craton could be interpreted as a relict of subducted oceanic crust from the Paleoproterozoic events that assembled the block and got preserved in the lithosphere. A similar collisional structure has been observed in several other cratonic regions (Bostock, 1998; Altoe et al., 2020; Hopper & Fischer, 2015), and may be a feature of subduction involving relatively warm buoyant plates as formed in the early Earth.

4.3.2 Proterozoic Blocks and Intracratonic Basins

Much of the rest of the South American platform is characterised by Paleozoic intracratonic basins. Most of these basins (Parecis, Paraná, Chaco-Paraná, Parnaíba, Amazonas, Solimões) are thought to be underlain by Proterozoic basement, assembled into its current configuration during the Neoproterozoic Brasiliano Orogeny. The main underlying mechanism for the formation of these basins by slow and prolonged subsidence during the Paleozoic is most likely thermal subsidence (Julià et al., 2008; Milani & Ramos, 1998) in response to low-rate extension and requires the presence of thick lithosphere (Allen & Armitage, 2012). Other mechanisms, including flexure due to glacial loading (Zalán et al., 1990), Panthallassan subduction (Milani & Ramos, 1998), or a dynamic response to flushing of slab material through the 660-km discontinuity (Pysklywec & Quintas, 2000) have been proposed to have contributed to the evolution and individualisation of the different basins.

Below the Parecis and Paraná Basins, thick lithosphere is still present today, although it appears to be pervasively altered throughout much of its depth range. Chronostratigraphic correlations between the Paraná and Parecis Basins have been established, indicating similar periods of subsidence (Silurian/Devonian and Permian/Carboniferous), and possibly, similar underlying processes (e.g., Pedreira & Bahia, 2004). During the Mesozoic, these basins were affected by substantial magmatism followed by Jurrassic/Early Cretaceous subsidence (Zalán et al., 1990; Milani, 2004). Within the Parecis Basin, the volcanic rocks of Anari and Tapirapuã Formations (196 to 206 Ma, Barros et al., 2006; Marzoli et al., 1999) are linked to plume activity related to Central Atlantic opening.

Two intraplate magmatic events have been recognised in the Paraná Basin, the Paleozoic Três Lagoas basalts (443 ± 10 Ma) and the Mesozoic Serra Geral Formation flood basalts (137 to 127 Ma) that form the LIP linked to South Atlantic opening.

The extensive Mesozoic volcanism indicates that the lithosphere was likely significantly thinned below both the northern Paraná and Parecis basins, probably by plume impingement. Alternatively, magmas produced below thinner lithosphere neighbouring these basins would have had to accumulate within these basins through deflection during upward migration or flow towards the basins upon extrusion. Our analysis indicates that, if previously thinned, the lithosphere below these two regions has since healed and thickened again. The deep metasomatism could be related to the infiltration of plume-related magmatic fluids into the cratonic keel (C.-T. Lee & Rudnick, 1999). Plume upwelling may not only be responsible for lithospheric removal (Wang et al., 2015) but for its recratonization. Numerical modelling shows that the depleted melt residues produced by plumes accumulate in regions of thinned lithosphere located between thick cratonic regions, whether the upwelling is directly beneath the thinned region or displaced laterally from it (Liu et al., 2021). A similar kind of compositional structure combined with the presence of thick lithosphere is observed in the Mid-Continent Rift System in North America (Altoe et al., 2020).

The western and southern parts of the Paraná basin (6PrB(n), 6PrB(w), and 6PrB(s)) are underlain by a relatively thin ($\sim$ 100 km) present-day lithosphere. As mentioned before, these regions coincide with a geophysically identified suture zone (Dragone et al., 2017, 2021; Bologna et al., 2019). The Western Paraná Suture/Shear Zone (WPSZ) follows a gravity gradient between negative Bouguer anomalies in the east, and positive Bouguer anomalies in the west, it also coincides with changes in crustal thickness, lithospheric velocities, and electrical resistivity (Dragone et al., 2017). Magnetotelluric surveys conducted in what is our region 6PrB(s) imaged a high-resistivity anomaly under the edge of the Paraná Basin. This eastward dipping anomaly starts in the crust and extends to upper mantle depths (70-100 km depth), and was interpreted as a remnant of a former subduction zone beneath the Paraná Basin related to the amalgamation between the Rio de la Plata and the Southern Paraná cratons during the Brasiliano events.

The eclogitic layer below regions 6PrB can be interpreted as a remnant of a formal subduction zone (e.g., Hajnal et al., 1997), but could also be the result of metamorphic eclogitization of the lower crust during lithosphere shortening (e.g., Bousquet et al., 1997). In both cases, this layer would be a remnant of the Brasiliano orogenic events. Another possibility is that the layer is the residue of partial melting during ancient magmatic events (e.g., C. T. A. Lee et al., 2006; C.-T. A. Lee et al., 2011), e.g. during Mesozoic extension. The fact that this structure has been preserved suggests that the layer is trapped in a part of the lithospheric root that is highly viscous, preventing the high-density layer from sinking. The lithosphere below these region was probably originally thickened by stacking and/or shortening during oceanic or continental collision events, and likely was still thick during the Paleozoic intracratonic Paraná Basin subsidence phases. During Mesozoic extension and plume activity, these regions experienced events that may have thinned their lithospheric roots. However, differently from the northern Paraná Basin, the conditions were apparently not favourable for recratonization, maybe because of the larger distance from the northern cratonic blocks.

In contrast to several previous studies (Feng et al., 2004, 2007; Finger et al., 2021), we do not find any structures clearly following the Transbrasiliano Lineament (TBL). As other tomographic studies found, the velocities along much of the TBL are low compared to, in the south, regions to the east, and in the north, the regions east and west of it. However, our results emphasise that the structure varies at least as much from north to south along the TBL as across it. In contrast to the Paraná Suture zone, which appears to coincide with the western boundary of regions 6PrB, the TBL crosscuts several of our clusters, so the TBl does not appear to have a clear lithospheric expression.

4.3.3 Modified Cratons and the Effects of Dynamic Topography

Groups on the western margin (5PtB, 2ChB, and 5RPC) and 2LAC on the eastern margin contain small fragments of Archean cratonic crust. The western regions include the Rio Apa, the Rio Tebicuary and part of the Rio de la Plata cratons, respectively, and region 2LAC on the east coast contains the Luíz Alves Craton. Although they acted as stable cratonic blocks during Neoproterozoic events, these regions currently lack lithospheric roots. Therefore, those regions can be classified as 'modified cratons' (Pearson et al., 2021). Lithospheric thinning could be due to the same Mesozoic plume activity and stretching that probably led to the modification and thinning of the lithosphere below the Paraná Basin. However, there is limited evidence of Mesozoic magmatism in the western platform. Other examples of modified cratons include the North China and Wyoming Cratons, where root destabilisation has often been attributed to weakening of the lithosphere by fluids released by subducted lithosphere (Dave & Li, 2016; Gao et al., 2004). Proximity to the Andean subduction zone, with a history of flat subduction (e.g., Ramos & Folguera, 2009) which might have delivered fluids quite far into the foreland, makes this a plausible contributing mechanism for root erosion below the western margin of the South American Platform as well.

Besides the thin lithosphere, these regions also seem to be affected by dynamic topography. Tomographic models (e.g., Portner et al., 2020; Rodríguez et al., 2021; Li et al., 2008; Ren et al., 2007) show that the Nazca slab below the central part of South America between 65°W and 55°W is particularly pronounced and it thickens upon penetration through 660 km depth. Within this region, the Andean Foreland Basins system developed, including the Pantanal and Chaco basins. The downward flow associated with the sinking slab induces subsidence of the overlying lithosphere (Flament et al., 2015), which could explain the present-day topographic low observed in those regions. Therefore, the western margin (5PtB, 2ChB, and 5RPC) seem to be affected by dynamic topography due to subduction of the Nazca plate.

Different tomographic models also resolve multiple high-velocity anomalies in the sub-lithospheric mantle below the South Atlantic margins of South America. These anomalies have been interpreted as zones of downwelling due to delamination or dripping of the edge of the continental lithosphere (King & Ritsema, 2000; Hu et al., 2018). Such lithospheric removal can result in isostatic uplift, which would explain the present topographic high in region 2LAC, while the density anomalies associated with lithospheric fragments in the mantle might explain the low geoid.

5 Conclusions

Variations in Rayleigh-wave group velocities, topography and geoid across the eastern South American Platform can be modelled with four distinct types of thermo-chemical mantle lithosphere, which seem to correlate with different events in the tectonic history of the South American Platform. The South American Platform appears to have lost at least part of the (> 200 km) thick lithospheric roots that probably existed when it stabilised at the end of the Neoproterozoic assembly of Western Gondwana. Thick thermal lithosphere (200-300 km) remains below the largest Archean cratonic blocks (Amazonian, São Francisco, and southern Rio de la Plata cratons). The presence of shallow lithospheric metasomatic alteration and, in some places, a layer of eclogite within these three cratonic roots are probably a signature of their assembly by collision during the Archean to Neoproterozoic.

The Paleozoic Parecis and northern Paraná intracratonic basins adjoining the two large northern Archean cores, are also underlain by thick lithosphere (200-300 km), but require more pervasive metasomatism. These regions were likely affected by plume activity, which can lead to infiltration of magmatic fluids into the cratonic keel. Plume upwelling may have caused lithospheric erosion in those regions (allowing the extensive Mesozoic magmatism) but would then probably have aided its recratonization.

By contrast, other intracratonic basins (western and southern Paraná, Pantanal, Chaco basins), which have Paleoproterozoic basements with small Archean fragments, only retain a $\sim$ 100 km thick lithosphere. The western and southern parts of the Paraná Basin, overlying the Western Paraná Suture Zone, require a shallow layer of eclogite (probably stabilised in high-viscosity lithosphere), which may be a remnant of Neoproterozoic subduction. For the regions along the western and eastern edge of the South American platform, topography and geoid cannot be matched with an isostatic model and are likely affected by dynamic topography due to Andean subduction in the west and edge-driven convection along the passive margin in the east.

Our results suggest more compositional heterogeneity in cratons than usually considered, and more lithospheric root modification and erosion than below for example North American cratonic regions, possibly resulting from the small size of many of the South American Archean cores, and the strong and recent influence of both plume activity (including the Paraná-Etendeka LIP) and subduction (along the Andean margin).

Open Research

The regionalisation and main characteristics of the thermo-chemical models are included as Supporting Information. Conversion was done using the open source code PerPleX which can be found on www.perplex.ethz.ch, including the thermodynamic data base used. The Abers and Hacker (2016) data base is also freely available at doi.org/10.1002/2015GC006171. Topography and geoid data were retrieved from www.ngdc.noaa.gov/mgg/global/global.html and icgem.gfz-potsdam.de, respectively.

Acknowledgments

We thank María L. Rosa for sharing the tomographic model of South America used in this study. Isabella L. Altoe was funded by a scholarship from the CAPES Foundation, agency under the Ministry of Education, Brazil (DOC_PLENO - 88881.128245/2016-01).

References

Abbott, D. (1991, 4). The case for accretion of the tectosphere by buoyant subduction. *Geophysical Research Letters*, *18*(4), 585–588. doi: 10.1029/91GL00813

Abers, G. A., & Hacker, B. R. (2016, 2). A MATLAB toolbox and ¡scp¿E¡/scp¿ xcel workbook for calculating the densities, seismic wave speeds, and major element composition of minerals and rocks at pressure and temperature. *Geochemistry, Geophysics, Geosystems*, *17*(2), 616–624. doi: 10.1002/2015GC006171

Abt, D. L., Fischer, K. M., French, S. W., Ford, H. A., Yuan, H., & Romanowicz, B. (2010, 9). North American lithospheric discontinuity structure imaged by Ps and Sp receiver functions. *Journal of Geophysical Research: Solid Earth*, *115*(9), B09301. doi: 10.1029/2009JB006914

Affonso, G. M. P. C., Rocha, M. P., Costa, I. S. L., Assumpção, M., Fuck, R. A., Albuquerque, D. F., … Beck, S. L. (2021, 4). Lithospheric Architecture of the Paranapanema Block and Adjacent Nuclei Using Multiple-Frequency P-Wave Seismic Tomography. *Journal of Geophysical Research: Solid Earth*, *126*(4), e2020JB021183. doi: 10.1029/2020JB021183

Afonso, J. C., Fernàndez, M., Ranalli, G., Griffin, W. L., & Connolly, J. A. D. (2008, 5). Integrated geophysical-petrological modeling of the lithosphere and sublithospheric upper mantle: Methodology and applications. *Geochemistry,* *Geophysics, Geosystems*, *9*(5), n/a-n/a. doi: 10.1029/2007GC001834

Afonso, J. C., Salajegheh, F., Szwillus, W., Ebbing, J., & Gaina, C. (2019, 6). A global reference model of the lithosphere and upper mantle from joint inversion and analysis of multiple data sets. *Geophysical Journal International*, *217*(3), 1602–1628. doi: 10.1093/gji/ggz094

Albuquerque, D. F., França, G. S., Moreira, L. P., Assumpção, M., Bianchi, M., Barros, L. V., ... Oliveira, M. E. (2017). Crustal structure of the Amazonian Craton and adjacent provinces in Brazil. *Journal of South American Earth Sciences*, *79*. doi: 10.1016/j.jsames.2017.08.019

Allen, P. A., & Armitage, J. J. (2012, 1). Cratonic Basins. *Tectonics of Sedimentary Basins: Recent Advances*, 602–620. doi: 10.1002/9781444347166.CH30

Almeida, F. F. M. d., Brito Neves, B. B. d., & Dal Ré Carneiro, C. (2000, 5). The origin and evolution of the South American Platform. *Earth-Science Reviews*, *50*(1-2), 77–111. doi: 10.1016/S0012-8252(99)00072-0

Altoe, I., Eeken, T., Goes, S., Foster, A., & Darbyshire, F. (2020, 10). Thermo-compositional structure of the north-eastern Canadian Shield from Rayleigh wave dispersion analysis as a record of its tectonic history. *Earth and Planetary Science Letters*, *547*, 116465. doi: 10.1016/j.epsl.2020.116465

Amante, C., & Eakins, B. (2009). ETOPO1 1 Arc-Minute Global Relief Model: Procedures, Data Sources and Analysis. *NOAA Technical Memorandum NESDIS NGDC-24*(March). doi: 10.1594/PANGAEA.769615

Assumpção, M., Feng, M., Tassara, A., & Julià, J. (2013). *Models of crustal thickness for South America from seismic refraction, receiver functions and surface wave tomography.* doi: 10.1016/j.tecto.2012.11.014

Barros, M. A. d. S., Mizusaki, A. M., Weska, R., de Borba, A., Chemale Jr, F., & da Costa, E. C. (2006, 6). Petrografia, Geoquímica, Análises Isotópicas (Sr, Nd) e Geocronologia Ar-Ar dos Basaltos de Tapirapuã (Tangará da Serra, Mato Grosso, Brasil). *Pesquisas em Geociências*, *33*(2), 71. doi: 10.22456/1807-9806.19515

Berrocal, J., Marangoni, Y., de Sá, N. C., Fuck, R., Soares, J. E., Dantas, E., ... Fernandes, C. (2004, 9). Deep seismic refraction and gravity crustal model and tectonic deformation in Tocantins Province, Central Brazil. *Tectonophysics*, *388*(1-4), 187–199. doi: 10.1016/J.TECTO.2004.04.033

Bettencourt, J. S., Juliani, C., Xavier, R. P., Monteiro, L. V., Bastos Neto, A. C., Klein, E. L., ... Pereira, V. P. (2016, 7). Metallogenetic systems associated with granitoid magmatism in the Amazonian Craton: An overview of the present level of understanding and exploration significance. *Journal of South American Earth Sciences*, *68*, 22–49. doi: 10.1016/J.JSAMES.2015.11.014

Bologna, M. S., Dragone, G. N., Muzio, R., Peel, E., Nuñez-Demarco, P., & Ussami, N. (2019, 1). Electrical Structure of the Lithosphere From Rio de la Plata Craton to Paraná Basin: Amalgamation of Cratonic and Refertilized Lithospheres in SW Gondwanaland. *Tectonics*, *38*(1), 77–94. doi: 10.1029/2018TC005148

Bostock, M. G. (1998). Mantle stratigraphy and evolution of the Slave province. *Journal of Geophysical Research: Solid Earth*, *103*(B9), 21183–21200. doi: 10.1029/98jb01069

Bousquet, R., Goffé, B., Henry, P., Le Pichon, X., & Chopin, C. (1997). Kinematic, thermal and petrological model of the Central Alps: Lepontine metamorphism in the upper crust and eclogitisation of the lower crust. *Tectonophysics*, *273*(1-2). doi: 10.1016/S0040-1951(96)00290-9

Boyce, A., Bastow, I. D., Golos, E. M., Rondenay, S., Burdick, S., & Van der Hilst, R. D. (2019, 11). Variable modification of continental lithosphere during the Proterozoic Grenville orogeny: Evidence from teleseismic P-wave tomography. *Earth and Planetary Science Letters*, *525*, 115763. doi: 10.1016/J.EPSL.2019.115763

Brito Neves, B. B. d., & Fuck, R. A. (2014). The basement of the South American

platform: Half Laurentian (N-NW)+half Gondwanan (E-SE) domains. *Precambrian Research*, *244*(1). doi: 10.1016/j.precamres.2013.09.020
Bruneton, M., Pedersen, H. A., Vacher, P., Kukkonen, I. T., Arndt, N. T., Funke, S., … Farra, V. (2004, 9). Layered lithospheric mantle in the central Baltic Shield from surface waves and xenolith analysis. *Earth and Planetary Science Letters*, *226*(1-2), 41–52. doi: 10.1016/j.epsl.2004.07.034
Carvalho, L. D., Jalowitzki, T., Scholz, R., Gonçalves, G. O., Rocha, M. P., Pereira, R. S., … Fuck, R. A. (2022, 1). An exotic Cretaceous kimberlite linked to metasomatized lithospheric mantle beneath the southwestern margin of the São Francisco Craton, Brazil. *Geoscience Frontiers*, *13*(1), 101281. doi: 10.1016/J.GSF.2021.101281
Cedraz, V., Julià, J., & Assumpção, M. (2020). Joint Inversion of Receiver Functions and Surface-Wave Dispersion in the Pantanal Wetlands: Implications for Basin Formation. *Journal of Geophysical Research: Solid Earth*, *125*(2). doi: 10.1029/2019JB018337
Celli, N. L., Lebedev, S., Schaeffer, A. J., Ravenna, M., & Gaina, C. (2020, 4). The upper mantle beneath the South Atlantic Ocean, South America and Africa from waveform tomography with massive data sets. *Geophysical Journal International*, *221*(1), 178–204. doi: 10.1093/gji/ggz574
Ciardelli, C., Assumpção, M., Bozdağ, E., & Lee, S. (2022, 2). Adjoint Waveform Tomography of South America. *Journal of Geophysical Research: Solid Earth*, *127*(2). doi: 10.1029/2021JB022575
Connolly, J. (2005, 7). Computation of phase equilibria by linear programming: A tool for geodynamic modeling and its application to subduction zone decarbonation. *Earth and Planetary Science Letters*, *236*(1-2), 524–541. doi: 10.1016/J.EPSL.2005.04.033
Cooper, C., Lenardic, A., & Moresi, L. (2004, 6). The thermal structure of stable continental lithosphere within a dynamic mantle. *Earth and Planetary Science Letters*, *222*(3-4), 807–817. doi: 10.1016/J.EPSL.2004.04.008
Cordani, U., Sato, K., Teixeira, W., Tassinari, C., & Basei, M. (2000). Crustal evolution of the South American platform. In *Tectonic evolution of south america.*
Cordani, U., Teixeira, W., D'Agrella-Filho, M., & Trindade, R. (2009, 6). The position of the Amazonian Craton in supercontinents. *Gondwana Research*, *15*(3-4), 396–407. doi: 10.1016/j.gr.2008.12.005
Cordani, U. G., Amaral, G., & Kawashita, K. (1973). The precambrian evolution of South America. *Geologische Rundschau*, *62*(2). doi: 10.1007/BF01840100
Cordani, U. G., Brito Neves, B. B., Fuck, R. A., Porto, R., Filho, A. T., & Bezerra Da Cunha, F. M. (2008). Estudo preliminar de integração do Pré-Cambriano com os eventos tectônicos das bacias sedimentares brasileiras (Republicação). In *Boletim de geociencias da petrobras* (Vol. 17).
Cordani, U. G., D'Agrella-Filho, M. S., Brito-Neves, B. B., & Trindade, R. I. (2003). Tearing up Rodinia: The neoproterozoic palaeogeography of South American cratonic fragments. *Terra Nova*, *15*(5). doi: 10.1046/j.1365-3121.2003.00506.x
Cordani, U. G., Ramos, V. A., Fraga, L. M., Cegarra, M., Delgado, I., Souza, K. G. d., … Schobbenhaus, C. (2016). Tectonic map of South America. *Comission de la carte géologique du monde*. doi: 10.14682/2016TEMSA
Cordani, U. G., & Teixeira, W. (2007). Proterozoic accretionary belts in the Amazonian Craton. In *Memoir of the geological society of america* (Vol. 200). doi: 10.1130/2007.1200(14)
Da Cruz Cunha, P. R., Gonçalves De Melo, J. H., & Da Silva, O. B. (2007). Bacia do Amazonas. *Boletim de Geociencias da Petrobras*, *15*(2).
D'Agrella-Filho, M. S., Bispo-Santos, F., Trindade, R. I. F., & Antonio, P. Y. J. (2016, 6). Paleomagnetism of the Amazonian Craton and its role in paleocontinents. *Brazilian Journal of Geology*, *46*(2), 275–299. doi:

10.1590/2317-4889201620160055
D'Agrella-Filho, M. S., Trindade, R. I., Elming, S. , Teixeira, W., Yokoyama, E., Tohver, E., ... Ruiz, A. S. (2012). The 1420Ma Indiavaí Mafic Intrusion (SW Amazonian Craton): Paleomagnetic results and implications for the Columbia supercontinent. *Gondwana Research*, *22*(3-4). doi: 10.1016/j.gr.2012.02.022
Daly, M. C., Andrade, V., Barousse, C. A., Costa, R., McDowell, K., Piggott, N., & Poole, A. J. (2014). Brasiliano crustal structure and the tectonic setting of the Parnaíba basin of NE Brazil: Results of a deep seismic reflection profile. *Tectonics*, *33*(11). doi: 10.1002/2014TC003632
Da Silva, L. C., McNaughton, N. J., Armstrong, R., Hartmann, L. A., & Fletcher, I. R. (2005). The neoproterozoic Mantiqueira Province and its African connections: A zircon-based U-Pb geochronologic subdivision for the Brasiliano/Pan-African systems of orogens. *Precambrian Research*, *136*(3-4). doi: 10.1016/j.precamres.2004.10.004
da Silva, L. C., Pedrosa-Soares, A. C., Teixeira, L. R., & Armstrong, R. (2008). Tonian rift-related, A-type continental plutonism in the Araçuaí Orogen, eastern Brazil: New evidence for the breakup stage of the São Francisco-Congo Paleocontinent. *Gondwana Research*, *13*(4). doi: 10.1016/j.gr.2007.06.002
Dave, R., & Li, A. (2016, 11). Destruction of the Wyoming craton: Seismic evidence and geodynamic processes. *Geology*, *44*(11), 883–886. doi: 10.1130/G38147.1
De Brito Neves, B. B., Campos Neto, M. D. C., & Fuck, R. A. (1999). *From Rodinia to Western Gondwana: An approach to the Brasiliano-Pan African cycle and orogenic collage* (Vol. 22) (No. 3). doi: 10.18814/epiiugs/1999/v22i3/002
de Min, A., Piccirillo, E. M., Marzoli, A., Bellieni, G., Renne, P. R., Ernesto, M., & Marques, L. S. (2003). The central atlantic magmatic province (CAMP) in Brazil: Petrology, geochemistry, 40Ar/39Ar ages, paleomagnetism and geodynamic implications. In *Geophysical monograph series* (Vol. 136). doi: 10.1029/136GM06
Dragone, G. N., Bologna, M. S., Ussami, N., Giménez, M. E., Alvarez, O., Lince Klinger, F. G., & Correa-Otto, S. (2021, 7). Lithosphere of South American intracratonic basins: Electromagnetic and potential field data reveal cratons, terranes, and sutures. *Tectonophysics*, *811*, 228884. doi: 10.1016/J.TECTO.2021.228884
Dragone, G. N., Ussami, N., Gimenez, M. E., Lince Klinger, F. G., & Chaves, C. A. M. (2017, 4). Western Paraná suture/shear zone and the limits of Rio Apa, Rio Tebicuary and Rio de la Plata cratons from gravity data. *Precambrian Research*, *291*, 162–177. doi: 10.1016/J.PRECAMRES.2017.01.029
Eakin, C. M. (2021). Quasi-Love wave scattering reveals tectonic history of Australia and its margins reflected by mantle anisotropy. *Communications Earth & Environment*, *2*(1). doi: 10.1038/s43247-021-00276-7
Eeken, T., Goes, S., Pedersen, H. A., Arndt, N. T., & Bouilhol, P. (2018, 6). Seismic evidence for depth-dependent metasomatism in cratons. *Earth and Planetary Science Letters*, *491*, 148–159. doi: 10.1016/j.epsl.2018.03.018
Eeken, T., Goes, S., Petrescu, L., & Altoe, I. (2020, 7). Lateral Variations in Thermochemical Structure of the Eastern Canadian Shield. *Journal of Geophysical Research: Solid Earth*, *125*(7). doi: 10.1029/2019JB018734
Faul, U. H., & Jackson, I. (2005, 5). The seismological signature of temperature and grain size variations in the upper mantle. *Earth and Planetary Science Letters*, *234*(1-2), 119–134. doi: 10.1016/J.EPSL.2005.02.008
Favetto, A., Rocha, V., Pomposiello, C., García, R., & Barcelona, H. (2015). A new limit for the NW Río de la plata craton border at about 24ºS (Argentina) detected by magnetotellurics. *Geologica Acta*, *13*(3). doi: 10.1344/GeologicaActa2015.13.3.6
Feng, M., Assumpção, M., & Van der Lee, S. (2004, 12). Group-velocity tomography and lithospheric S-velocity structure of the South American continent. *Physics*

of the Earth and Planetary Interiors, *147*(4), 315–331. doi: 10.1016/J.PEPI.2004.07.008

Feng, M., van der Lee, S., & Assumpção, M. (2007, 4). Upper mantle structure of South America from joint inversion of waveforms and fundamental mode group velocities of Rayleigh waves. *Journal of Geophysical Research: Solid Earth*, *112*(B4). doi: 10.1029/2006JB004449

Fernandes, C. M. D., Juliani, C., Monteiro, L. V. S., Lagler, B., & Echeverri Misas, C. M. (2011). High-K calc-alkaline to A-type fissure-controlled volcano-plutonism of the São Félix do Xingu region, Amazonian craton, Brazil: Exclusively crustal sources or only mixed Nd model ages? *Journal of South American Earth Sciences*, *32*(4). doi: 10.1016/j.jsames.2011.03.004

Finger, N., Kaban, M. K., Tesauro, M., Haeger, C., Mooney, W. D., & Thomas, M. (2021, 4). A Thermo-Compositional Model of the Cratonic Lithosphere of South America. *Geochemistry, Geophysics, Geosystems*, *22*(4). doi: 10.1029/2020GC009307

Flament, N., Gurnis, M., Müller, R. D., Bower, D. J., & Husson, L. (2015, 11). Influence of subduction history on South American topography. *Earth and Planetary Science Letters*, *430*, 9–18. doi: 10.1016/j.epsl.2015.08.006

Folguera, A., Orts, D., Spagnuolo, M., Vera, E. R., Litvak, V., Sagripanti, L., … Ramos, V. A. (2011). A review of Late Cretaceous to Quaternary palaeogeography of the southern Andes. *Biological Journal of the Linnean Society*, *103*(2). doi: 10.1111/j.1095-8312.2011.01687.x

Förste, C., Bruinsma, S., Abrikosov, O., Flechtner, F., Marty, J.-C., Lemoine, J.-M., … Marty, J.-c. (2014). EIGEN-6C4 - The latest combined global gravity field model including GOCE data up to degree and order 1949 of GFZ Potsdam and GRGS Toulouse. *EGU General Assembly*, *16*.

Fuck, R. A., Brito Neves, B. B., & Schobbenhaus, C. (2008). Rodinia descendants in South America. *Precambrian Research*, *160*(1-2). doi: 10.1016/j.precamres.2007.04.018

Gao, S., Rudnick, R. L., Yuan, H. L., Liu, X. M., Liu, Y. S., Xu, W. L., … Wang, Q. H. (2004). Recycling lower continental crust in the North China craton. *Nature*, *432*(7019). doi: 10.1038/nature03162

Garber, J. M., Maurya, S., Hernandez, J. A., Duncan, M. S., Zeng, L., Zhang, H. L., … Stixrude, L. (2018, 7). Multidisciplinary Constraints on the Abundance of Diamond and Eclogite in the Cratonic Lithosphere. *Geochemistry, Geophysics, Geosystems*, *19*(7), 2062–2086. doi: 10.1029/2018GC007534

Gibson, S. A., Thompson, R. N., & Day, J. A. (2006). Timescales and mechanisms of plume-lithosphere interactions: 40Ar/39Ar geochronology and geochemistry of alkaline igneous rocks from the Paraná-Etendeka large igneous province. *Earth and Planetary Science Letters*, *251*(1-2). doi: 10.1016/j.epsl.2006.08.004

Gilligan, A., Bastow, I. D., Watson, E., Darbyshire, F. A., Levin, V., Menke, W., … Petrescu, L. (2016, 8). Lithospheric deformation in the Canadian Appalachians: evidence from shear wave splitting. *Geophysical Journal International*, *206*(2), 1273–1280. doi: 10.1093/gji/ggw207

Góes, A. M. O., Souza, J. M. P., & Teixeira, L. B. (1990). Estágio Exploratório e Perspectivas Petrolíferas da Bacia do Parnaíba. *Boletim de Geociências da Petrobras*, *4*(1).

Griffin, W. L., O'Reilly, S. Y., Afonso, J. C., & Begg, G. C. (2009, 7). The Composition and Evolution of Lithospheric Mantle: a Re-evaluation and its Tectonic Implications. *Journal of Petrology*, *50*(7), 1185–1204. doi: 10.1093/petrology/egn033

Hacker, B. R. (2008, 3). H2O subduction beyond arcs. *Geochemistry, Geophysics, Geosystems*, *9*(3). doi: 10.1029/2007GC001707

Hackspacher, P. C., Godoy, D. F. d., Ribeiro, L. F. B., Hadler Neto, J. C., &

Franco, A. O. B. (2007). Modelagem térmica e geomorfologia da borda sul do Cráton do São Francisco: termocronologia por traços de fissão em apatita. *Revista Brasileira de Geociências*, *37*(S4). doi: 10.25249/0375-7536.200737s47686

Hajnal, Z., Nemeth, B., Clowes, R. M., Ellis, R. M., Spence, G. D., Burianyk, M. J., ... Forsyth, D. A. (1997). Mantle involvement in lithospheric collision: Seismic evidence from the Trans-Hudson Orogen, western Canada. *Geophysical Research Letters*, *24*(16). doi: 10.1029/97GL01958

Hartigan, J. A. (1975). *Clustering algorithms* (Wiley, Ed.). New York.

Hartigan, J. A., & Wong, M. A. (1979). Algorithm AS 136: A K-Means Clustering Algorithm. *Applied Statistics*, *28*(1), 100. doi: 10.2307/2346830

Heilbron, M., & Machado, N. (2003). Timing of terrane accretion in the Neoproterozoic-Eopaleozoic Ribeira Orogen (se Brazil). *Precambrian Research*, *125*(1-2). doi: 10.1016/S0301-9268(03)00082-2

Heintz, M., Debayle, E., & Vauchez, A. (2005, 8). Upper mantle structure of the South American continent and neighboring oceans from surface wave tomography. *Tectonophysics*, *406*(1-2), 115–139. doi: 10.1016/J.TECTO.2005.05.006

Herzberg, C., Asimow, P. D., Arndt, N., Niu, Y., Lesher, C. M., Fitton, J. G., ... Saunders, A. D. (2007, 2). Temperatures in ambient mantle and plumes: Constraints from basalts, picrites, and komatiites. *Geochemistry, Geophysics, Geosystems*, *8*(2). doi: 10.1029/2006GC001390

Hieronymus, C. F., & Goes, S. (2010, 3). Complex cratonic seismic structure from thermal models of the lithosphere: effects of variations in deep radiogenic heating. *Geophysical Journal International*, *180*(3), 999–1012. doi: 10.1111/j.1365-246X.2009.04478.x

Holland, T. J., & Powell, R. (1998). An internally consistent thermodynamic data set for phases of petrological interest. *Journal of Metamorphic Geology*, *16*(3), 309–343. doi: 10.1111/j.1525-1314.1998.00140.x

Hopper, E., & Fischer, K. M. (2015, 12). The meaning of midlithospheric discontinuities: A case study in the northern U.S. craton. *Geochemistry, Geophysics, Geosystems*, *16*(12), 4057–4083. doi: 10.1002/2015GC006030

Horton, B. K. (2018). *Sedimentary record of Andean mountain building* (Vol. 178). doi: 10.1016/j.earscirev.2017.11.025

Hu, J., Liu, L., Faccenda, M., Zhou, Q., Fischer, K. M., Marshak, S., & Lundstrom, C. (2018, 3). Modification of the Western Gondwana craton by plume–lithosphere interaction. *Nature Geoscience*, *11*(3), 203–210. Retrieved from `http://www.nature.com/articles/s41561-018-0064-1` doi: 10.1038/s41561-018-0064-1

IBGE. (2010). Atlas Nacional do Brasil Milton Santos - Bacias de produção de petróleo.

Jordan, T. H. (1978, 8). Composition and development of the continental tectosphere. *Nature*, *274*(5671), 544–548. doi: 10.1038/274544a0

Julià, J., Assumpção, M., & Rocha, M. P. (2008, 8). Deep crustal structure of the Paraná Basin from receiver functions and Rayleigh-wave dispersion: Evidence for a fragmented cratonic root. *Journal of Geophysical Research: Solid Earth*, *113*(8). doi: 10.1029/2007JB005374

Kaufman, L., & Rousseeuw, P. J. (1990). *Finding groups in data : an introduction to cluster analysis* (Wiley, Ed.). New York.

King, S. D., & Ritsema, J. (2000, 11). African Hot Spot Volcanism: Small-Scale Convection in the Upper Mantle Beneath Cratons. *Science*, *290*(5494), 1137–1140. doi: 10.1126/SCIENCE.290.5494.1137

Krueger, H. E., Gama, I., & Fischer, K. M. (2021, 6). Global Patterns in Cratonic Mid-Lithospheric Discontinuities From Sp Receiver Functions. *Geochemistry, Geophysics, Geosystems*, *22*(6). doi: 10.1029/2021GC009819

Laske, G., Masters, G., Ma, Z., & Pasyanos, M. (2013). Update on CRUST1.0—A 1-

degree global model of Earth's crust. In *Egu general assembly 2013* (Vol. 15).

Lee, C.-T., & Rudnick, R. L. (1999). Compositionally stratified cratonic lithosphere: petrology and geochemistry of peridotite xenoliths from the Labait tuff cone, Tanzania. In S. R. Gurney J. J. & Richardson (Ed.), *International kimberlite conference* (pp. 503–521). Cape Town: Red Roof Design.

Lee, C. T. A., Cheng, X., & Horodyskyj, U. (2006). The development and refinement of continental arcs by primary basaltic magmatism, garnet pyroxenite accumulation, basaltic recharge and delamination: Insights from the Sierra Nevada, California. *Contributions to Mineralogy and Petrology*, *151*(2). doi: 10.1007/s00410-005-0056-1

Lee, C.-T. A., Luffi, P., & Chin, E. J. (2011, 5). Building and Destroying Continental Mantle. *Annual Review of Earth and Planetary Sciences*, *39*(1), 59–90. doi: 10.1146/annurev-earth-040610-133505

Legendre, C. P., Meier, T., Lebedev, S., Friederich, W., & Viereck-Götte, L. (2012). A shear wave velocity model of the European upper mantle from automated inversion of seismic shear and surface waveforms. *Geophysical Journal International*. doi: 10.1111/j.1365-246X.2012.05613.x

Lekic, V., Cottaar, S., Dziewonski, A., & Romanowicz, B. (2012, 12). Cluster analysis of global lower mantle tomography: A new class of structure and implications for chemical heterogeneity. *Earth and Planetary Science Letters*, *357-358*, 68–77. doi: 10.1016/j.epsl.2012.09.014

Li, C., Van Der Hilst, R. D., Engdahl, E. R., & Burdick, S. (2008). A new global model for P wave speed variations in Earth's mantle. *Geochemistry, Geophysics, Geosystems*, *9*(5). doi: 10.1029/2007GC001806

Liddell, M., Bastow, I., Rawlinson, N., Darbyshire, F., Gilligan, A., & Watson, E. (2018, 7). Precambrian Plate Tectonics in Northern Hudson Bay: Evidence from P and S-wave Seismic Tomography and Analysis of Source Side Effects in Relative Arrival-Time Datasets. *Journal of Geophysical Research: Solid Earth*, *123*(7), 5690–5709. doi: 10.1029/2018JB015473

Liu, J., Pearson, D. G., Wang, L. H., Mather, K. A., Kjarsgaard, B. A., Schaeffer, A. J., ... Armstrong, J. P. (2021, 4). Plume-driven recratonization of deep continental lithospheric mantle. *Nature 2021 592:7856*, *592*(7856), 732–736. doi: 10.1038/s41586-021-03395-5

Lloyd, S., van der Lee, S., França, G. S., Assumpção, M., & Feng, M. (2010, 11). Moho map of South America from receiver functions and surface waves. *Journal of Geophysical Research*, *115*(B11), B11315. doi: 10.1029/2009JB006829

Mantovani, M., Quintas, M., Shukowsky, W., & Brito Neves, B. (2005, 3). Delimitation of the Paranapanema Proterozoic block: A geophysical contribution. *Episodes*, *28*(1), 18–22. doi: 10.18814/epiiugs/2005/v28i1/002

Marzoli, A., Renne, P. R., Piccirillo, E. M., Ernesto, M., Bellieni, G., & De Min, A. (1999, 4). Extensive 200-million-year-old continental flood basalts of the Central Atlantic Magmatic Province. *Science*, *284*(5414), 616–618. doi: 10.1126/SCIENCE.284.5414.616/ASSET/E9EE98F9-2D6C-4492-A99B-591A3AA72581/ASSETS/GRAPHIC/SE1397399005.JPEG

Masters, G., Woodhouse, J., & Freeman, G. (2011). *Mineos v1.0.2.* Computational Infrastructure for Geodynamics.

Menegazzo, M. C., Catuneanu, O., & Chang, H. K. (2016, 5). The South American retroarc foreland system: The development of the Bauru Basin in the back-bulge province. *Marine and Petroleum Geology*, *73*, 131–156. doi: 10.1016/j.marpetgeo.2016.02.027

Milani, E. J. (2004). Comentários sobre a origem e a evolução tectônica da Bacia do Paraná. In V. Mantesso-Neto, A. Bartorelli, C. D. R. Carneiro, & B. B. d. Brito Neves (Eds.), *Geologia do continente sul-americano: Evolução da obra de fernando flávio marqués de almeida* (pp. 265–291). São Paulo: Beca.

Milani, E. J., & Ramos, V. A. (1998). Orogenias Paleozóicas no Domínio Sul-ocidental do Gondwana e os ciclos de subsidência da Bacia do Paraná. *Revista Brasileira de Geociências*, *28*(4), 473–484.

Milani, E. J., & Zalán, P. V. (1999). An outline of the geology and petroleum systems of the Paleozoic interior basins of South America. *Episodes*, *22*(3). doi: 10.18814/epiiugs/1999/v22i3/007

Miller, M. S., & Eaton, D. W. (2010, 9). Formation of cratonic mantle keels by arc accretion: Evidence from S receiver functions. *Geophysical Research Letters*, *37*(18). doi: 10.1029/2010GL044366

Mizusaki, A. M., Petrini, R., Bellieni, P., Comin-Chiaramonti, P., Dias, J., De Min, A., & Piccirillo, E. M. (1992). Basalt magmatism along the passive continental margin of SE Brazil (Campos basin). *Contributions to Mineralogy and Petrology*, *111*(2). doi: 10.1007/BF00348948

Montagner, J. P., & Kennett, B. L. (1996). How to reconcile body-wave and normal-mode reference earth models. *Geophysical Journal International*, *125*(1). doi: 10.1111/j.1365-246X.1996.tb06548.x

Neves, B. B. d. B., Fuck, R. A., & Pimentel, M. M. (2014, 11). The Brasiliano collage in South America: a review. *Brazilian Journal of Geology*, *44*(3), 493–518. doi: 10.5327/Z2317-4889201400030010

O'Reilly, S. Y., & Griffin, W. L. (2010, 11). The continental lithosphere-asthenosphere boundary: Can we sample it? *Lithos*, *120*(1-2), 1–13. doi: 10.1016/j.lithos.2010.03.016

Oriolo, S., Oyhantçabal, P., Wemmer, K., & Siegesmund, S. (2017, 11). Contemporaneous assembly of Western Gondwana and final Rodinia break-up: Implications for the supercontinent cycle. *Geoscience Frontiers*, *8*(6), 1431–1445. doi: 10.1016/j.gsf.2017.01.009

Oyhantçabal, P., Siegesmund, S., & Wemmer, K. (2010, 8). The Río de la Plata Craton: a review of units, boundaries, ages and isotopic signature. *International Journal of Earth Sciences 2010 100:2*, *100*(2), 201–220. doi: 10.1007/S00531-010-0580-8

Pankhurst, R. J., Trouw, R. A. J., Neves, B. B. B., & Wit, M. J. (2008). *West Gondwana: Pre-Cenozoic Correlations Across the South Atlantic Region* (Vol. 294).

Pavlis, N. K., Holmes, S. A., Kenyon, S. C., & Factor, J. K. (2012, 4). The development and evaluation of the Earth Gravitational Model 2008 (EGM2008). *Journal of Geophysical Research: Solid Earth*, *117*(B4), n/a-n/a. doi: 10.1029/2011JB008916

Pearson, D. G., Canil, D., & Shirey, S. B. (2013). Mantle Samples Included in Volcanic Rocks: Xenoliths and Diamonds. Xenoliths and Diamonds. In *Treatise on geochemistry: Second edition* (Vol. 3). doi: 10.1016/B978-0-08-095975-7.00216-3

Pearson, D. G., Scott, J. M., Liu, J., Schaeffer, A., Wang, L. H., van Hunen, J., ... Kelemen, P. B. (2021, 8). Deep continental roots and cratons. *Nature*, *596*(7871), 199–210. doi: 10.1038/s41586-021-03600-5

Pedreira, A. J., & Bahia, R. B. C. (2004). Estratigrafia e Evolução da Bacia dos Parecis Região Amazônica, Brasil. *Serviço Geológico do Brasil*.

Perchuk, A. L., Gerya, T. V., Zakharov, V. S., & Griffin, W. L. (2020, 10). Building cratonic keels in Precambrian plate tectonics. *Nature*, *586*(7829), 395–401. doi: 10.1038/s41586-020-2806-7

Pilger, R. H. (1984). Cenozoic plate kinematics, subduction and magmatism: South American Andes. *Journal of the Geological Society*, *141*(5). doi: 10.1144/gsjgs.141.5.0793

Portner, D. E., Rodríguez, E. E., Beck, S., Zandt, G., Scire, A., Rocha, M. P., ... Alvarado, P. (2020, 5). Detailed Structure of the Subducted Nazca Slab into the Lower Mantle Derived From Continent-Scale Teleseismic P Wave

Tomography. *Journal of Geophysical Research: Solid Earth*, *125*(5). doi: 10.1029/2019JB017884

Pysklywec, R. N., & Quintas, M. C. (2000, 7). A mantle flow mechanism for the late Paleozoic subsidence of the Paraná Basin. *Journal of Geophysical Research: Solid Earth*, *105*(B7), 16359–16370. doi: 10.1029/2000JB900080/FORMAT/PDF

Ramos, V. A. (1999). *Plate tectonic setting of the Andean Cordillera* (Vol. 22) (No. 3). doi: 10.18814/epiiugs/1999/v22i3/005

Ramos, V. A. (2009). Anatomy and global context of the Andes: Main geologic features and the Andean orogenic cycle. In *Memoir of the geological society of america* (Vol. 204). doi: 10.1130/2009.1204(02)

Ramos, V. A., & Folguera, A. (2009). Andean flat-slab subduction through time. *Geological Society Special Publication*, *327*. doi: 10.1144/SP327.3

Rapela, C. W., Fanning, C. M., Casquet, C., Pankhurst, R. J., Spalletti, L., Poiré, D., & Baldo, E. G. (2011). *The Rio de la Plata craton and the adjoining Pan-African/brasiliano terranes: Their origins and incorporation into south-west Gondwana* (Vol. 20) (No. 4). doi: 10.1016/j.gr.2011.05.001

Rapela, C. W., Pankhurst, R. J., Casquet, C., Fanning, C. M., Baldo, E. G., González-Casado, J. M., . . . Dahlquist, J. (2007, 7). The Río de la Plata craton and the assembly of SW Gondwana. *Earth-Science Reviews*, *83*(1-2), 49–82. doi: 10.1016/J.EARSCIREV.2007.03.004

Ren, Y., Stutzmann, E., van der Hilst, R. D., & Besse, J. (2007). Understanding seismic heterogeneities in the lower mantle beneath the Americas from seismic tomography and plate tectonic history. *Journal of Geophysical Research: Solid Earth*, *112*(1). doi: 10.1029/2005JB004154

Renne, P. R., Ernesto, M., Pacca, I. G., Coe, R. S., Glen, J. M., Prévot, M., & Perrin, M. (1992). The age of Paraná flood volcanism, rifting of Gondwanaland, and the Jurassic-Cretaceous boundary. *Science*, *258*(5084). doi: 10.1126/science.258.5084.975

Renne, P. R., Glen, J. M., Milner, S. C., & Duncan, A. R. (1996). Age of Etendeka flood volcanism and associated intrusions in southwestern Africa. *Geology*, *24*(7). doi: 10.1130/0091-7613(1996)024⟨0659:AOEFVA⟩2.3.CO;2

Richards, F., Hoggard, M., Crosby, A., Ghelichkhan, S., & White, N. (2020). *Structure and dynamics of the oceanic lithosphere-asthenosphere system* (Vol. 309). doi: 10.1016/j.pepi.2020.106559

Richards, F. D., Hoggard, M. J., Cowton, L. R., & White, N. J. (2018). Reassessing the Thermal Structure of Oceanic Lithosphere With Revised Global Inventories of Basement Depths and Heat Flow Measurements. *Journal of Geophysical Research: Solid Earth*, *123*(10). doi: 10.1029/2018JB015998

Rivadeneyra-Vera, C., Bianchi, M., Assumpção, M., Cedraz, V., Julià, J., Rodríguez, M., . . . Fernandez, G. (2019). An updated crustal thickness map of central South America based on receiver function measurements in the region of the Chaco, Pantanal, and Paraná Basins, southwestern Brazil. *Journal of Geophysical Research: Solid Earth*, *124*(8), 8491–8505. doi: 10.1029/2018JB016811

Rodríguez, E. E., Portner, D. E., Beck, S. L., Rocha, M. P., Bianchi, M. B., Assumpção, M., . . . Lynner, C. (2021, 1). Mantle dynamics of the Andean Subduction Zone from continent-scale teleseismic S-wave tomography. *Geophysical Journal International*, *224*(3), 1553–1571. doi: 10.1093/GJI/GGAA536

Rosa, M. L., Collaço, B., Assumpção, M., Sabbione, N., & Sánchez, G. (2016, 3). Thin crust beneath the Chaco-Paraná Basin by surface-wave tomography. *Journal of South American Earth Sciences*, *66*, 1–14. Retrieved from `https://www.sciencedirect.com/science/article/pii/S0895981115300900` doi: 10.1016/J.JSAMES.2015.11.010

Rousseeuw, P. J. (1987, 11). Silhouettes: A graphical aid to the interpretation and validation of cluster analysis. *Journal of Computational and Applied Math-*

ematics, *20*(C), 53–65. doi: 10.1016/0377-0427(87)90125-7

Schaeffer, A. J., & Lebedev, S. (2015). Global Heterogeneity of the Lithosphere and Underlying Mantle: A Seismological Appraisal Based on Multimode Surface-Wave Dispersion Analysis, Shear-Velocity Tomography, and Tectonic Regionalization. In *The earth's heterogeneous mantle* (pp. 3–46). Cham: Springer International Publishing. doi: 10.1007/978-3-319-15627-9{_}1

Selway, K., Ford, H., & Kelemen, P. (2015, 3). The seismic mid-lithosphere discontinuity. *Earth and Planetary Science Letters*, *414*, 45–57. doi: 10.1016/J.EPSL.2014.12.029

Sleep, N. H. (2005). Evolution of the continental lithosphere. *Annual Review of Earth and Planetary Sciences*, *33*(1), 369–393. doi: 10.1146/annurev.earth.33.092203.122643

Soares, J. E., Berrocal, J., Fuck, R. A., Mooney, W. D., & Ventura, D. B. R. (2006, 12). Seismic characteristics of central Brazil crust and upper mantle: A deep seismic refraction study. *Journal of Geophysical Research: Solid Earth*, *111*(B12), n/a-n/a. doi: 10.1029/2005JB003769

Soares, J. E. P., Fuck, R. A., Oliveira, M. P. d., & Lima, M. V. d. (2011). Descontinuidade de Moho e velocidade média da crosta sob a linha de refração sísmica profunda N-S da Província Borborema: uma aproximação por reflexões de alto ângulo.. doi: 10.1190/sbgf2011-084

Soares, P. C., Barbosa Landim, P. M., & Fulfaro, V. J. (1978). Tectonic cycles and sedimentary sequences in the Brazilian intracratonic basins. *Bulletin of the Geological Society of America*, *89*(2). doi: 10.1130/0016-7606(1978)89⟨181:TCASSI⟩2.0.CO;2

Teixeira, W., & Figueiredo, M. C. H. (1991). An outline of Early Proterozoic crustal evolution in the São Francisco craton, Brazil: a review. *Precambrian Research*, *53*(1-2). doi: 10.1016/0301-9268(91)90003-S

Trompette, R. (1994). Geology of western Gondwana (2000-500 Ma): Pan-African-Brasiliano aggregation of South America and Africa. *Geology of western Gondwana (2000-500 Ma): Pan-African-Brasiliano aggregation of South America and Africa*. doi: 10.1016/0301-9268(95)00062-3

Turcotte, D. L., & Schubert, G. (2002). Geodynamics - 2nd Edition. *geod*, 472. doi: 10.2277/0521661862

Uieda, L., & Barbosa, V. C. (2017). Fast nonlinear gravity inversion in spherical coordinates with application to the South AmericanMoho. *Geophysical Journal International*, *208*(1). doi: 10.1093/gji/ggw390

Ussami, N., Shiraiwa, S., & Dominguez, J. M. L. (1999). Basement reactivation in a sub-Andean foreland flexural bulge: The Pantanal wetland, SW Brazil. *Tectonics*, *18*(1). doi: 10.1029/1998TC900004

Van Decar, J. C., James, D. E., & Assumpção, M. (1995). Seismic evidence for a fossil mantle plume beneath south america and implications for plate driving forces. *Nature*, *378*(6552). doi: 10.1038/378025a0

van der Lee, S., James, D., & Silver, P. (2001, 12). Upper mantle ¡i¿S¡/i¿ velocity structure of central and western South America. *Journal of Geophysical Research: Solid Earth*, *106*(B12), 30821–30834. doi: 10.1029/2001JB000338

van der Meijde, M., Julià, J., & Assumpção, M. (2013, 12). Gravity derived Moho for South America. *Tectonophysics*, *609*, 456–467. doi: 10.1016/J.TECTO.2013.03.023

van Hunen, J., & Moyen, J.-F. (2012, 5). Archean Subduction: Fact or Fiction? *Annual Review of Earth and Planetary Sciences*, *40*(1), 195–219. doi: 10.1146/annurev-earth-042711-105255

Wang, H., van Hunen, J., & Pearson, D. G. (2015, 4). The thinning of subcontinental lithosphere: The roles of plume impact and metasomatic weakening. *Geochemistry, Geophysics, Geosystems*, *16*(4), 1156–1171. doi: 10.1002/2015GC005784

Weller, O., Copley, A., Miller, W., Palin, R., & Dyck, B. (2019, 7). The relationship between mantle potential temperature and oceanic lithosphere buoyancy. *Earth and Planetary Science Letters*, *518*, 86–99. doi: 10.1016/J.EPSL.2019.05.005

Xu, W., Lithgow-Bertelloni, C., Stixrude, L., & Ritsema, J. (2008). The effect of bulk composition and temperature on mantle seismic structure. *Earth and Planetary Science Letters*, *275*(1-2), 70–79. doi: 10.1016/j.epsl.2008.08.012

Zalán, P. V., Wolff, S., Astolfi, M. A. M., Vieira, I. S., Concelção, J. C. J., Appi, V. T., ... Marques, A. (1990, 5). The Paraná Basin, Brazil. In *Interior cratonic basins.* American Association of Petroleum Geologists. doi: 10.1306/M51530C34

Supporting Information for:
Thermo-compositional structure of the South American Platform lithosphere: Evidence of stability, modification and erosion.

Isabella Altoe[1], Saskia Goes[1], and Marcelo Assumpção[2]

[1] *Department of Earth Science and Engineering, Imperial College London, UK*
[2] *Department of Geophysics, IAG, University of São Paulo, São Paulo, Brazil*
Corresponding Author: i.altoe17@imperial.ac.uk

Contents of this file

1. Figures S1 to S16
2. Tables S1 to S5

Table S1 - Variability within the clusters to inter cluster distance

Cluster/Ave. distance to cluster	C1	C2	C3	C4	C5	C6
C1	0.0513	0.6220	0.2120	0.3704	0.2796	0.5156
C2	0.6120	0.0373	0.6046	0.3010	0.1294	0.1132
C3	0.1926	0.5991	0.0319	0.1319	0.3307	0.3474
C4	0.3478	0.2923	0.1287	0.0286	0.2015	0.1070
C5	0.2614	0.1252	0.3320	0.2060	0.0331	0.1297
C6	0.4849	0.0965	0.3362	0.0990	0.1172	0.0207

Average distance of the points in a cluster to every centroid for our preferred solution with six clusters. For six clusters, the within-cluster distance is lower than the distance between clusters. For more clusters, the average distances within and between clusters become similar.

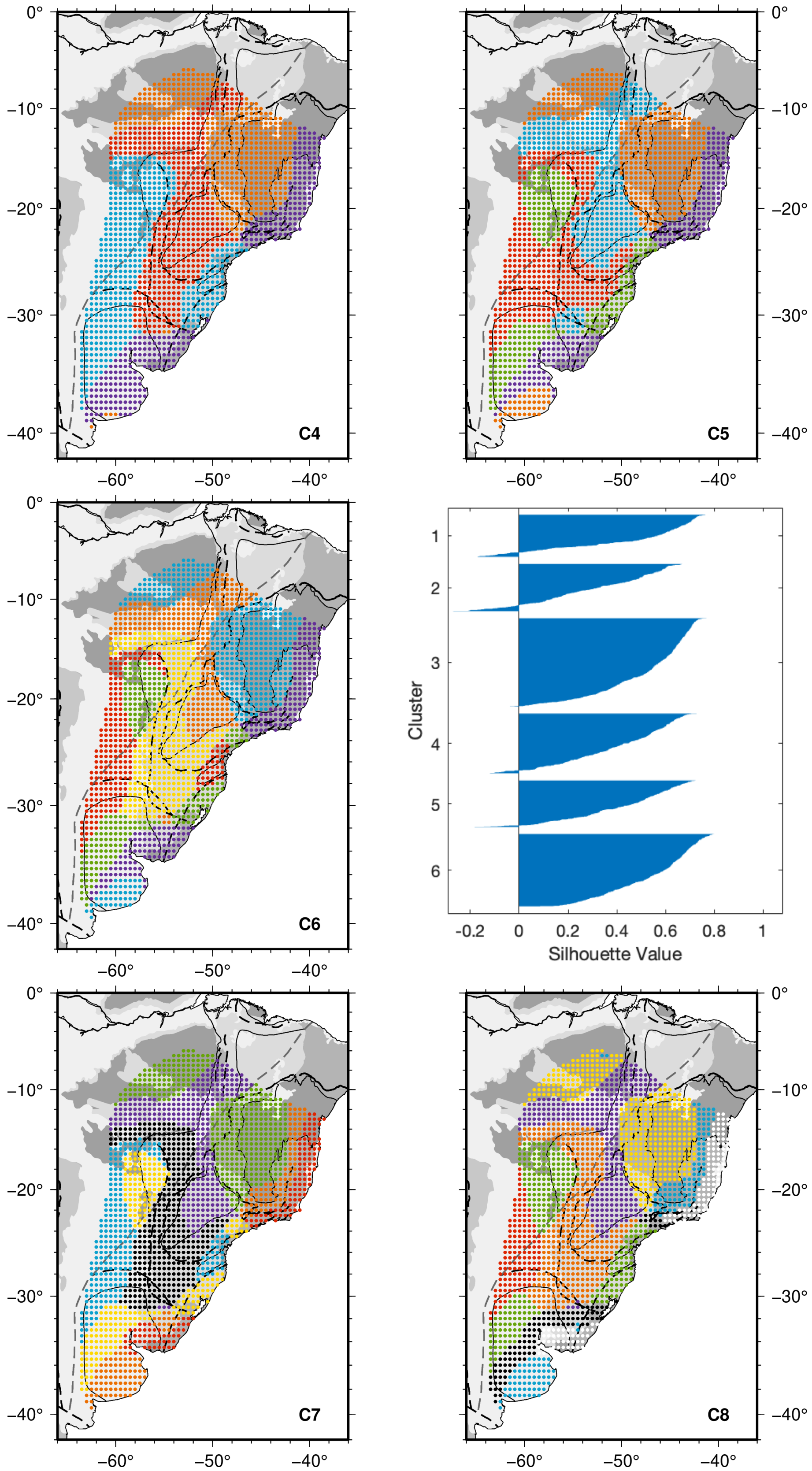

Figure S1 - Maps showing the k-means solutions for 4 to 8 clusters (labelled C4 through C8) and silhouette plot for 6 clusters. Each cluster generated by the cluster analysis is represented by one colour. On map C6, the black dots are the ones that have negative silhouette values and/or are geographic isolated and therefore were removed from further analysis.

Table S2 - Thermal Parameters

	Fixed parameters	**Value**	**Ref.**
k_c	Crustal thermal conductivity	2.7 $Wm^{-1}K^{-1}$	(Hasterok & Chapman, 2011; Michaut et al., 2007)
k_m	Mantle thermal conductivity	3.0 $Wm^{-1}K^{-1}$	(Hasterok & Chapman, 2011; Michaut et al., 2007)
A_{uc}	Upper crustal heat production	0.8 μWm^3	(Hasterok & Chapman, 2011; Michaut et al., 2007; Rudnick & Nyblade, 1999)
A_{lc}	Lower crustal heat production	0.4 μWm^3	(Hasterok & Chapman, 2011; Michaut et al., 2007; Rudnick & Nyblade, 1999)
A_m	Lithospheric mantle heat production	0.01 μWm^3	(Hasterok & Chapman, 2011; Michaut et al., 2007)
	Variable parameters	**Range** (increment)	**Ref.**
q_m	Moho heat flow	10-35 (1.0) mWm^{-2}	(Lévy & Jaupart, 2011; Shapiro et al., 2004)
T_{pot}	Mantle potential temperature	1100-1300 (50)°C	(Herzberg et al., 2007)
	Obtained parameters	**Range**	**Ref.**
q_s	Surface heat flow	31-62 mWm^{-2}	(Lévy & Jaupart, 2011; Shapiro et al., 2004)
L_T	Thermal lithospheric thickness	90-360 km	(Jaupart & Mareschal, 1999)

Crustal thickness for each group is given in Table S3 - Crustal Parameters

Table S3 - Crustal Parameters

Groups	H (km)	ρ_{uc} (kg/m^3)	ρ_{lc} (kg/m^3)	$V_{\text{p-uc}}$ (m/s)	$V_{\text{s-uc}}$ (m/s)	$V_{\text{p-lc}}$ (m/s)	$V_{\text{s-lc}}$ (m/s)
3AmC	36 - 40	2780	2910	6290	3640	6810	3850-4000
3SFC	37 - 41	2760	2970	6250	3580	7020	3950-4100
4PcB	38 - 42	2760	2920	6200	3570	6890	3900-4050
4PrB	42 - 46	2730	3000	6160	3520	7090	4000-4150
6PrB(n)	34 - 37	2760	2940	6260	3590	6950	3900-4050
6PrB(w)	39 - 43	2730	2980	6130	3500	7060	4000-4150
6PrB(s)	39 - 43	2750	2930	6110	3500	6920	3900-4050
5PtB	38 - 42	2740	2970	6240	3520	7015	3900-4050
2ChB	38 - 41	2700	2960	6100	3400	6990	3900-4050
2LAC	37 - 41	2760	2910	6230	3600	6800	3950-4000
5RPC	37 - 41	2730	2960	6130	3510	7000	3950-4100
3RPC	33 - 37	2700	2980	6030	3470	7070	4000-4150

Crustal parameters used for each group. H is crustal thickness, ρ is density, uc is upper crust, lc is lower crust, V_p is P-wave velocity, V_s is S-wave velocity. The depth of the upper-lower crust boundary is 2/3 of the crustal thickness. Groups: 3Amc (Amazonian Craton), 3SFC (São Francisco Craton), 4PcB (Parecis Basin), 4PrB (Paraná Basin), 6PrB(n) (Paraná Basin north), 6PrB(w) (Paraná Basin west), 6PrB(s) (Paraná Basin south), 5PtB (Pantanal Basin), 2ChB (Chaco Basin), 2LAC (Luiz Alves Craton), 5RPC (Rio de la Plata Craton), 3RPC (Rio de la Plata Craton) (see map in Fig. 3). Data from Rivadeneyra-Vera et al. (2019) and CRUST1.0 (Laske et al., 2013)

Table S4 - Compositions considered

Composition (wt%)	SiO_2	TiO_2	Al_2O_3	FeO	MnO	MgO	CaO	Na_2O	K_2O	H_2O
ARC9 (Dunite)	42.90	0.01	0.30	6.50	0.15	49.20	0.10	0.10		
ARC4 (lherzolite)	44.3	0.17	1.74	8.1	0.12	43.3	1.27	0.12		
Pyrolite	44.93	0.00	4.37	8.56		38.82	3.19	0.13		
MORB	50.6	1.5	15.7	10.6		7.6	11.1	2.6	0.2	
ARC9 with 0.215 wt% H2O	42.90	0.01	0.30	6.50		49.20	0.10	0.10		0.215
ARC9 with 5wt% phl	43.28	00.1	0.90	6.23		48.61	0.10	0.10	0.57	0.22

References: ARC9 and ARC4 from Griffin et al. (2009), Pyrolite from Xu et al. (2008), MORB from Hacker (2008).

Table S5 - Solid-solution models used

Abbreviation	**Mineral**	**Ref.**
Act(M)	low-pressure amphibole	(Massonne, 2008)
Atg(PN)	antigorite	(Padrón-Navarta et al., 2013)
Chl(HP)	chlorite	(T. Holland et al., 1998)
Cpx(HP)	clinopyroxene	(T. Holland & Powelll, 1996)
Ctd(HP)	chloritoid	(White et al., 2000)
GlTrTsPg	clinoamphibole	(Wei & Powell, 2003; White et al., 2003)
Gt(HP)	garnet	(T. J. Holland & Powell, 1998)
O(HP)	olivine	(T. J. Holland & Powell, 1998)
Opx(HP)	orthopyroxene	(T. Holland & Powelll, 1996)
Pl(h)	feldspar	(Newton et al., 1980)
Sp(JR)	spinel	(Jamieson & Roeder, 1984)
T	talc	ideal

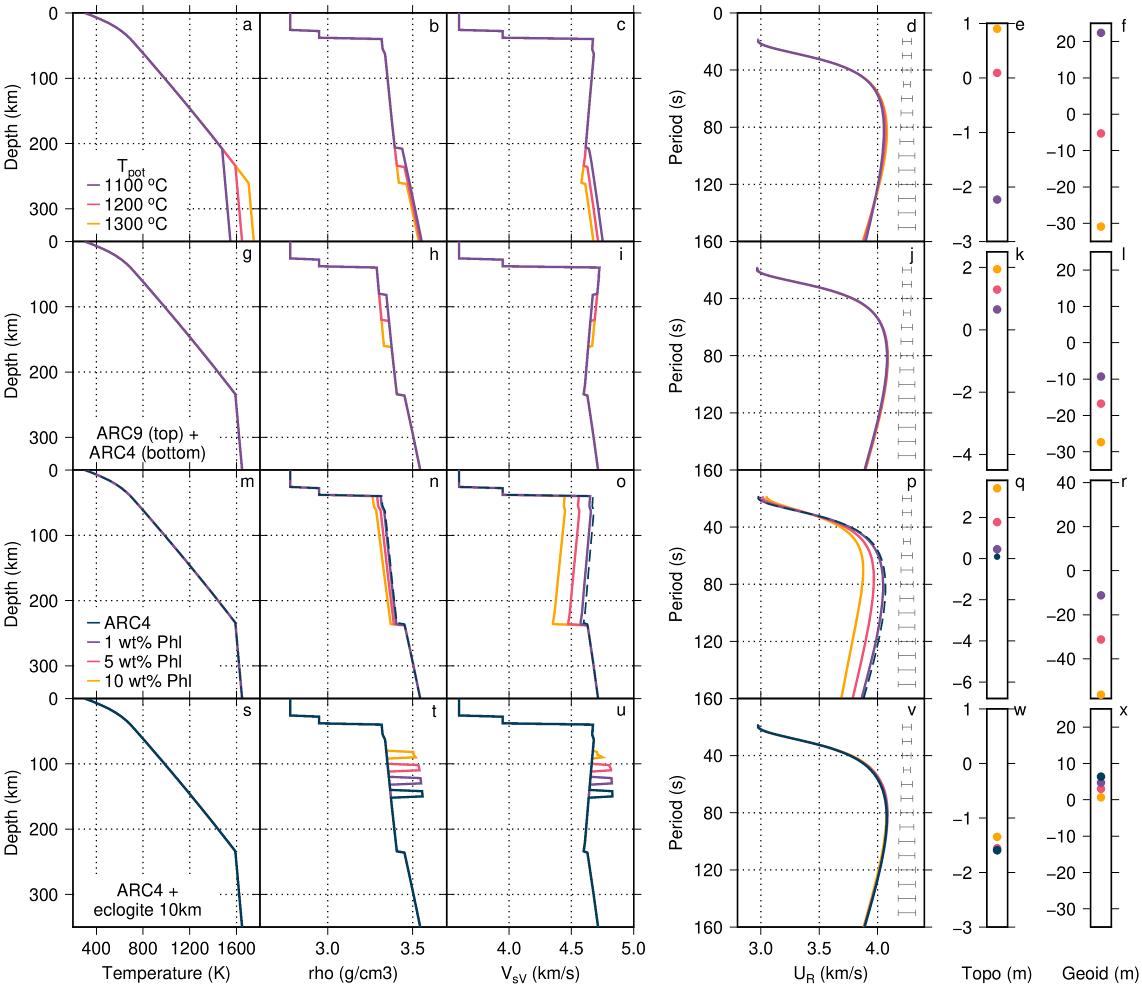

Figure S2 Sensitivity analysis of group Rayleigh-wave dispersion curves, topography, and geoid height to different mantle potential temperature (first row), layered background composition (second row), plhogopite content (third row), and a layer of eclogite at different depths (forth row) . For each set of tests, the left hand side shows the geotherms (a, g, m, and s), the density (b, h, n, and t) and the velocity profiles (c, i, o, and u). The right hand side shows the effect of the different thermal and compositional parameters to the group Rayleigh-wave dispersion curves (d, i, p, and v), topography (e, k, q, and w) and geoid (f, l, r, and x).

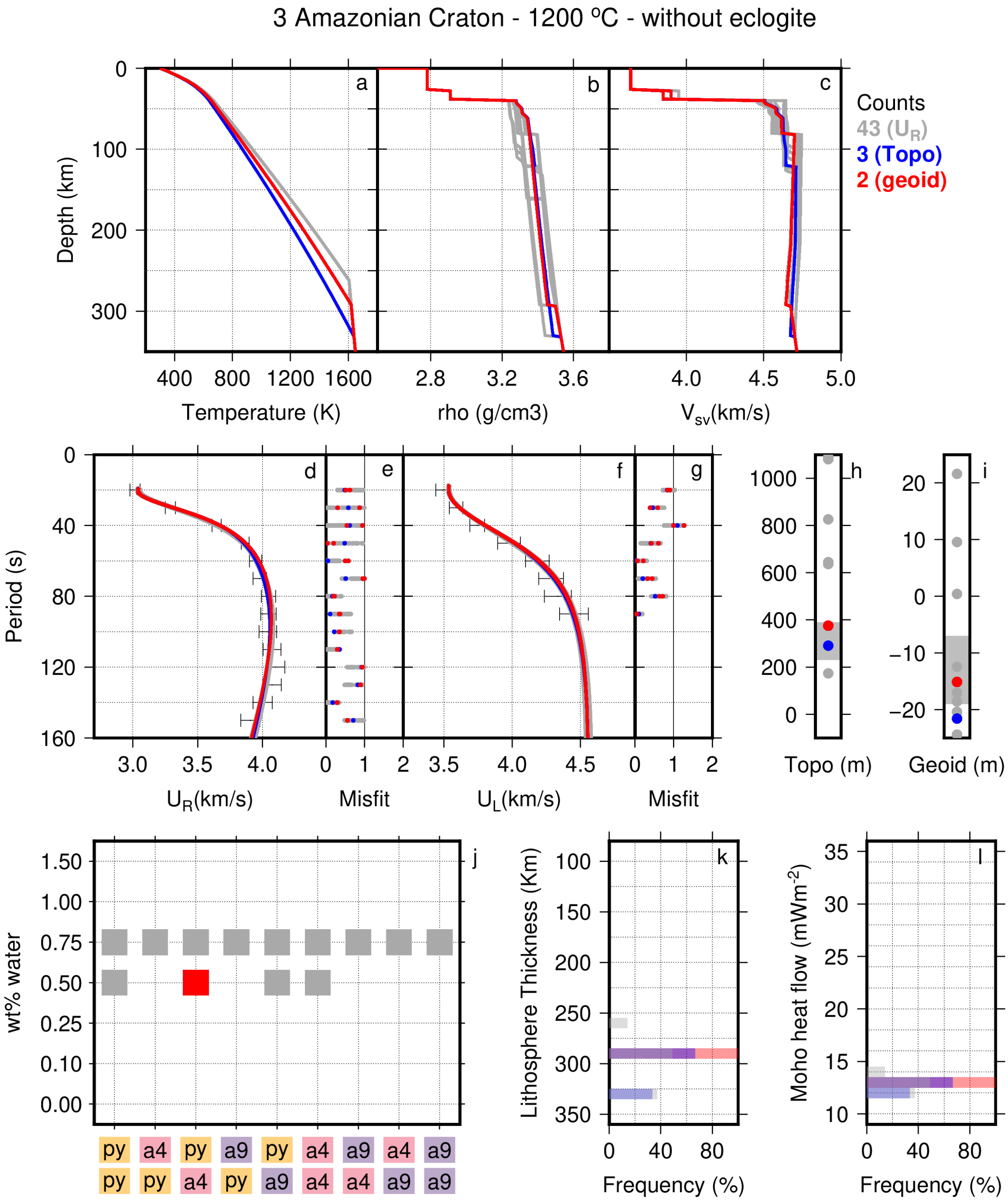

Figure S3 Set of solutions for group 3 Amazonian Craton (3AmC) for a sublithospheric potential temperature of 1200°C without an eclogitic layer. All solutions that fit the dispersion curves are in grey; those that fit both the dispersion curves and the elevation are in blue; those that fit dispersion curves, elevation, and geoid are in red. Top row: (a) Geotherms, (b) density profiles, and (c) V_{SV} profiles. Middle row: (d) group Rayleigh-wave groups velocities vs period and, (e) respective misfits, (f) group Love-wave groups velocities vs period. and (g) respective misfits, (h) and (i) show elevation and geoid, respectively, with a dark grey box for the observed range. Bottom row: (j) water content vs background composition (top layer/bottom layer), (k) and (l) show histograms of the solutions for thermal lithosphere thickness, and Moho heat flow.

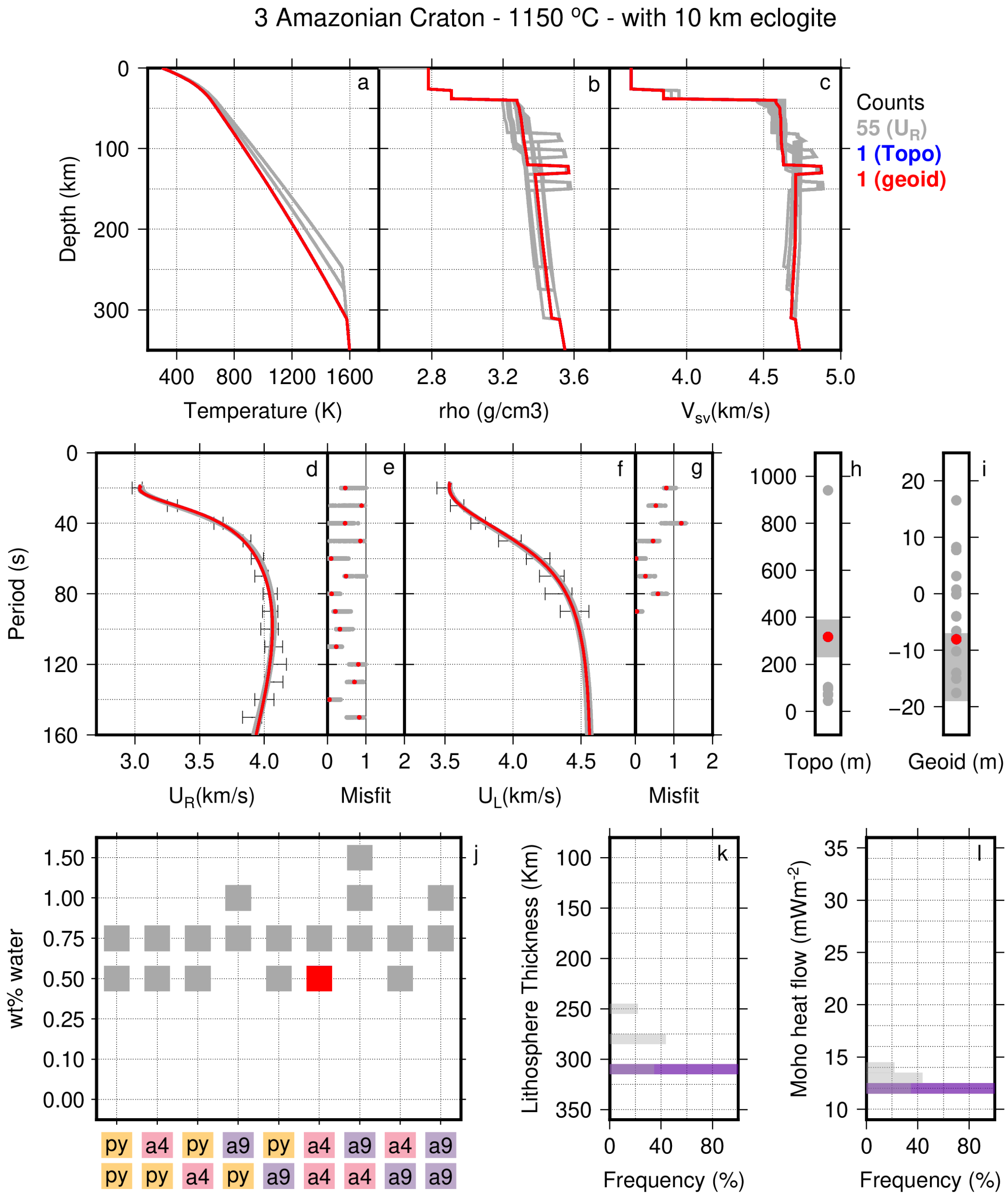

Figure S4 Set of solutions for group 3 Amazonian Craton (3AmC) for a sublithospheric potential temperature of 1150°C with a 10 km eclogitic layer. All solutions that fit the dispersion curves are in grey; those that fit both the dispersion curves and the elevation are in blue; those that fit dispersion curves, elevation, and geoid are in red. Top row: (a) Geotherms, (b) density profiles, and (c) V_{SV} profiles. Middle row: (d) group Rayleigh-wave groups velocities vs period and, (e) respective misfits, (f) group Love-wave groups velocities vs period. and (g) respective misfits, (h) and (i) show elevation and geoid, respectively, with a dark grey box for the observed range. Bottom row: (j) water content vs background composition (top layer/bottom layer), (k) and (l) show histograms of the solutions for thermal lithosphere thickness, and Moho heat flow.

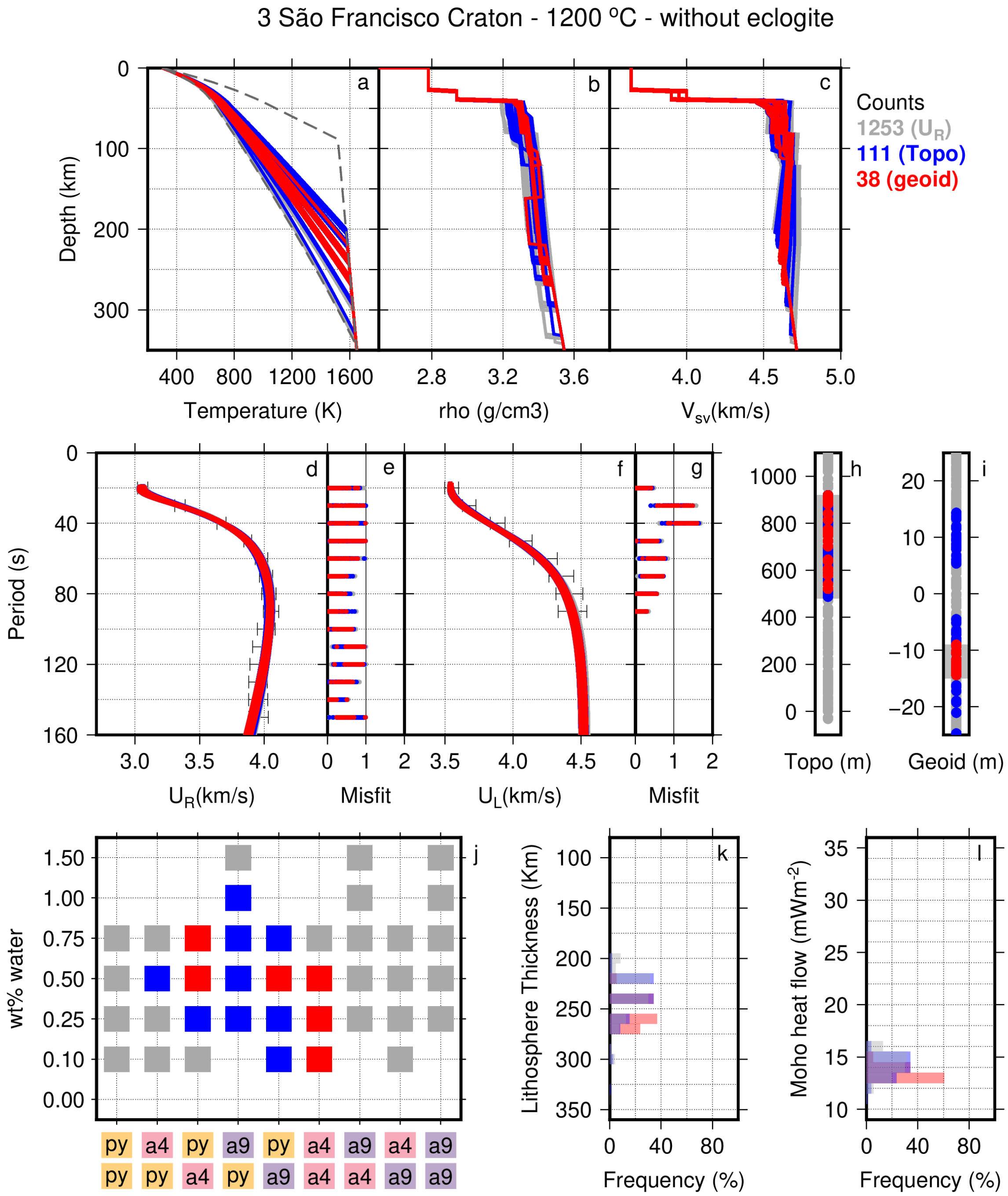

Figure S5 Set of solutions for group 3 São Francisco Craton (3SFC) for a sublithospheric potential temperature of 1200°C without an eclogitic layer. All solutions that fit the dispersion curves are in grey; those that fit both the dispersion curves and the elevation are in blue; those that fit dispersion curves, elevation, and geoid are in red. Top row: (a) Geotherms, (b) density profiles, and (c) V_{SV} profiles. Middle row: (d) group Rayleigh-wave groups velocities vs period and, (e) respective misfits, (f) group Love-wave groups velocities vs period. and (g) respective misfits, (h) and (i) show elevation and geoid, respectively, with a dark grey box for the observed range. Bottom row: (j) water content vs background composition (top layer/bottom layer), (k) and (l) show histograms of the solutions for thermal lithosphere thickness, and Moho heat flow.

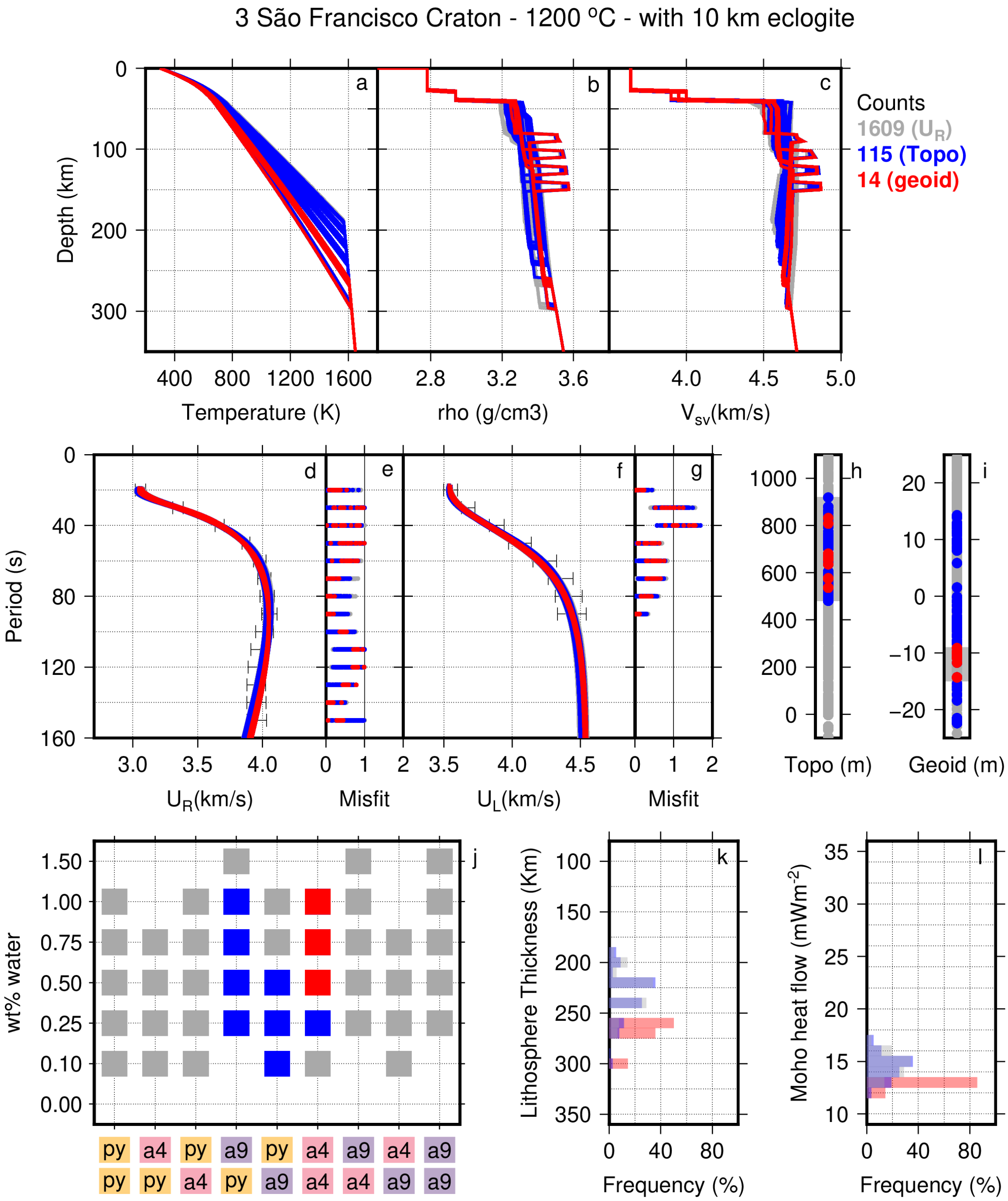

Figure S6 Set of solutions for group 3 São Francisco Craton (3SFC) for a sublithospheric potential temperature of 1200°C wit a 10 km eclogitic layer. All solutions that fit the dispersion curves are in grey; those that fit both the dispersion curves and the elevation are in blue; those that fit dispersion curves, elevation, and geoid are in red. Top row: (a) Geotherms, (b) density profiles, and (c) V_{SV} profiles. Middle row: (d) group Rayleigh-wave groups velocities vs period and, (e) respective misfits, (f) group Love-wave groups velocities vs period. and (g) respective misfits, (h) and (i) show elevation and geoid, respectively, with a dark grey box for the observed range. Bottom row: (j) water content vs background composition (top layer/bottom layer), (k) and (l) show histograms of the solutions for thermal lithosphere thickness, and Moho heat flow.

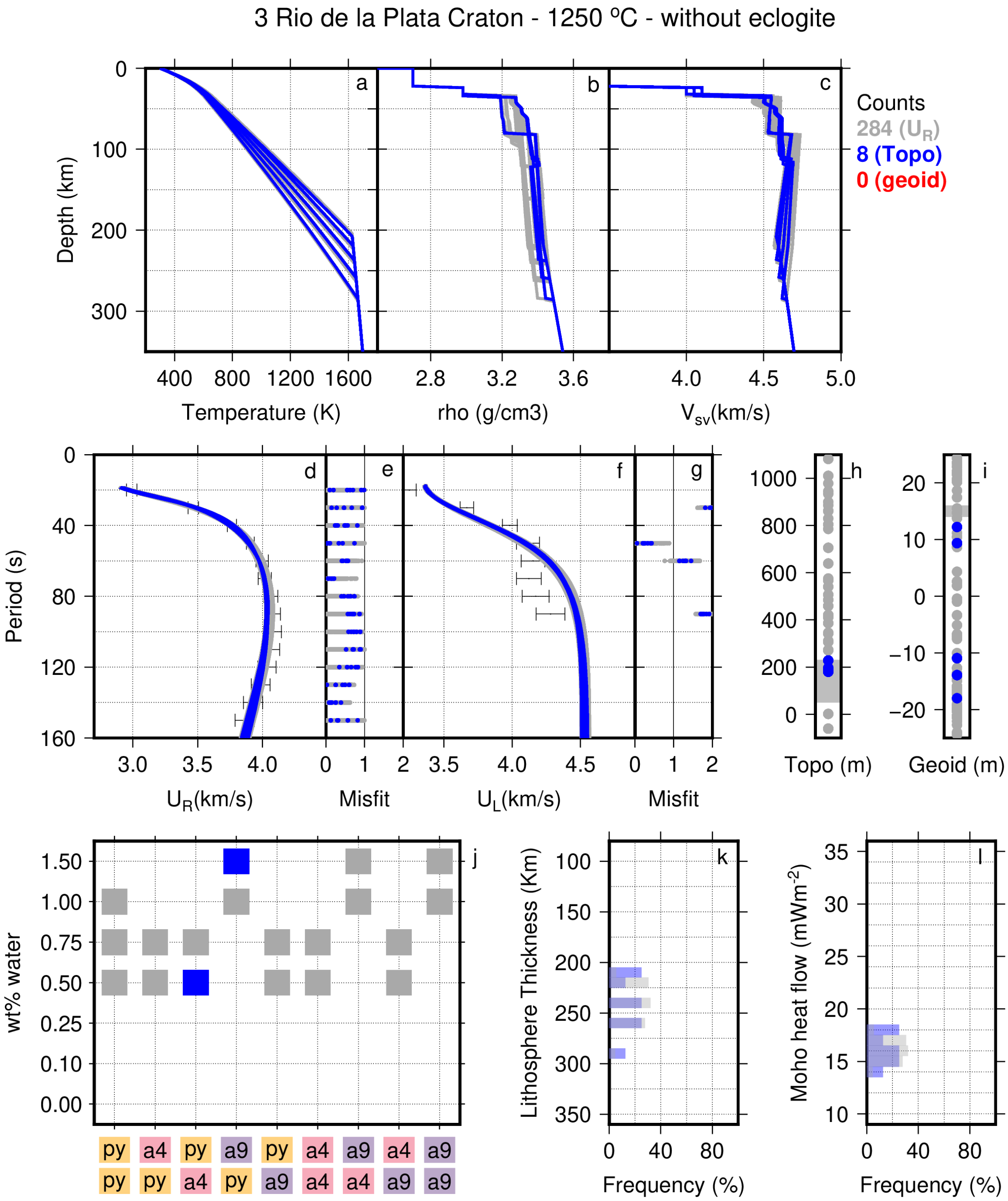

Figure S7 Set of solutions for group 3 Rio de la Plata Craton (3RPC) for a sublithospheric potential temperature of 1250°C without an eclogitic layer. All solutions that fit the dispersion curves are in grey; those that fit both the dispersion curves and the elevation are in blue; those that fit dispersion curves, elevation, and geoid are in red. Top row: (a) Geotherms, (b) density profiles, and (c) V_{SV} profiles. Middle row: (d) group Rayleigh-wave groups velocities vs period and, (e) respective misfits, (f) group Love-wave groups velocities vs period. and (g) respective misfits, (h) and (i) show elevation and geoid, respectively, with a dark grey box for the observed range. Bottom row: (j) water content vs background composition (top layer/bottom layer), (k) and (l) show histograms of the solutions for thermal lithosphere thickness, and Moho heat flow.

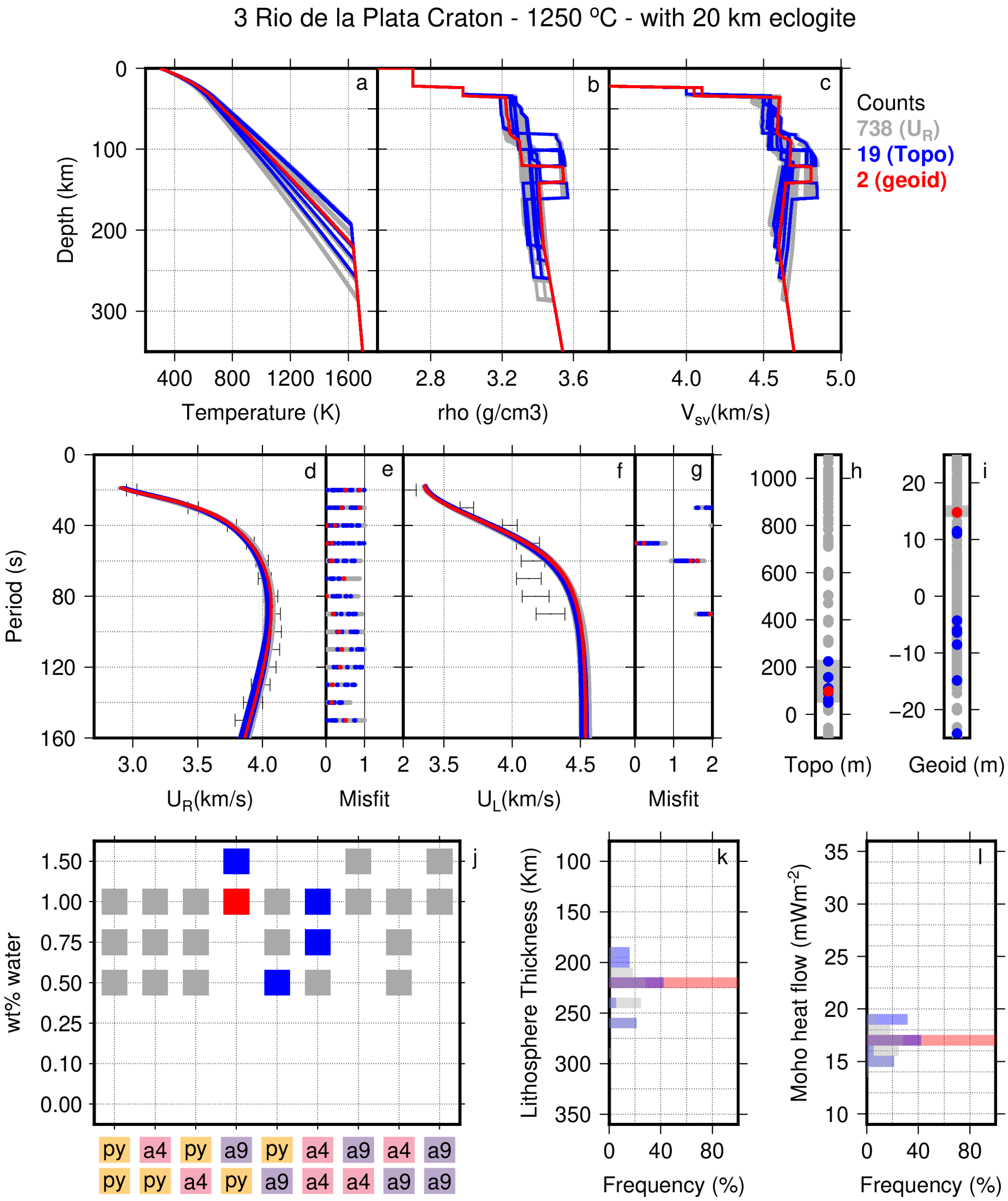

Figure S7 Set of solutions for group 3 Rio de la Plata Craton (3RPC) for a sublithospheric potential temperature of 1250°C with a 20 km eclogitic layer. All solutions that fit the dispersion curves are in grey; those that fit both the dispersion curves and the elevation are in blue; those that fit dispersion curves, elevation, and geoid are in red. Top row: (a) Geotherms, (b) density profiles, and (c) V_{SV} profiles. Middle row: (d) group Rayleigh-wave groups velocities vs period and, (e) respective misfits, (f) group Love-wave groups velocities vs period. and (g) respective misfits, (h) and (i) show elevation and geoid, respectively, with a dark grey box for the observed range. Bottom row: (j) water content vs background composition (top layer/bottom layer), (k) and (l) show histograms of the solutions for thermal lithosphere thickness, and Moho heat flow.

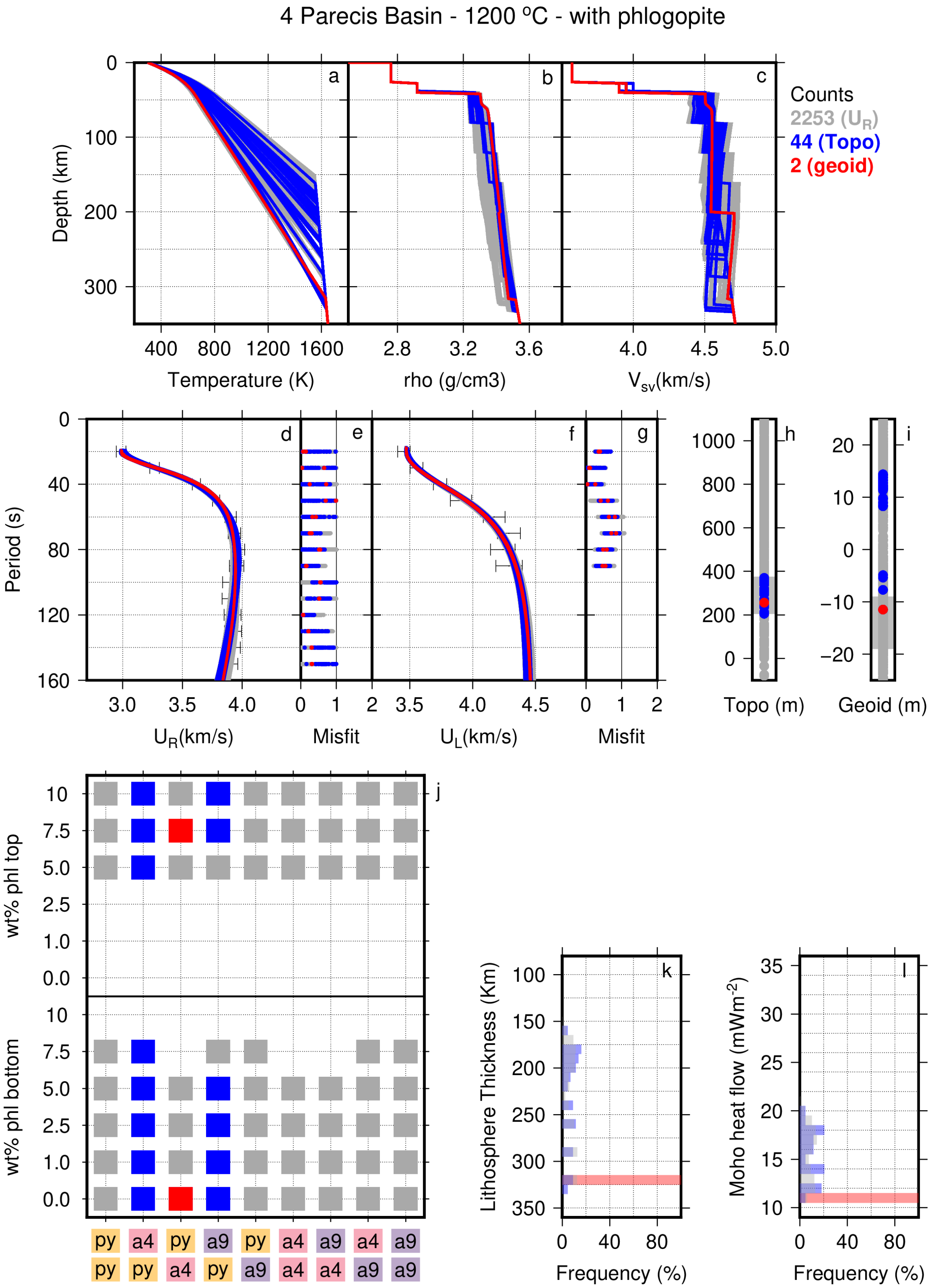

Figure S8 Set of solutions for group 4 Parecis Basin (4PcB) for a sublithospheric potential temperature of 1200°C with addition of Plogopite. All solutions that fit the dispersion curves are in grey; those that fit both the dispersion curves and the elevation are in blue; those that fit dispersion curves, elevation, and geoid are in red. Top row: (a) Geotherms, (b) density profiles, and (c) V_{SV} profiles. Middle row: (d) group Rayleigh-wave groups velocities vs period and, (e) respective misfits, (f) group Love-wave groups velocities vs period. and (g) respective misfits, (h) and (i) show elevation and geoid, respectively, with a dark grey box for the observed range. Bottom row: (j) Phlogopite content vs background composition (top layer/bottom layer), (k) and (l) show histograms of the solutions for thermal lithosphere thickness, and Moho heat flow.

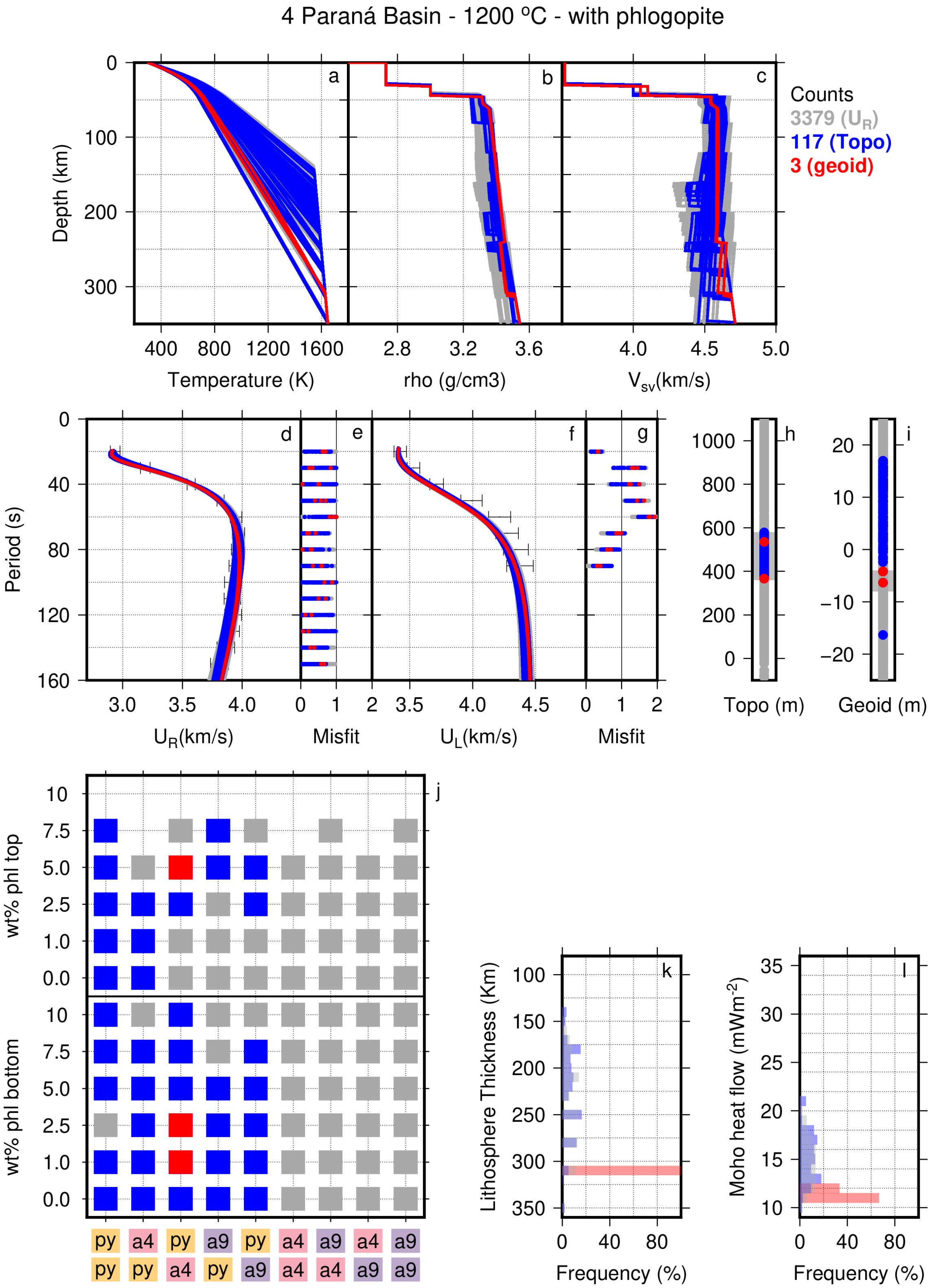

Figure S9 Set of solutions for group 4 Paraná Basin (4PrB) for a sublithospheric potential temperature of 1200°C with addition of Plogopite. All solutions that fit the dispersion curves are in grey; those that fit both the dispersion curves and the elevation are in blue; those that fit dispersion curves, elevation, and geoid are in red. Top row: (a) Geotherms, (b) density profiles, and (c) V_{SV} profiles. Middle row: (d) group Rayleigh-wave groups velocities vs period and, (e) respective misfits, (f) group Love-wave groups velocities vs period. and (g) respective misfits, (h) and (i) show elevation and geoid, respectively, with a dark grey box for the observed range. Bottom row: (j) Phlogopite content vs background composition (top layer/bottom layer), (k) and (l) show histograms of the solutions for thermal lithosphere thickness, and Moho heat flow.

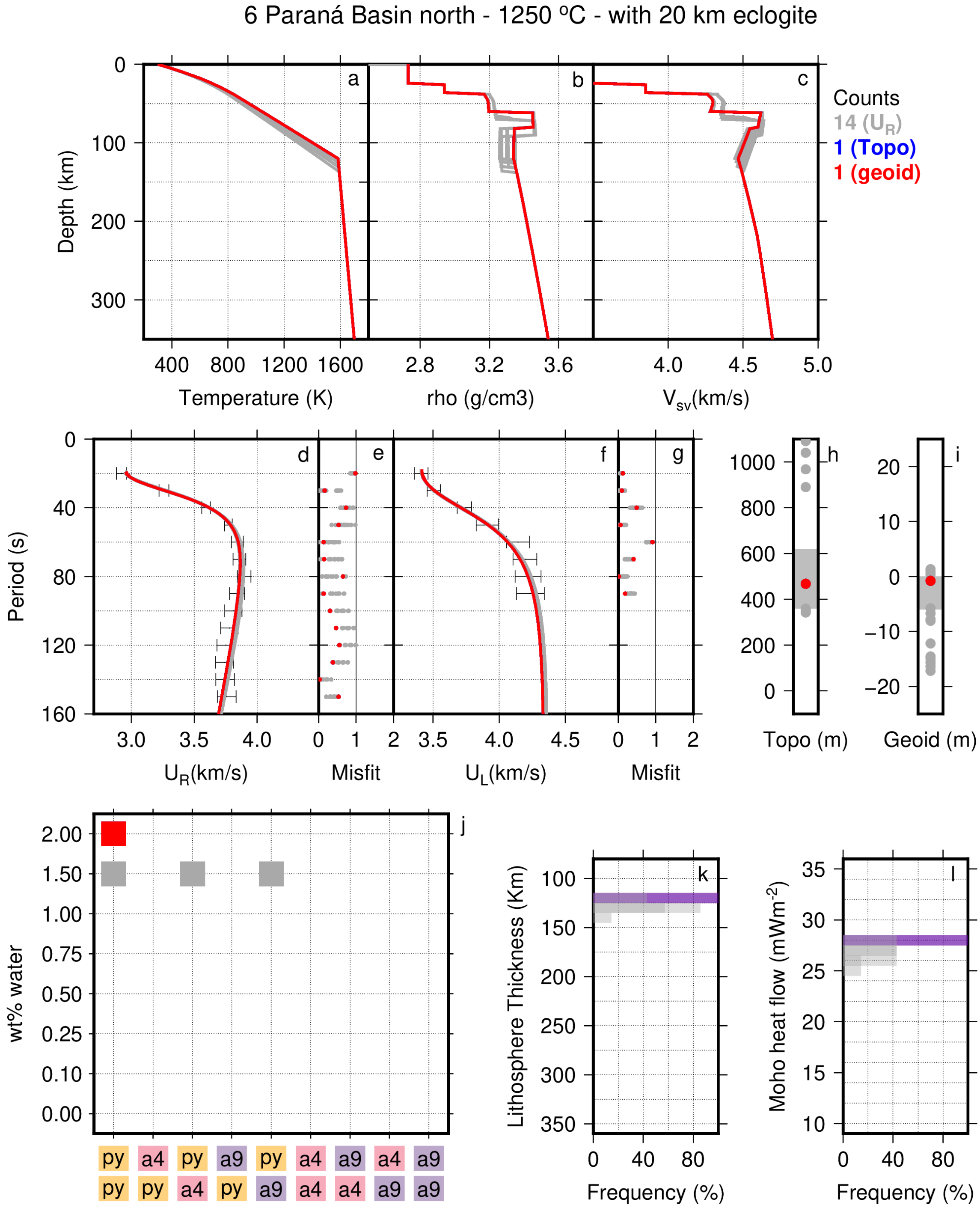

Figure S10 Set of solutions for group 6 Paraná Basin north (6PrB(n)) for a sublithospheric potential temperature of 1250°C with a 20 km eclogitic layer. All solutions that fit the dispersion curves are in grey; those that fit both the dispersion curves and the elevation are in blue; those that fit dispersion curves, elevation, and geoid are in red. Top row: (a) Geotherms, (b) density profiles, and (c) V_{SV} profiles. Middle row: (d) group Rayleigh-wave groups velocities vs period and, (e) respective misfits, (f) group Love-wave groups velocities vs period. and (g) respective misfits, (h) and (i) show elevation and geoid, respectively, with a dark grey box for the observed range. Bottom row: (j) water content vs background composition (top layer/bottom layer), (k) and (l) show histograms of the solutions for thermal lithosphere thickness, and Moho heat flow.

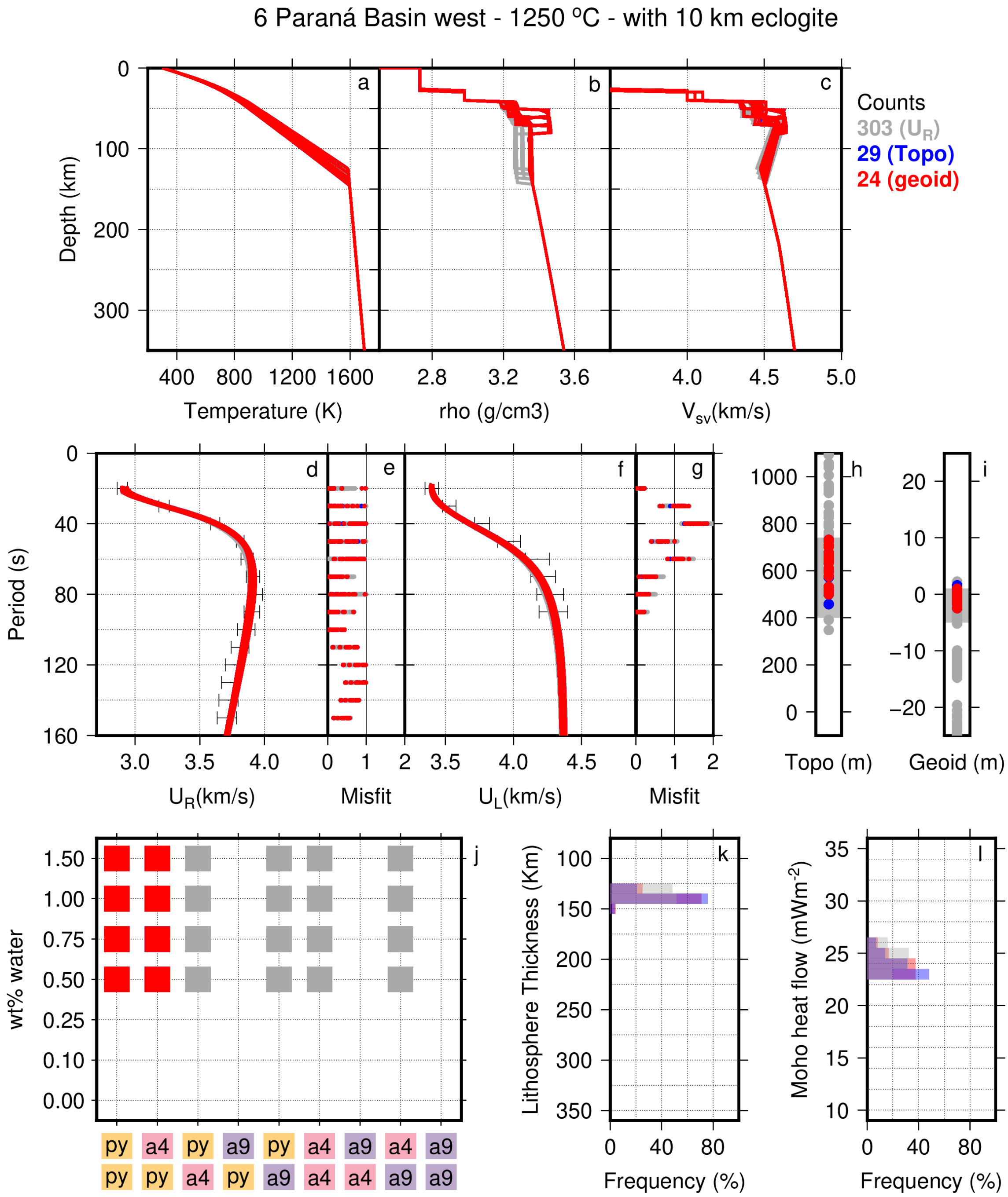

Figure S11 Set of solutions for group 6 Paraná Basin west (6PrB(w)) for a sublithospheric potential temperature of 1250°C with a 10 km eclogitic layer. All solutions that fit the dispersion curves are in grey; those that fit both the dispersion curves and the elevation are in blue; those that fit dispersion curves, elevation, and geoid are in red. Top row: (a) Geotherms, (b) density profiles, and (c) V_{SV} profiles. Middle row: (d) group Rayleigh-wave groups velocities vs period and, (e) respective misfits, (f) group Love-wave groups velocities vs period. and (g) respective misfits, (h) and (i) show elevation and geoid, respectively, with a dark grey box for the observed range. Bottom row: (j) water content vs background composition (top layer/bottom layer), (k) and (l) show histograms of the solutions for thermal lithosphere thickness, and Moho heat flow.

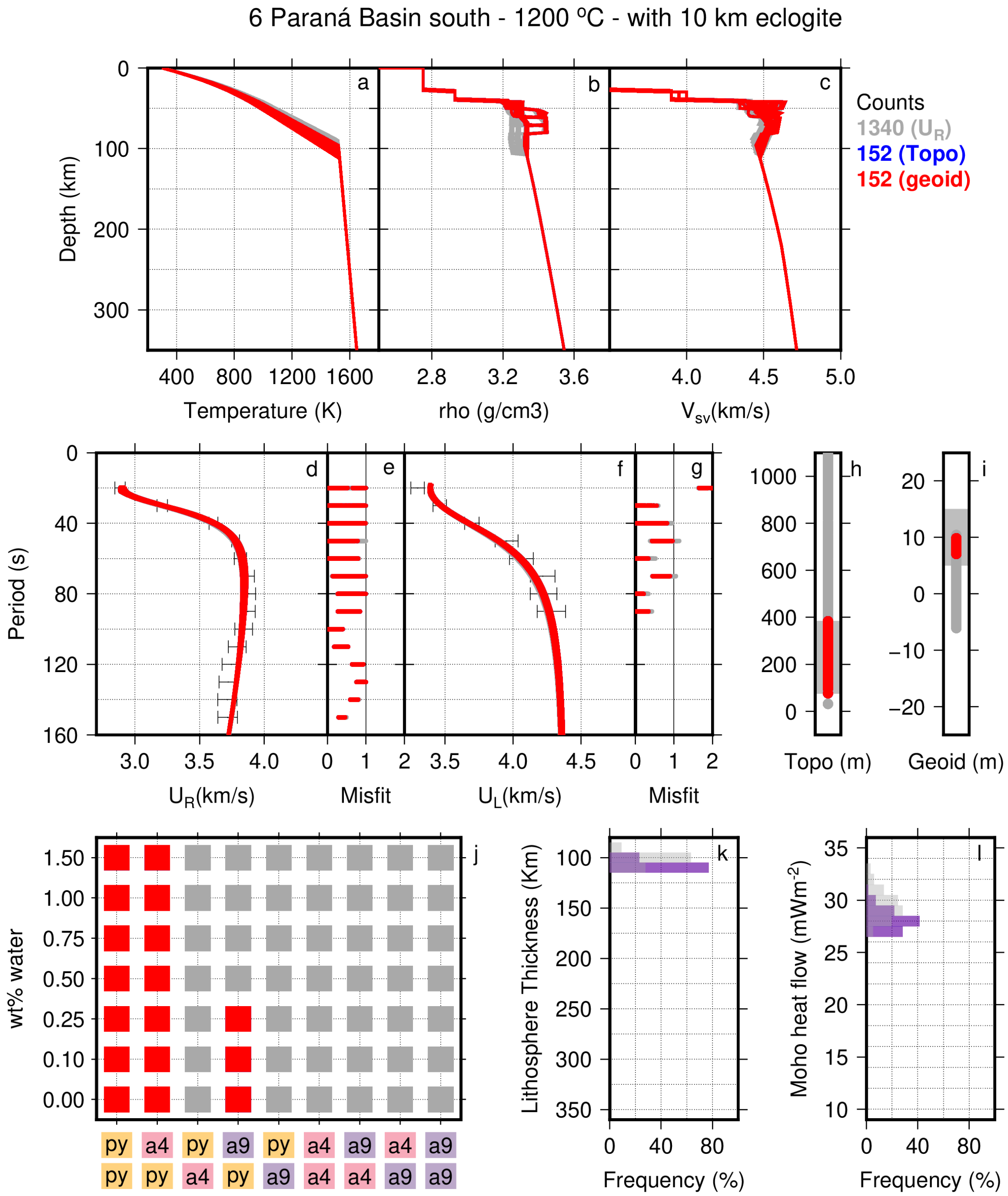

Figure S12 Set of solutions for group 6 Paraná Basin south (6PrB(s)) for a sublithospheric potential temperature of 1200°C with a 10 km eclogitic layer. All solutions that fit the dispersion curves are in grey; those that fit both the dispersion curves and the elevation are in blue; those that fit dispersion curves, elevation, and geoid are in red. Top row: (a) Geotherms, (b) density profiles, and (c) V_{SV} profiles. Middle row: (d) group Rayleigh-wave groups velocities vs period and, (e) respective misfits, (f) group Love-wave groups velocities vs period. and (g) respective misfits, (h) and (i) show elevation and geoid, respectively, with a dark grey box for the observed range. Bottom row: (j) water content vs background composition (top layer/bottom layer), (k) and (l) show histograms of the solutions for thermal lithosphere thickness, and Moho heat flow.

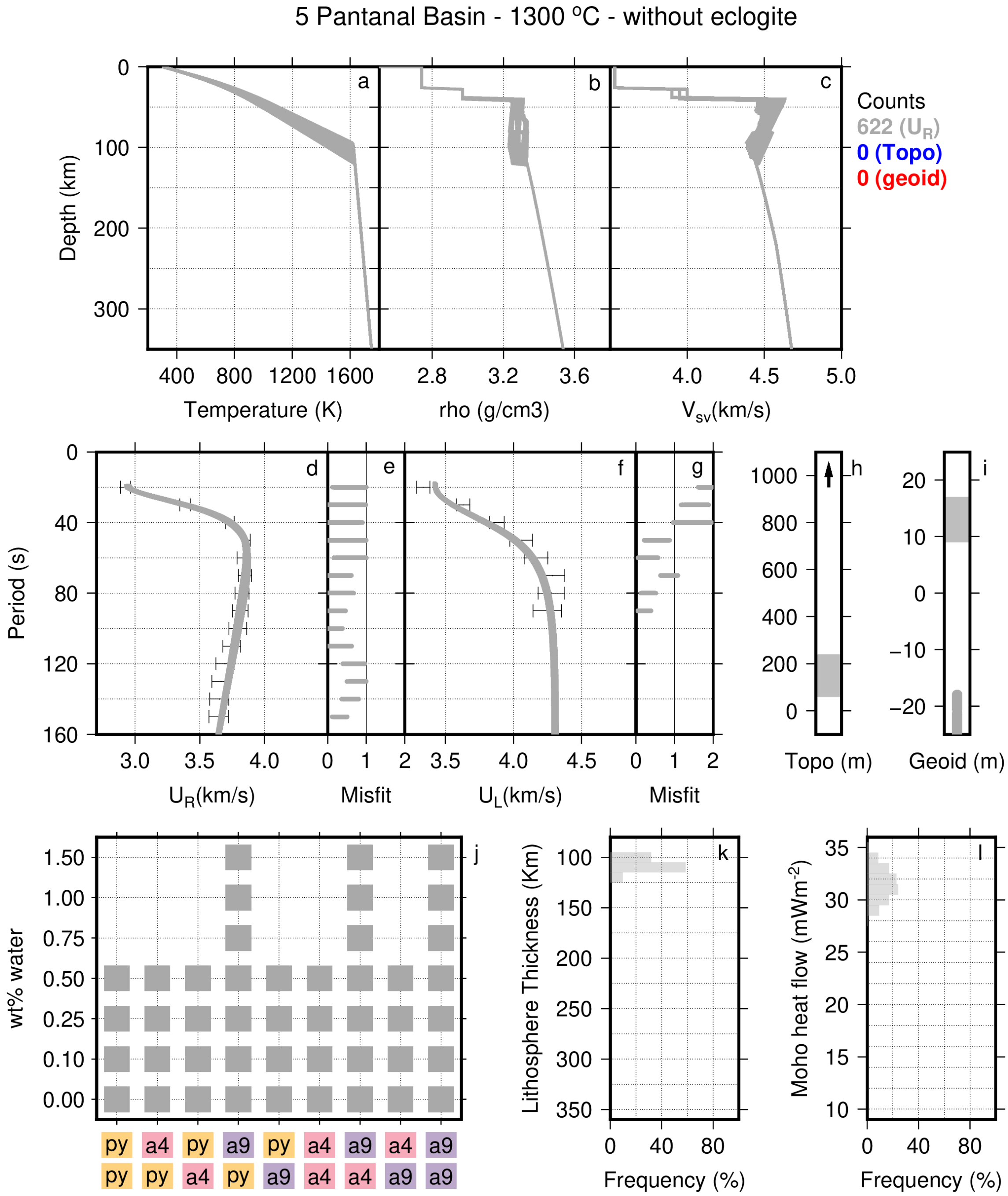

Figure S13 Set of solutions for group 5 Pantanal Basin (5PtB) for a sublithospheric potential temperature of 1300°C without an eclogitic layer. All solutions that fit the dispersion curves are in grey; those that fit both the dispersion curves and the elevation are in blue; those that fit dispersion curves, elevation, and geoid are in red. Solutions for elevation range between 1545 and 3254 meter. Solutions for elevation range between 1545 and 3254 meter. Top row: (a) Geotherms, (b) density profiles, and (c) V_{SV} profiles. Middle row: (d) group Rayleigh-wave groups velocities vs period and, (e) respective misfits, (f) group Love-wave groups velocities vs period. and (g) respective misfits, (h) and (i) show elevation and geoid, respectively, with a dark grey box for the observed range. Bottom row: (j) water content vs background composition (top layer/bottom layer), (k) and (l) show histograms of the solutions for thermal lithosphere thickness, and Moho heat flow.

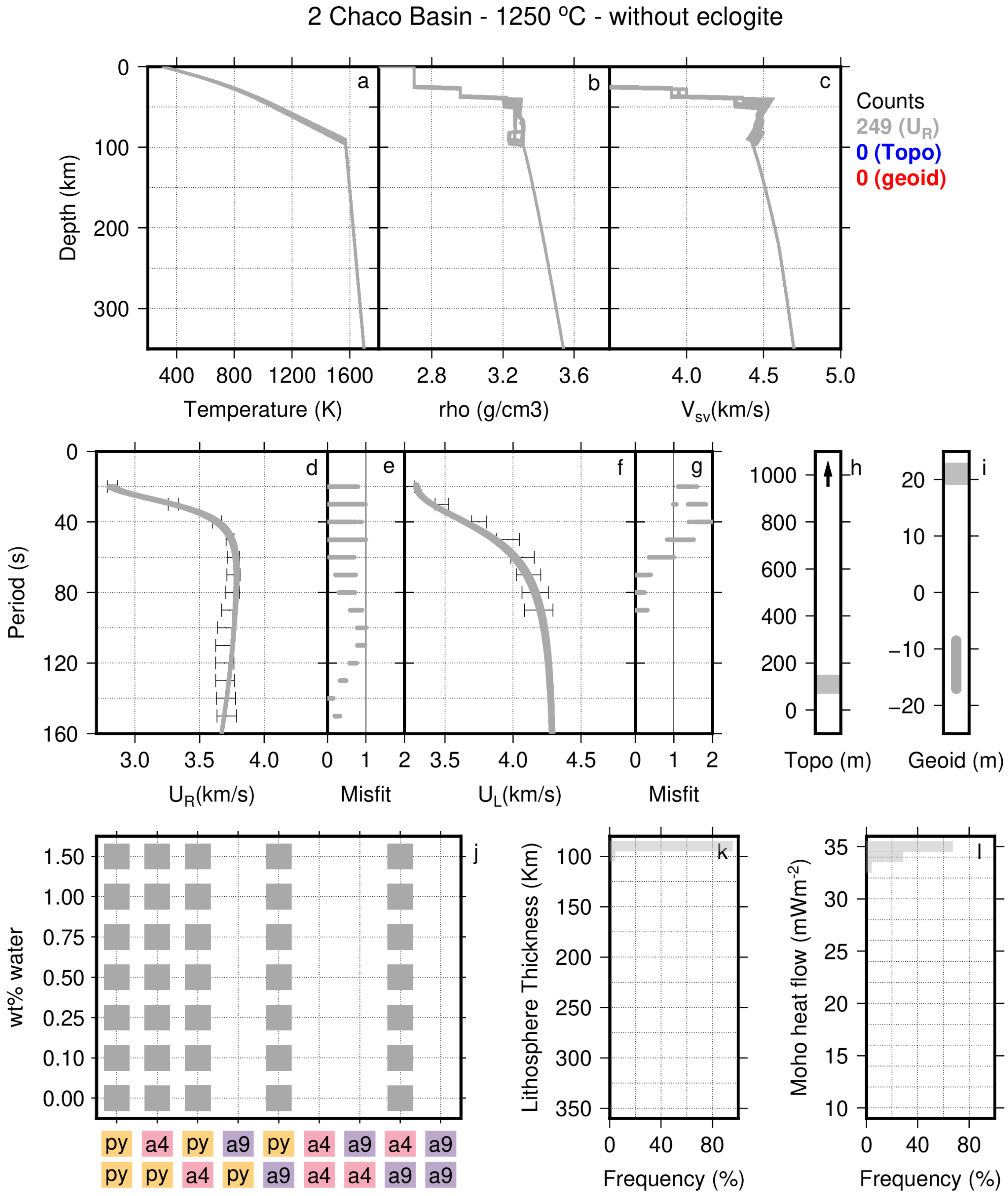

Figure S14 Set of solutions for group 2 Chaco Basin (2ChB) for a sublithospheric potential temperature of 1250°C without an eclogitic layer. All solutions that fit the dispersion curves are in grey; those that fit both the dispersion curves and the elevation are in blue; those that fit dispersion curves, elevation, and geoid are in red. Solutions for elevation range between 1626 and 2564 meters. Top row: (a) Geotherms, (b) density profiles, and (c) V_{SV} profiles. Middle row: (d) group Rayleigh-wave groups velocities vs period and, (e) respective misfits, (f) group Love-wave groups velocities vs period. and (g) respective misfits, (h) and (i) show elevation and geoid, respectively, with a dark grey box for the observed range. Bottom row: (j) water content vs background composition (top layer/bottom layer), (k) and (l) show histograms of the solutions for thermal lithosphere thickness, and Moho heat flow.

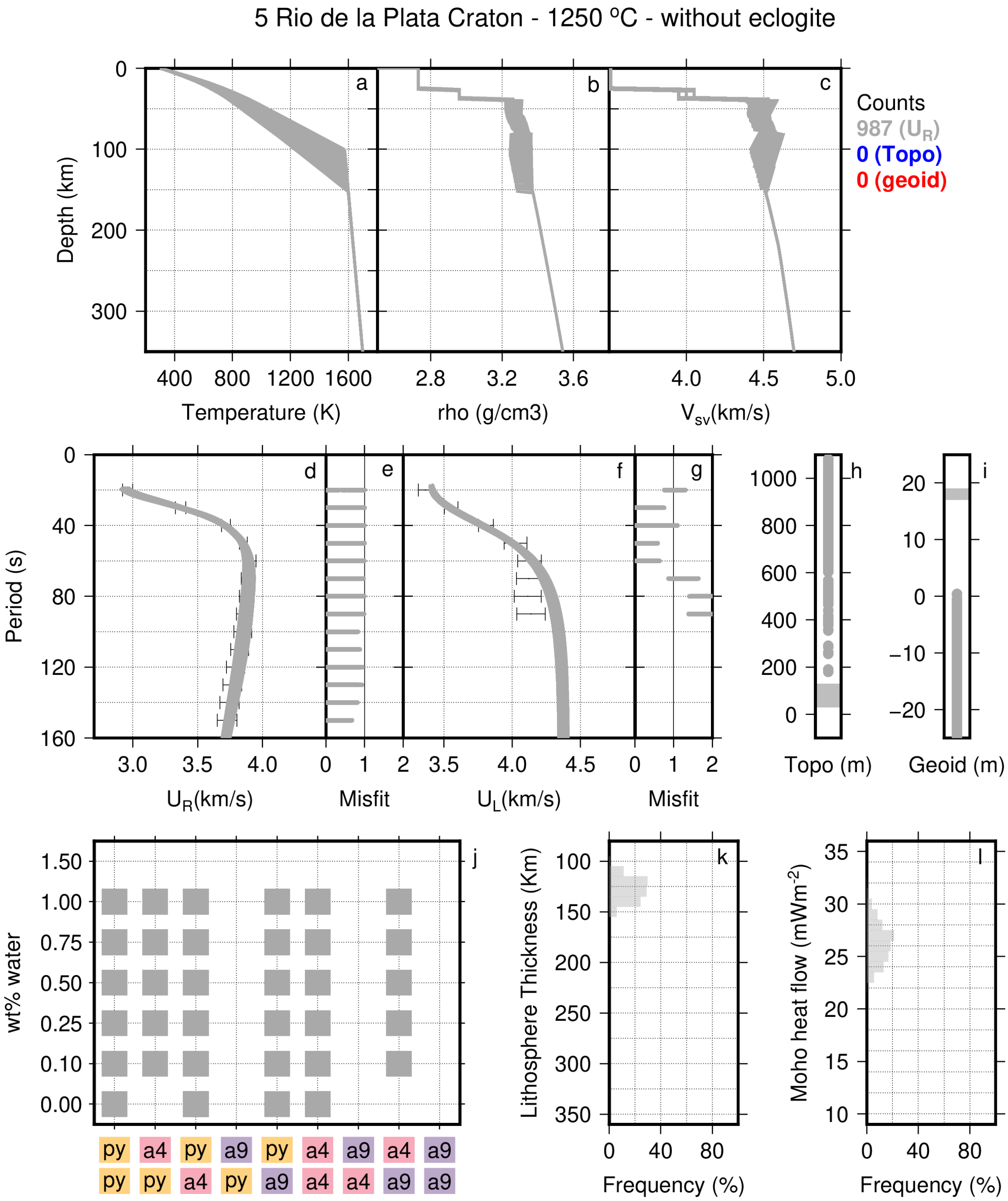

Figure S15 Set of solutions for group 5 Rio de la Plata Craton (5RPC) for a sublithospheric potential temperature of 1250°C without an eclogitic layer. All solutions that fit the dispersion curves are in grey; those that fit both the dispersion curves and the elevation are in blue; those that fit dispersion curves, elevation, and geoid are in red. Top row: (a) Geotherms, (b) density profiles, and (c) V_{SV} profiles. Middle row: (d) group Rayleigh-wave groups velocities vs period and, (e) respective misfits, (f) group Love-wave groups velocities vs period. and (g) respective misfits, (h) and (i) show elevation and geoid, respectively, with a dark grey box for the observed range. Bottom row: (j) water content vs background composition (top layer/bottom layer), (k) and (l) show histograms of the solutions for thermal lithosphere thickness, and Moho heat flow.

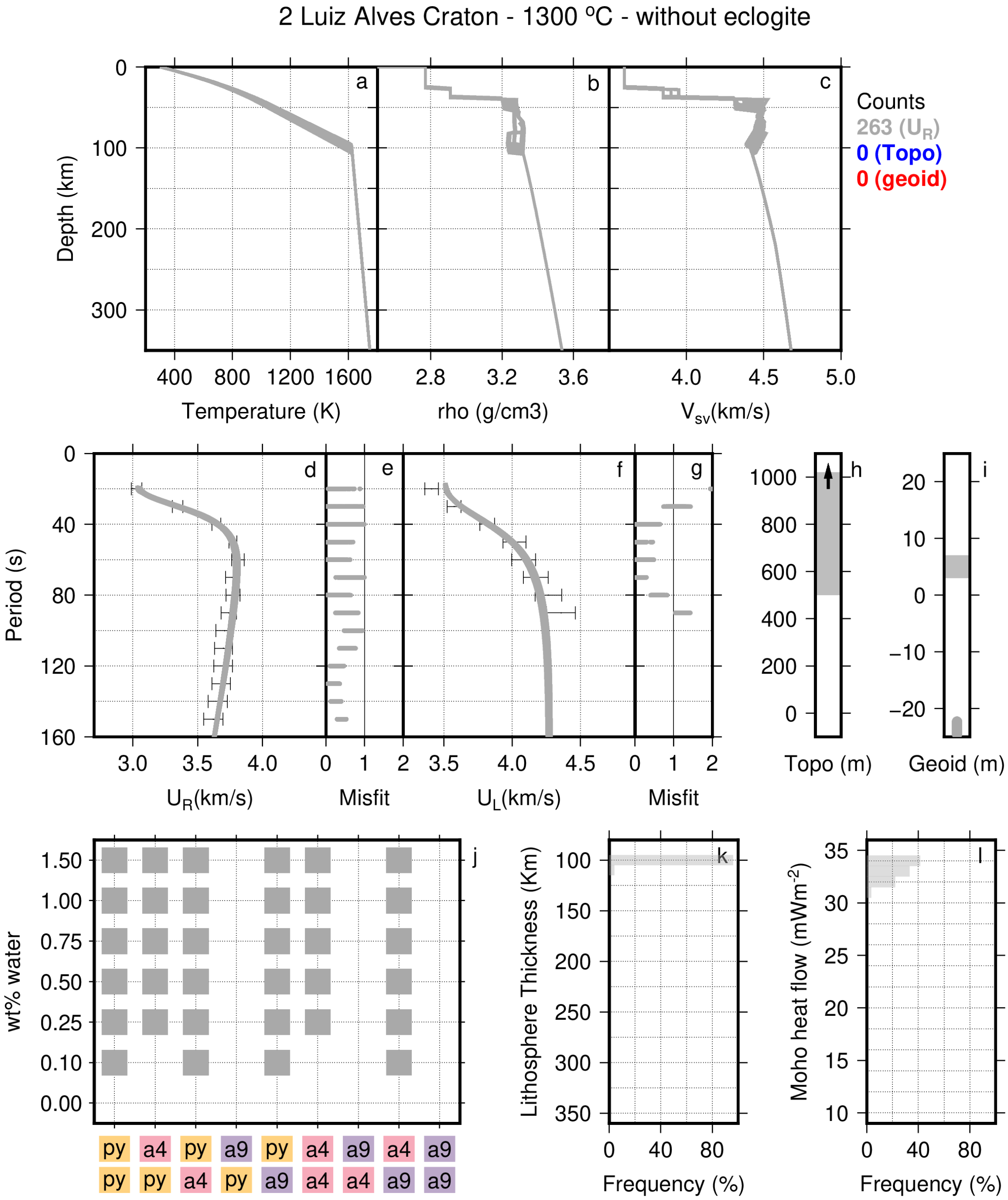

Figure S16 Set of solutions for group 2 Luiz Alves Craton (2LAC) for a sublithospheric potential temperature of 1300°C without an eclogitic layer. All solutions that fit the dispersion curves are in grey; those that fit both the dispersion curves and the elevation are in blue; those that fit dispersion curves, elevation, and geoid are in red. Solutions for elevation range between 1601 and 2838. Top row: (a) Geotherms, (b) density profiles, and (c) V_{SV} profiles. Middle row: (d) group Rayleigh-wave groups velocities vs period and, (e) respective misfits, (f) group Love-wave groups velocities vs period. and (g) respective misfits, (h) and (i) show elevation and geoid, respectively, with a dark grey box for the observed range. Bottom row: (j) water content vs background composition (top layer/bottom layer), (k) and (l) show histograms of the solutions for thermal lithosphere thickness, and Moho heat flow.

References

Griffin, W. L., O'Reilly, S. Y., Afonso, J. C., & Begg, G. C. (2009, 7). The Composition and Evolution of Lithospheric Mantle: a Re-evaluation and its Tectonic Implications. *Journal of Petrology*, *50*(7), 1185–1204. doi: 10.1093/petrology/egn033

Hacker, B. R. (2008, 3). H2O subduction beyond arcs. *Geochemistry, Geophysics, Geosystems*, *9*(3). doi: 10.1029/2007GC001707

Hasterok, D., & Chapman, D. (2011, 7). Heat production and geotherms for the continental lithosphere. *Earth and Planetary Science Letters*, *307*(1-2), 59–70. doi: 10.1016/J.EPSL.2011.04.034

Herzberg, C., Asimow, P. D., Arndt, N., Niu, Y., Lesher, C. M., Fitton, J. G., ... Saunders, A. D. (2007, 2). Temperatures in ambient mantle and plumes: Constraints from basalts, picrites, and komatiites. *Geochemistry, Geophysics, Geosystems*, *8*(2). doi: 10.1029/2006GC001390

Holland, T., Baker, J., & Powell, R. (1998). Mixing properties and activity-composition relationships of chlorites in the system MgO-FeO-Al2O3-SiO2-H2O. *European Journal of Mineralogy*. doi: 10.1127/ejm/10/3/0395

Holland, T., & Powelll, R. (1996). Thermodynamics of order-disorder in minerals: II. Symmetric formalism applied to solid solutions. *American Mineralogist*. doi: 10.2138/am-1996-11-1215

Holland, T. J., & Powell, R. (1998). An internally consistent thermodynamic data set for phases of petrological interest. *Journal of Metamorphic Geology*, *16*(3), 309–343. doi: 10.1111/j.1525-1314.1998.00140.x

Jamieson, H. E., & Roeder, P. L. (1984). The distribution of Mg and Fe2+ between olivine and spinel at 1300oC. *American Mineralogist*, *69*(3-4).

Jaupart, C., & Mareschal, J. C. (1999, 9). The thermal structure and thickness of continental roots. *Lithos*, *48*(1-4), 93–114. doi: 10.1016/S0024-4937(99)00023-7

Laske, G., Masters, G., Ma, Z., & Pasyanos, M. (2013). Update on CRUST1.0—A 1-degree global model of Earth's crust. In *Egu general assembly 2013* (Vol. 15).

Lévy, F., & Jaupart, C. (2011, 1). Temperature and rheological properties of the mantle beneath the North American craton from an analysis of heat flux and seismic data. *Journal of Geophysical Research*, *116*(B1), B01408. doi: 10.1029/2010JB007726

Massonne, H.-J. W. (2008). Phase relations and dehydration behaviour of psammopelite and mid-ocean ridge basalt at very-low-grade to low-grade metamorphic conditions. *European Journal of Mineralogy*. doi: 10.1127/0935-1221/2008/0020-1871

Michaut, C., Jaupart, C., & Bell, D. R. (2007, 4). Transient geotherms in Archean continental lithosphere: New constraints on thickness and heat production of the subcontinental lithospheric mantle. *Journal of Geophysical Research: Solid Earth*, *112*(4). doi: 10.1029/2006JB004464

Newton, R. C., Charlu, T. V., & Kleppa, O. J. (1980). Thermochemistry of the high structural state plagioclases. *Geochimica et Cosmochimica Acta*. doi: 10.1016/0016-7037(80)90283-5

Padrón-Navarta, J. A., Sánchez-Vizcaíno, V. L., Hermann, J., Connolly, J. A., Garrido, C. J., Gómez-Pugnaire, M. T., & Marchesi, C. (2013). Tschermak's substitution in antigorite and consequences for phase relations and water liberation in high-grade serpentinites. *Lithos*. doi: 10.1016/j.lithos.2013.02.001

Rivadeneyra-Vera, C., Bianchi, M., Assumpção, M., Cedraz, V., Julià, J., Rodríguez, M., ... Fernandez, G. (2019). An updated crustal thickness map of central South America based on receiver function measurements in the region of the Chaco, Pantanal, and Paraná Basins, southwestern Brazil. *Journal of Geophysical Research: Solid Earth*, *124*(8), 8491–8505. doi: 10.1029/2018JB016811

Rudnick, R., & Nyblade, A. (1999). The thickness and heat production of Archean lithosphere: constraints from xenolith thermobarometry and surface heat flow. *Mantle petrology: Field observations and high pressure Experimentation: A Tribute to Francis R. (Joe) Boyd*(6), 3–12.

Shapiro, N. M., Ritzwoller, M. H., Mareschal, J. C., & Jaupart, C. (2004, 1). Lithospheric structure of the Canadian Shield inferred from inversion of surface-wave dispersion with thermodynamic <i>a priori</i> constraints. *Geological Society, London, Special Publications*, *239*(1), 175–194. doi: 10.1144/GSL.SP.2004.239.01.12

Wei, C., & Powell, R. (2003). Phase relations in high-pressure metapelites in the system KFMASH (K2O?FeO?MgO?Al2O3?SiO2?H2O) with application to natural rocks. *Contributions to Mineralogy and Petrology*. doi: 10.1007/s00410-003-0454-1

White, Powell, Holland, & Worley. (2000). The effect of TiO2 and Fe2O3 on metapelitic assemblages at greenschist and amphibolite facies conditions: Mineral equilibria calculations in the system K2O-FeO-MgO-Al2O3-SiO2-H2O-TiO2-Fe2O3. *Journal of Metamorphic Geology*. doi: 10.1046/j.1525-1314.2000.00269.x

White, R. W., Powell, R., & Phillips, G. N. (2003). A mineral equilibria study of the hydrothermal alteration in mafic greenschist facies rocks at Kalgoorlie, Western Australia. *Journal of Metamorphic Geology*. doi: 10.1046/j.1525-1314.2003.00454.x

Xu, W., Lithgow-Bertelloni, C., Stixrude, L., & Ritsema, J. (2008). The effect of bulk composition and temperature on mantle seismic structure. *Earth and Planetary Science Letters*, *275*(1-2), 70–79. doi: 10.1016/j.epsl.2008.08.012